Sub-kpc Scale Analysis of Stellar Chemical Abundance and Star Formation Distributions in Nearby Galaxies

Myles Anthony Aaron Alexander McKay

A dissertation
submitted in partial fulfillment of the
requirements for the degree of

Doctor of Philosophy

University of Washington

2024

Reading Committee:
Benjamin Williams, Chair
Eleanor Byler
Mario Juric

Program Authorized to Offer Degree:
Astronomy

University of Washington

Abstract

Sub-kpc Scale Analysis of Stellar Chemical Abundance and Star Formation Distributions in Nearby Galaxies

Myles Anthony Aaron Alexander McKay

Chair of the Supervisory Committee:
Benjamin Williams
Astronomy

Nearby galaxies provide critical insights into the complex chemical and stellar evolution of galaxies over cosmic time. High-quality resolved measurements provide insight into the intrinsic details of evolution when investigating the stellar population and chemical abundance in the bulge and disk regions. Furthermore, this allows us to compare the radial distribution properties of different galaxies to examine their recent evolution, especially among distinct galaxies. In this work, we utilize integral field unit spectroscopy (IFS) and high-resolution stellar photometry to examine the distribution of nearby galaxies. We first investigate the radial distribution of stellar population, star formation, and oxygen abundance in centrally star-forming galaxies with photometrically red disks, termed BreakBRD galaxies, compared to the parent sample using the MaNGA IFS survey. We find that the BreakBRD galaxies exhibit a significant positive stellar population age profile but show no significant variation in stellar mass surface density, star formation surface density, or oxygen abundance. We estimate the RGB metallicity gradient of M31's northern and southern halves from the PHAT and PHAST surveys, respectively, and find a shallow negative gradient in both halves. We interpret this result as indicating that the older RGB stellar population is well mixed throughout the disk. Additionally, we have developed a photometry pipeline for future flagship surveys and used high-quality MaNGA data with a high-performance deep learning

model to test prediction accuracy for recovering the ionization source.

TABLE OF CONTENTS

LIST OF FIGURES

Figure Number Page

ACKNOWLEDGMENTS

This PhD journey would not have been possible without the unwavering support of my family, mentors, and friends, who have been a source of light throughout this endeavor.

First and foremost, I extend my deepest gratitude to my mother, Sonja Bryant; my sister, Ari'yell Bryant; and my younger brothers, Mark and Matthew Washington. Your support and understanding over the years have been invaluable as I pursued this Ph.D.

I am profoundly grateful for the mentorship and support provided by Professor Donald Walter at South Carolina State University during my undergraduate studies. Your guidance opened doors to numerous opportunities and collaborations in astronomy. I also wish to thank my mentors from the National Astronomy Consortium (NAC) for their inspiring research and reliable mentorship, which laid a solid foundation for my career in astronomy. Special thanks to Dr. Nell Byler for the research internship at the Pacific Northwest National Laboratory and for your steadfast support and advocacy.

I am also thankful to the graduate students at the University of Washington for creating a supportive and collaborative environment. My appreciation extends to GCAP for fostering a sense of community and space.

To my friends who have been a constant presence during my graduate studies, thank you for your companionship and support. I am particularly grateful to Lupita and Andrell, Debby and Tron for their help with watching Lawrence while I worked on my thesis. Additional thanks to Nicole, Trevor, Hannah, Iryna, Dan, Diana, Michael, Steven, Dino, Bethlee, Rudy, Akaxia, Zeeshawn, Nicel, Samantha, and Leah for your encouragement and camaraderie. Thank you also to Jarvis, Jamar, Mike and my line brothers for always keeping me laughing

and looking out for me.

I want to express my thanks to my advisor, Professor Benjamin Williams, for your unwavering support and guidance throughout my PhD journey. Your insightful feedback and constructive suggestions have been instrumental in shaping this thesis. I am also deeply appreciative of the financial support you provided.

I am grateful to my reading committee—Professor Benjamin Williams, Dr. Eleanor Byler, Professor Mario Juric, and Professor Leilani Battle—for their thorough critiques and constructive comments, which have significantly enhanced the quality of this work.

Finally, I am thankful for the NSF fellowship awarded during my PhD studies. This fellowship has been crucial in supporting my research and academic development, and I deeply appreciate the opportunity it has provided.

Thank you all for being an integral part of this journey

DEDICATION

To my best friend and the love of my life, my wife Brianna McKay, to my baby-boy Lawrence McKay and my munchkin Skye. Your love and support have been my greatest sources of strength and inspiration.

Chapter 1

INTRODUCTION

When we imagine galaxies we think of the beautiful distinct spiral structure, the interesting color patterns from the stars and gas structure and the prominent bright central bulge. These are more than feature of the given galaxy and tells a story about the billions of years of evolution. Recent techniques have advanced our ability to gain insight into the details of the evolution when investigating the stellar population and chemical abundance and composition in the bulge and the disk region. The technique involve taking well known measurements of galaxies but on sub-kpc and individual star scales to investigate the stellar population and star formation activity. The key parameters for examining these regions are the stellar age and mass, oxygen/iron abundance (metallicity), the production and efficiency of the stars forming (star formation rate and star formation efficiency) and the current star types and colors.

Photometry, a method to study the integrated color of galaxies, has established that a galaxy's stellar photometry can be used to classify galaxies and infer recent star formation. The color and flux of a galaxy are strongly correlated with its star formation activity. Peak star formation occurred approximately 10 billion years ago (at $z \sim 3$).

Integral field unit spectroscopy(IFS) allows for spectral and spatail observation of nearby galaxies allow for studies of of stellar and gas properties and kinematics. The study the sub-kpc region have established that the local properties govern the evolution and the global properties influence the evolutionary path, the mass assembly of galaxies is formed inside-out regardless of morphology and mass and the local age can and the the same similar laws that the global evolutionary sequence holds on the kilo parsec scales.

Though stellar population radial distribution holds for most galaxies there are still population of galaxies that we don't fully understand evolution and distinct features. Additionally, the techniques that are used to obtain science-ready products is expansive and need data management systems to extract measurements as well as be used for machine learning applications. While we can use IFS observation method to establish a gas and stellar properties of nearby galaxies, we have limited knowledge of the underlying mechanisms that drive these properties on sub-kpc and smaller scales especially for galaxies that have distinct features.

In this work I utilize the radial distribution star formation and chemical abundance to infer evolution sequences of the distinct galaxies, measure the chemical abundance distribution of the the most resolved galaxy closest to us and software used to manage data and apply machine learning application to test other areas of study use for the expansive dataset.

Science Motivation

In this dissertation I aim to address the following science questions:

1. How does distinct centrally star forming galaxies with red disk local stellar population and star formation properties distribution compare to young, intermediate and old central stellar age?(**Chapter 2**)

2. Using the stellar photometry of M31 stars, what is the red giant branch stars metallicity distribution and gradient? (**Chapter 3**)

3. How can we improve current software tools in processing and handling large astronomical datasets and how can we leverage extensive spatially resolved spectroscopic datasets to test state-of-the-art prediction models? (**Chapter 4**)

1.1 Evolution of Mass Distribution and Shape of Nearby Galaxies

One of the most accepted explanations for galaxy evolution in a ΛCDM Universe is hierarchical structure formation where the bulges evolved at earlier epochs. This concept was originally proposed by the (Larson, 1976) and the one of the main evolutionary drivers in this model was the infall time scale of material difference in the central bulge and disk triggering star formation. Consequently, the bulge would have a shorter infall time and thus trigger star formation early in the evolution of the galaxy. These stars would eventually die and eject material in the interstellar and circumgalactic medium. The gas in the bulge would be converted to more stars until all the material is depleted only leaving a old stellar population. Meanwhile, the bulge, some of the ejected neutral gas material is now in-falling into the disk and start to condense and form a young stars across the disk. As a result, we see today galaxies with a prominent central bulge along with a disk of young stars.

The inside-out model assumes that the galaxy is isolated when in reality the evolution is dynamic. Galaxies experiences at earlier epochs from cold gas accretion, minor mergers, or violent gas instabilities and the disk interstellar medium is built up at a later epoch (Mo et al., 1998; Dekel et al., 2009; Pérez et al., 2013; Chen et al., 2020; Belfiore et al., 2017). These dynamic mechanisms physically shape the morphology and influence the star formation capabilities during the evolutionary periods. The degree of the influence on these galaxies varies widely and we see this first hand in the structure, total mass, star formation and chemical abundance distribution and their relation between each other.

The local distribution of the host galaxies for some galaxies are not fully understood and thus need to be compared to more main-stream galaxies that fit the inside-out formation model and the correlating features. The local stellar population and distribution for galaxies are direct results of their evolution. Some galaxies show distinct features and the underlying mechanisms is challenging to uncover. The interplay of stars and enriched and neutral gas tells the story of the evolution path of galaxies. However, the observational techniques to obtain the information is critical to investigate for key insights into galaxies.

1.2 Tools and Techniques

Local parameters of nearby galaxies provide a wealth of information to explore to understand the intricate details of the evolution. Integral Field Spectroscopy (IFS) allows us to observe galaxies chemical signatures on the sub-kpc scales.IFS Surveys of nearby galaxies ($z \leq 1$)

have provided a expansive 3D datacubes for over 10,000 individual galaxies. The MaNGA, CALIFA and SAMI Bundy et al. (2014); Sánchez et al. (2016a); Croom et al. (2012). The IFS surveys takes spectroscopic measurements across the surface of the galaxies using integral field units. The data products are 3 dimensional datacubes that where the X and Y represent the spatial coordinates and the Z represent the wavelength elements. Use spectroscopy and stellar population synthesis we are able to find connection between the local distribution relates to the global properties. Additionally, their a wide range of catalogs using the datasets publicly available including the Pipe3D stellar population maps Sánchez et al. (2016b).

Stellar photometry is a technique that observes stars using different filters and compute the magnitude of the stars. This information is then used to measure the color, temperature, and metallicity of the stars or a large stellar population Freedman (1986). Measuring the stars along the plane of nearby galaxies have been use the study the radial distribution using earlier techniques (see Freedman (1986) for earlier references). The Hubble Space Telescope have expanded greatly on these methods over the past 30 years and provided the high resolution stellar photometry of nearby galaxies. The Panchromatic Hubble Andromeda Treasury is one of the surveys that utilizes the advance instrumentation to study the 1/3 of stellar population in the disk of our nearest neighbor M31 Dalcanton et al. (2012, 2015); Williams et al. (2014). The survey provides multi-wavelength observations of over 10 million stars to constrain the stellar temperature, bolometric luminosity and extinction for most spectral types. A wealth of insight about the stellar evolution of M31 such as metallicity gradients Gregersen et al. (2015), the star cluster formation Johnson et al. (2016) and many others. A more recent survey called the Panchromatic Hubble Andromeda Southern TreasuryWilliams et al. (2021) aims to observe the southern half of M31 to complete the photometry catalog. In this work we combine the PHAT and PHAST catalog to measure the metallicity gradient of the RGB stars and their individual contributions to it.

Integral field unit spectroscopy and stellar photometry catalogs provide a significant amount of data and thus sophisticated software development is necessary for appropriate calibration and processing of the this data to make science ready data products. Furthermore, these data products can be utilized by applying machine learning applications to test state-of-the-art models. The MaNGA survey uses the Data Analysis Pipeline Westfall et al. (2019) and Data Reduction Pipeline Law et al. (2016) to produce science ready datacubes and emission and absorption line maps. The PHAT and PHAST catalog uses a photometry pipeline make measurements of stars and calibrate the magnitude to provide science ready catalogs.

1.3 Dissertation Outline

In the following chapters, I will described several projects that aim to shed new light on the evolution of galaxies. In Chapter 2, we investigate the radial distribution of centrally star-forming galaxies with photometrically red disks, called BreakBRD galaxies and examine there stellar population and star formation radial distribution. In Chapter 3, we use stellar photometry of RGB stars to measure the metallicity gradients of the Andromeda galaxy (M31) northern and southern half. Finally, Chapter 4 we build on the large datasets from stellar photometry and integral field unit spectroscopy and presented a photometry pipeline and deep-learning classification model.

Chapter 2

CENTRALLY STAR-FORMING GALAXIES RESOLVED RADIAL PROFILE

Chapter Summary

The spatial distribution of stellar age properties provide key insights into the dynamic evolution of nearby galaxies. Using SDSS-IV MaNGA data, we investigate how the radial stellar age and mass profiles of 11 centrally-concentrated star-forming galaxies with photometrically red disks (Breaking Bulges in Red Disks; BreakBRDs) to examine for differences in the stellar age population distribution on sub-kpc scales. We aim to clarify if the BreakBRD galaxies central stellar population is indeed younger than the disk on the resolved scales and correspond to global measurements from previous literature. We compare the distribution plots to the control parent sample of galaxies with red bulges with photometrically red or blue disks. The parent sample is then separated into centrally star-forming, centrally green-valley and centrally quiescent galaxies based on D_n4000 index as a stellar age indicator. We find that the BreakBRD galaxies show a departure in the stellar age of the outer disk but a similar central stellar age to centrally star-forming galaxies, further indicating that the red outer disk is indeed older than the central region as seen in the global measurements. The mass distribution of the BreakBRD galaxies show no main deviation providing evidence that the mass distribution does not play a pivotal role in the recent central star formation and older disk age distribution.

2.1 Motivation and Background

One of the most accepted explanations for galaxy evolution in a ΛCDM Universe is hierarchical structure formation where the bulges evolved at earlier epochs from cold gas accretion, minor mergers, or violent gas instabilities and the disk interstellar medium is built up at a later epoch (Mo et al., 1998; Dekel et al., 2009; Pérez et al., 2013; Chen et al., 2020; Belfiore et al., 2017). The mass assembly of the central bulge and, later, the outer disk is known as inside-out mass growth. Stellar population and star formation properties provide evidence that generally supports inside-out formation from cosmological models (Kepner, 1999) and observations of $z \sim 2 - 0$ galaxies(Nelson et al., 2016; Pérez et al., 2013; Delgado et al., 2013; Fernández et al., 2018; Sanchez et al., 2019; Breda et al., 2020). Inside-out formation may be one of the essential aspects of galaxy assembly and provides a general explanation of stellar population and star-formation distribution of present-day spiral galaxies. In previous studies, the peak of star formation always occurs in the inner before the outer regions, and the delay is similar in all Hubble types of an average of 2.2 Gyr (Breda et al., 2020).

Radial profiles have been used for decades to investigate the systemic variation of stellar population and chemical abundance properties of nearby galaxies (Pagel & Edmunds, 1981; Peletier & Valentijn, 1989). Integral field unit spectroscopy (IFS) studies in more recent years provide supporting evidence for inside-out formation on the sub-kpc scales. For example, the negative radial gradients of the stellar ages of spiral galaxies in the CALIFA survey Pérez et al. (2013); González Delgado et al. (2015) supports this model. Sánchez (2020) also provides evidence of inside-out formation from stellar age radial profiles separated by morphology where the averaged age of the stellar population presents a negative age gradient for all late-type spiral galaxies more massive than $10^{9.5} M_{\odot}$. Studies of early and late-type galaxies' metallicity and age gradients also found negative age and metallicity gradients that support inside-out formation Parikh et al. (2021).

However, due to the complexity of galaxy evolution from various internal and external physical mechanisms, some galaxies show evidence of central star formation and truncated or suppressed disks deviating from the inside-out formation scenario. The mechanisms that drive these star formation distributions include but are not limited to minor mergers (Hilz et al., 2013), inflow and outflow of enriched and pristine gas (Breda et al., 2020) induced from stellar feedback or ram-pressure stripping (Gunn & Gott, 1972). From these studies, no one mechanism is responsible for the shaping the galaxies evolution and their relative influence is not known. As Tuttle & Tonnesen (2020) discusses, inside-out formation is not universal particularly for lower mass galaxies ($M_{\odot} < 10^{10}$) see (Pérez et al., 2013; Pan et al., 2015; Ibarra-Medel et al., 2016). They argue that there are mechanisms that produce outside-in formation up to lower mass and that galaxies within this mass range can have a diversity of age radial profiles. The BreakBRD galaxies we are studying in this paper have a wider mass range and show evidence of younger central stellar age than their disk further explaining that inside-out formation age difference is not universal.

Over the life cycle of a galaxy, different mechanisms may influence stellar populations and star formation properties, shaping them into the present-day galaxies we observe today. This analysis aims to investigate the distribution of stellar and star formation properties in nearby galaxies that exhibit features that deviate from inside-out formation.

Tuttle & Tonnesen (2020) analyzed a sample of 129 centrally star-forming galaxies confirmed by single-fiber spectroscopy and photometrically red disk galaxies from the Sloan Digital Sky Survey (SDSS). The sample is named "Breaking Bulges in Red Disks" (BreakBRD) because of the $4000\mathring{A}$ absorption break used as a stellar age indicator (Pagel & Edmunds, 1981; Kauffmann et al., 2003a) in the central $3 arcsec$ fiber and the photometrically red disks. These features make the BreakBRD samples potential outliers of the inside-out paradigm. Additionally, the BreakBRD galaxies are in isolated and crowded environments demonstrating that the central star formation is not exclusive to high-density galaxy environments.

Global measurements from 3" single-fiber spectroscopy and photometric disk colors provide broad but limited information about the star formation and stellar population, making it challenging to perform in-depth analysis across the BreakBRD sample. Therefore, we use integral field unit (IFU) spectroscopy to examine the central and disk region on sub-kpc scales and infer their stellar population features and star formation distribution. In the past decade, integral field unit spectroscopy has allowed for detailed measurements of face-on galaxies to provide more insight into kinematics, chemical compositions, star formation distribution, and stellar population properties on sub-kpc scales (Bundy et al., 2015; Sánchez

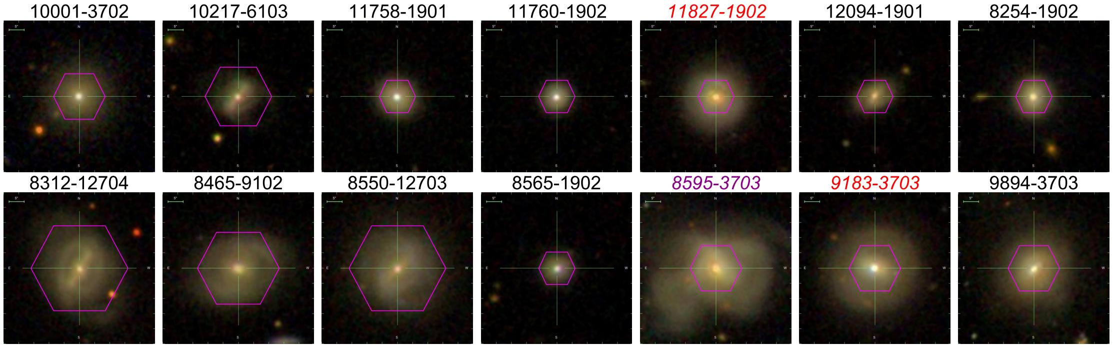

Figure 2.1: SDSS color images of the 14 BreakBRD galaxies observed by the MaNGA survey. The purple hexagon represents MaNGA FOV, and the images are titled with the unique plateifu identifier. The red labeled titles are the AGNs (11827-1902 and 9183-3703), and the purple label is the possible merger (8595-3703). These three galaxies are excluded from further analysis

et al., 2016a; Urrutia et al., 2019). We utilize these measurements across the BreakBRD sample by examining the stellar population age, star formation rate surface density, and stellar mass surface density as a function of radius from the center (radial profiles). In addition, we examine radial profiles of the BreakBRD galaxies to infer possible evolutionary paths and conditions that favor central star formation in a photometrically red disk.

This analysis compares the BreakBRD galaxies' stellar population age, mass, and star formation properties using radial profiles to controls sample of star-forming, green valley, and quiescent galaxies derived from the same parent sample. The parent sample galaxies consist of predominantly red older bulges and a blue or red outer disk. Differentiating profiles between the BreakBRD and the controlled samples could provide insight into the possible evolution scenarios that could drive central star formation in galaxies with a wide range of morphology and environments. If the BreakBRD galaxies are outliers and show recent central star formation with an older red disk, we expect to detect a noticeable difference between the samples.

2.2 Observations

2.2.1 Galaxy Sample Selection

The datasets used in our analysis are all drawn from the sample presented by (Lackner & Gunn, 2012)[LG12, hereafter] who conducted bulge-disk decomposition on local ($z < 0.05$) face-on galaxies using SDSS DR7 $3arcsec$ single-fiber spectroscopy and multi-waveband photometry. They apply a fit to either a de Vaucoleurs (classical) or an exponential (pseudo-)bulge and an exponential disk to perform a bulge-to-disk (B/T) decomposition. The LG12 sample contains 71825 galaxies with a majority of quiescent bulges and blue disks, as expected from an inside-out formation scenario, and 2.7% consisting of star-forming pseudo-bulges and red disks, the primary interest in this paper. LG12 find that two-thirds of the sample have half of their flux within the inner $3arcsec$, which means that the central bulge stellar light dominates the central fiber. Thus, throughout the remainder of our analysis we interpret the central fiber measurements as crudely analogous to the bulge stellar population and star formation.

From the LG12 sample, Tuttle & Tonnesen (2020) selected face-on galaxies with the most robust bulge-to-disk decomposition by identifying a subset with r-band absolute magnitude $M_r < -19$, axial ratio $b/a > 0.7$, and $0.2 < g - r < 0.9$ for both the bulge and disk. These cuts reduce the sample to 4643 galaxies. Specifically looking for galaxies with red disks and star-forming bulges, they consider galaxies to have a red disk if $g - r > 0.655$ and a star-forming bulge if $D_n4000 < 1.4\,dex$ in the single-fiber measurements, indicating recent star formation in the past $\sim 1Gyr$ (Kauffmann et al., 2003b). The final sample consists of 129 galaxies with star-forming bulges with a red disk called the BreakBRD galaxies.

The BreakBRD sample has a stellar-mass range of $9.9 < \log(M_\star/M_\odot) < 11.0$, with the majority of the sample above $\log(M_\star/M_\odot) > 10$. The visual morphology of the BreakBRD galaxies varies, hosting both spheroidal and barred central bulges with either diffuse or spiral disk structures. Furthermore, the environmental density measurements span a wide range and match the distribution of the parent sample (Tuttle & Tonnesen, 2020). The star-forming bulges and red disks consistently define our sample, making it an ideal dataset to investigate galaxies' outside-in evolution.

We aim to understand the differences between BreakBRD galaxies and control samples of centrally quiescent, centrally green-valley and centrally star-forming galaxies, which we define using alternative selections on the LG12 data set. We consider galaxies with $D_n4000 < 1.5$ measured in the central fiber as centrally star-forming (CSF), similar to the BreakBRD galaxies, except the CSF galaxies are not explicitly selected to have red disks. We then define our centrally quiescent (CQC) sample as galaxies with $D_n4000 > 1.75$. While this allows us to focus on the oldest and youngest central stellar populations in the LG12 sample, we include the intermediate $1.5 < D_n4000 < 1.75$ galaxies labeled as the centrally green valley (CGV) population. We use the term "green valley" as it refers to a region of color space which is populated by galaxies moving to and from the blue star-forming sequence to the red quenched sequence.

Additionally, we made stellar mass cut to the CSF, CGV and CQC samples to match the BreakBRD sample. We select galaxies with $9.9 < log(M_\star)$ <11.0 from the SDSS photometry (CSF=63, CQC=22, CGV=24, BBRD=14) and exclude the remaining galaxies from further analysis.

2.2.2 MaNGA Dataset

In order to study the spatially resolved star formation properties of BreakBRDs versus the CSF, CGV, and CQC control samples, we crossmatch these samples against the SDSS-IV Mapping Nearby Galaxies at Apache Point Observatory (MaNGA) survey (Bundy et al., 2015) to collect integral field unit (IFU) spectroscopic measurements when available. MaNGA is a 4th generation SDSS (SDSS-IV) program observed from 2014 to 2020. The goal of the study is to investigate the kinematics, structure, and composition of gas and stars for $\sim 10,000$ nearby ($z < 0.15$) face-on galaxies using integral field unit (IFU) spectroscopy. The survey provides a spectral resolution of $R \sim 2000$ in the wavelength range $3600 - 10,300\AA$. The independent fiber bundles provide 17 simultaneous observations of galaxies that feed to the BOSS spectrographs on the SDSS 2.5m telescope (Drory et al., 2015). The observations of the MaNGA galaxies were conducted to ensure all galaxies have radial coverage out to at least 1.5 times the effective (half-right) radius. A secondary sample maps galaxies out to 2.5 times the effective radius. The primary sample was color enhanced by adding 1700 galaxies designed to balance out the color distribution at fixed stellar mass (M_{star}) (Bundy et al., 2015; Wake et al., 2017). The spatial resolution is 1-2 kpc at a median redshift $z \sim 0.03$, and the target r-band SNR is $4 - 8\mathring{A}^{-1}$ per 2" fiber at 23 AB mag $arcsec^{-2}$.

MaNGA observations are first reduced through the Data Reduction Pipeline (DRP; Law et al., 2016) and then further processed through the data analysis pipeline (DAP; Westfall et al., 2019) to generate the spatially resolved maps for data analysis. These maps include stellar kinematics measurements, emission line flux density, and spectral indices. The DAP products include corresponding data quality and inverse-variance maps. The process was performed on the entire MaNGA sample and the products are publicly available.

The Pipe3D (Sánchez et al., 2016a) value-added catalog provides additional data products extracted from the DRP datacubes. The Pipe3D VAC is based on the FIT3D algorithm to perform a Continuum plus S/N binning (CS-binning) approach for the stellar population measurements because of the advantages of increasing the SNR and preserving the shape of the original target (Sánchez et al., 2015). The MaNGA galaxies are independently analyzed by the FIT3D algorithm and do not use the DAP masks. Belfiore et al. (2019) compares the differences between the DAP and Pipe3D outputs and finds no significant effects on their science case.

We use the stellar mass surface density $\Sigma_{M_\star}$, luminosity-weighted stellar age Age_{LW} maps, and integrated values from the publicly available catalog. Though Pipe3D used a different binning method than the DRP, Sánchez et al. (2016a) demonstrates that the luminosity-weighted ages and metallicity are recovered with a max precision of $\sim$ 0.1 dex to most stellar templates for the highest SNR spectra. Furthermore, the derived stellar parameters are compatible with widely used fitting routines templates making it an ideal data set for obtaining stellar population properties.

MaNGA observed 14/129 BreakBRD galaxies and 195/4643 from the LG12 sample. These samples are the primary focus of our analysis. In Figure 2.1, we show the BBRD color images from SDSS with the unique PLATE-IFU ID (plateifu) as the title. The galaxies with purple and red labels were removed from further analysis due to the presence of highly disturbed structure or active galactic nuclei (AGN; see Section 2.2.3), respectively. The purple hexagons represent the field of view (FOV) of the MaNGA fiber bundle.

From the DAP and Pipe3D data products, we are able to obtain spatially resolved maps of emission and absorption line fluxes, star formation history, stellar mass kinematics and elliptical coordinates. For our analysis, we use the $H\alpha$, $H\beta$, [OIII λ5008], [NII λ6585] emission line flux maps and D_n4000 absorption line index maps.

2.2.3 Data Reduction and Pre-processing

Resolved Dust Extinction Correction

We apply the dust extinction correction method from Calzetti (2001) to compute the intrinsic flux density for the MaNGA 2D emission line maps. We use a curve normalization $R_V = 4.05$ assuming a Case-B recombination of intrinsic Balmer decrements $Flux_{H\alpha}/Flux_{H\beta} = 2.86$. However, issues arise when $H\beta$ is much fainter than $H\alpha$, where low S/N can lead to $Flux_{H\alpha}/Flux_{H\beta} < 2.86$. Therefore, we exclude spaxels with $Flux_{H\alpha}/Flux_{H\beta} < 2.86$ from further analysis.

We first computed the observed Balmer decrements for each galaxy in the BreakBRD sample. We then adopted the Calzetti (2001) extinction curve (k(λ)) (Eq. 2.1) for $0.63\mu m > \lambda < 2.2\mu m$ and Eq.2.2 for $0.12\mu m > \lambda < 0.63\mu m$ using an curve normalization $R_V = 4.05$. The optical depth (Eq. 2.3) and gas color excess (Eq. 2.4) are computed assuming the Case B recombination intrinsic flux ratio. Finally, we calculate the intrinsic flux using Eq. 2.5. We use corrected emission line fluxes for the remainder of the data analysis.

$$k(\lambda) = 2.659 * 1.857 + 1.040/\lambda + R_V \tag{2.1}$$

$$k(\lambda) = 2.659(-2.156 + 1.509/\lambda - 0.198/\lambda^2 + 0.011/\lambda^3) + R_V \tag{2.2}$$

$$\tau = \log(\frac{(F_{H\alpha}/F_{H\beta})}{2.86}) \tag{2.3}$$

$$E(B-V)_{gas} = \frac{1.086}{k(H\alpha) - k(H\beta)} \tag{2.4}$$

$$F_{int} = F_{obs} * 10^{0.4k(\lambda)E(B-V)_{gas}} \tag{2.5}$$

Removal of AGN

$H\alpha$ luminosity typically scales with high-energy photons from massive stars and is often used as an SFR indicator; however, $H\alpha$ can also be collisionally ionized in the presents of shocks or ionizing radiation fields from active galactic nuclei (AGN). AGN processes have complex physical mechanisms that are unclear and challenging to distinguish ionization sources from each other. To ensure our global SFR estimates for the central single fiber spectrocopy are not dominated by emission from AGN activity, we use the [OIII]/$H\beta$ vs [NII]/$H\alpha$ (Baldwin et al., 1981) diagrams to identify the primary ionization's source for a stellar population in a galaxy. This diagram separates the region into AGN, composite and star forming classes (Kewley et al., 2006; Kauffmann et al., 2003a) where we exclude AGN class galaxies from further analysis. Using emission lines from the central SDSS fiber, we find that two galaxies in our MaNGA breakBRD sub-sample are AGN (marked with red titles in Figure 2.1 reducing our primary sample to 12 galaxies. Eight of the LG12 sample galaxies are AGN, reducing the control sample to 169 galaxies. The primary ionization source of the galaxies studied in this paper are shown to be dominated by star formation and composite activity (i.e. combination of starburst and AGN activity see Kewley et al. (2006)).

We also examine spatially resolved BPT maps to remove galaxies with a large fraction of AGN ionization-dominated spaxels in the central region for BBRD and LG12 samples.

The BreakBRD BPT maps vary widely between galaxies. For example, no galaxy outside those previously removed showed a high fraction of AGN spaxels in the central region. In the LG12 sample, we removed an additional four galaxies, giving us a final control sample of 138 galaxies.

Visual Inspection of MaNGA Samples

We visually inspected the BreakBRD and LG12 samples to remove galaxies showing significant disturbed features from a recent merger, crowded MaNGA FOV due to the foreground stars, and other visual anomalies. Galaxies undergoing mergers produce an undefined radial profile because of the mixing of interstellar gas suppressing or enhancing star formation from the collision with another galaxy. It is challenging to infer the stellar population and star formation rate properties from the individual spaxels. We mitigate this issue by simply removing any significantly disturbed galaxies in the color images. We then examine the spatial coverage of the BPT spaxels to remove objects with too sparse or low spatial coverage.

The BreakBRD galaxies show a range of features, as seen in Figure. 2.1 but plateifu: 8595-3703 in the bottom row indicates significantly disturbed structure in the color image; thus, we remove that object from further analysis, reducing our sample size to 11 BreakBRD galaxies. The LG12 sample also have a diverse galaxy structures and a broader range of colors than the BreakBRD sample. Therefore, we removed 58/195 galaxies, leaving 137 galaxies in the LG12 sample for further analysis.

Global Data Products

The SDSS DR7 value-added catalog provided the single-fiber spectroscopy and integrated photometric measurements of nearby galaxies. We adopt the total and fiber SFR/sSFR estimates from Brinchmann et al. (2004) who correct for galactic dust extinction and aperture effects. These estimates employ a Kroupa (2001) Initial Mass Function (IMF) and Kennicutt (1998) conversion factor between Hα flux and SFR. The stellar mass measurements were obtained from fits to the photometry using methods from Kauffmann et al. (2003a) and

Salim et al. (2007), and the fiber masses are derived from spectroscopic measurements within the $3arcsec$ central fiber.

In Figure. 2.2 we plot global data in multiple phase-space to show the relative distribution of the final BreakBRD (magenta), CQC (red), CGV (green) and CSF (blue) MaNGA samples and how they compare to the complete samples. The BreakBRD galaxies are distributed primarily with the star-forming galaxies in agreement with Tuttle & Tonnesen (2020). CSF, CGV, and CQC samples are differentiated where the CSF has a highest sSFR, SFR, and lowest D_n4000 index, the CQC sample has the highest central D_n4000, with CGV the middle-range sample. This apparent population difference provides a good comparison sample to the BreakBRD galaxies. The samples also share similar mass distributions.

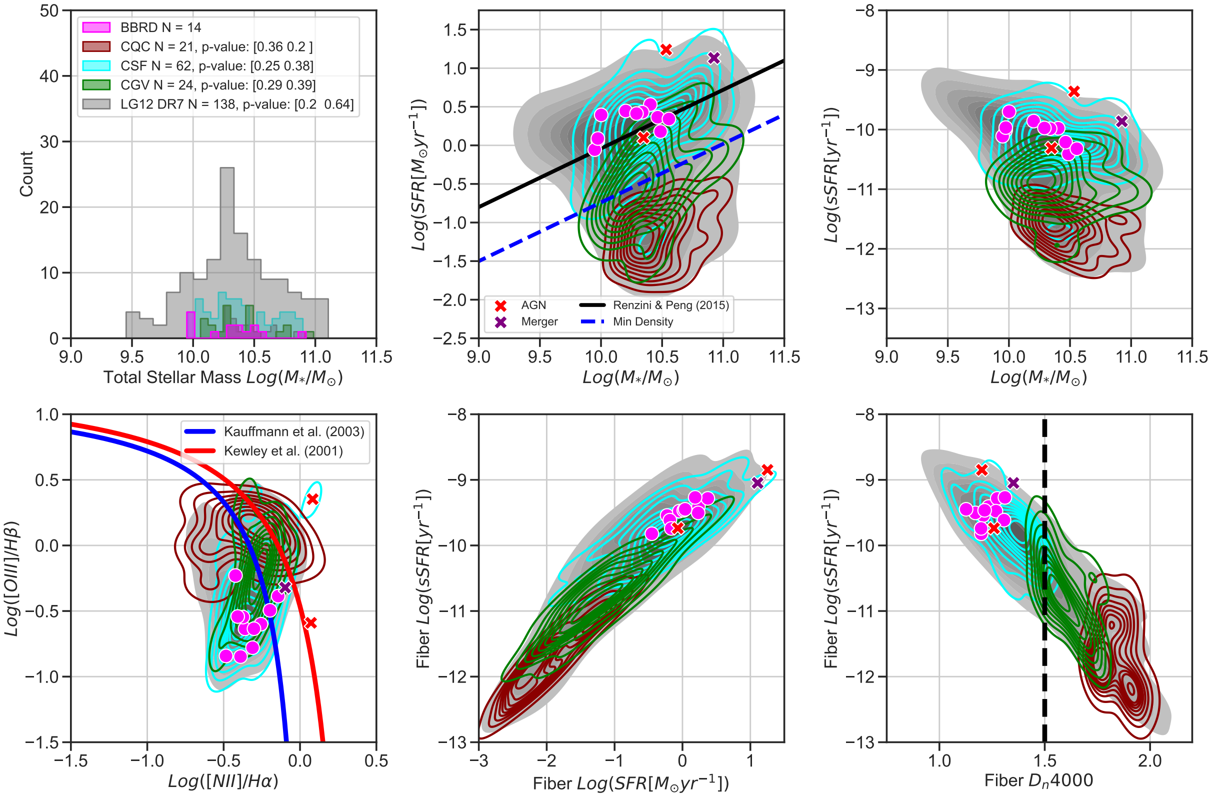

Figure 2.2: Global measurements from SDSS DR7 catalog for BreakBRD (BBRD) [magenta], LG12 centrally star-forming (CSF) [cyan], centrally green valley (CGV) [green] and centrally quiescent(CQC) [dark-red] sub-sample and the entire LG12 sample from the SDSS MaNGA sample. The red and purple [**X**] are the AGN/shock ionization dominated objects and a merger that we remove from further analysis. [**Top left:**] Total stellar mass histogram, with the legend listing the p-value from a two-sample Kolmogorov-Smirnov test between the BBRD and comparison sample. [**Top center:**] Global star-forming main-sequence where the black and blue line represent Renzini & Peng (2015) ridge-line and the minimum density line. [**Top Right:**] Total specific SFR (sSFR) vs Total stellar mass, [**Bottom Right:**] Baldwin et al. (1981) (BPT $N[II]/H\alpha$ diagnostic, where red and blue line represent Kauffmann et al. (2003a) and Kewley et al. (2006)) classification fits. [**Bottom Center:**] 3” central fiber sSFR vs fiber SFR. [**Bottom Left:**] 3” central fiber sSFR vs fiber D_n4000. We show that the LG12 MaNGA sub-sample is well distributed across the original parent sample consisting of both high and low sSFR, similar to Tuttle & Tonnesen (2020) that can be used to separate the data into star-forming and quiescent populations for comparison to the BreakBRD sample. We also demonstrate the separation in central fiber is appropriate to separate the data into star-forming and quiescent populations.

2.3 Method

2.3.1 Radial Profile

Radial profiles are created by evenly binning the IFU maps from the centre to outer disk and taking the median of values within that bin. We then plot the medians as a function of radius to examine the distribution of star formation and stellar population. We obtain the elliptical polar coordinates of each spaxel from the galaxy center by the MaNGA DAP catalog. The effective radius (R_{eff}) (half-light radii) was derived from de Vaucouleurs fit scale radii using the SDSS r-band color images. Using the elliptical polar coordinate maps and half-light radius provided by DAP, we create radial profiles for all 11 BBRD and 159 galaxies (57 CSF, 53 CQC, 24 CGV) from our parent sample. The radial profiles for each galaxy are constructed by binning the spaxels in 10 evenly separated radial intervals from the center spaxels out to 2.0 R_{eff}. We then take the median value spaxels in the bins and plot them as a function of radius. We use the R_{eff} scaled profiles to consider the population average of many galaxies and allow for the spaxels at similar positions relative to the size of the disk to get stacked together as seen in previous analysis (Bluck et al., 2020). At larger radii, the scatter in the samples becomes too large due to the lower surface brightness and signal-to-noise (S/N) and is less reliable for estimating flux surface density. Therefore, we do not use all the spaxels at R_{eff}. Further, we take median radial profile of each sample to show the overall distribution of the entire sample and compare them to the BreakBRD sample.

2.3.2 Selecting Central and Disk Spaxels

We relate the central and disk spaxels distribution in the BBRD sample to the LG12 CSF, CGV, and CQC samples. From characterization of the spatially resolved maps, the BreakBRD galaxies show the central 3 arcsecs spaxels within 0.5 effective radii have the highest surface brightness and encapsulate the central bulge. We define the central region as all spaxels with 0.5 R_{eff}. The disk of the BreakBRD galaxies extends to 1.5 - 2.5 R_{eff}. We select spaxels from 0.5 R_{eff} to 2 R_{eff} as our disk region to remove the low signal-to-noise outer spaxels of galaxies which tend to have a large scatter from our analysis.

2.3.3 BreakBRD Galaxies Outlier Comparison

The BreakBRD sample from the MaNGA survey includes 2 galaxies spatially dominated by AGN ionization and 1 possible merger identified from the false-color image. In this section, we examine the D_n4000, luminosity-weighted age (Age_{LW}) (stellar age indicator), and the stellar mass surface density of the AGN and merger samples in comparison with the other BreakBRD galaxies. AGN mechanisms produce high-energy photons, resulting in strong emission lines similar to those in star-forming galaxies. Merging galaxies redistribute the stellar population and material of a galaxy. The merger can cause central gas accretion, which promotes recent central star formation. We compare the stellar age and mass surface density distributions of the AGNs and merger galaxies with the BreakBRD galaxies, where the central bulge features a young central population and an older outer disk.

In Figure 2.3, we show the radial profiles of the merger, the 2 spatially dominated AGN galaxies, and the 11 BreakBRD galaxies. We also illustrate the distribution for $R = 0 - 0.5R/R_{eff}$ and $R = 0.5 - 2.0R/R_{eff}$, which we refer to as the central and disk regions, respectively. The samples are clearly separated by age across all radii, with the AGNs, BreakBRD, and merger galaxies showing a range from younger to older stellar population ages. All three samples exhibit a similar central stellar population age profile.

Figure 2.4 presents the stellar mass surface density radial profiles for the 11 BreakBRD, merger, and 2 AGN galaxies. The merger and AGN samples exhibit approximately ~ 0.5 dex higher mass surface density across all radii compared to the BreakBRD galaxies. The outer disks of all three samples are wider than the centers and overlap in mass surface density.

Comparing the 11 BreakBRD galaxies with the excluded AGN and merger samples, we find that the stellar population age and mass surface density are clearly separated in radial profiles. The AGN galaxies show younger stellar populations in both age indicators and higher stellar mass surface densities across all radii. The merger galaxy exhibits an older

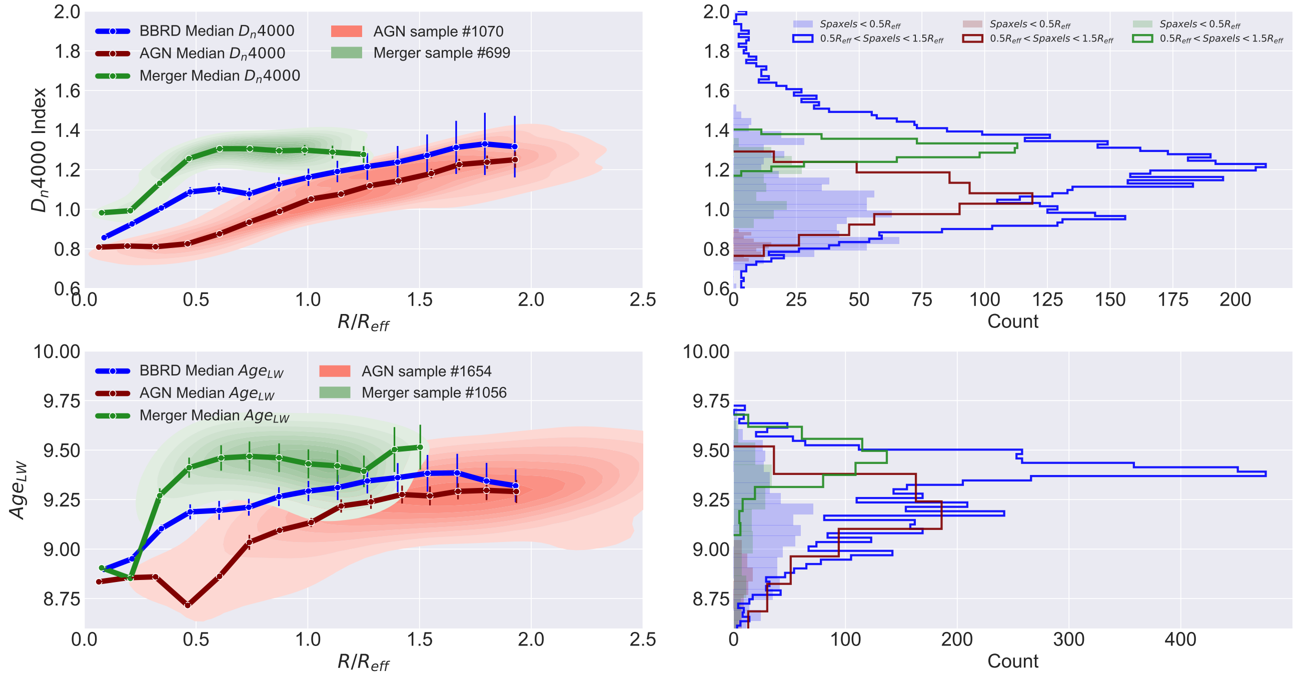

Figure 2.3: D_n4000 and luminosity-weighted stellar ageAge_{LW} radial profiles of the 11 BreakBRD galaxies(Blue) and the excluded BreakBRD, merger(green) and AGN(red) sample galaxies that we (left column) and the central$(0.0 - 0.5R/R_{eff})$ and disk $(0.5 - 2.0R/R_{eff})$ distribution (right). The error bars are the 1σ (standard deviation) for the spaxels in the radial bins. In the histograms, the filled in histograms represent the central spaxels than and the transparent histograms are the disk. The samples show a clear difference in stellar age radial profile where the merger has the oldest stellar population, the BreakBRD are intermediate and the AGN have the youngest stellar population. The radial profiles are increasing indicating recent central star formation resulting in a younger stellar population age while the disk has an older stellar population in agreement with previous analysis.

stellar population across all radii compared to the BreakBRD and AGN galaxies. This is evident in the histograms of the central and disk distributions. We conclude that these galaxies exhibit features similar to the BreakBRD galaxies but could contribute to a higher stellar mass distribution and possibly have no significant impact on the stellar age radial distribution.

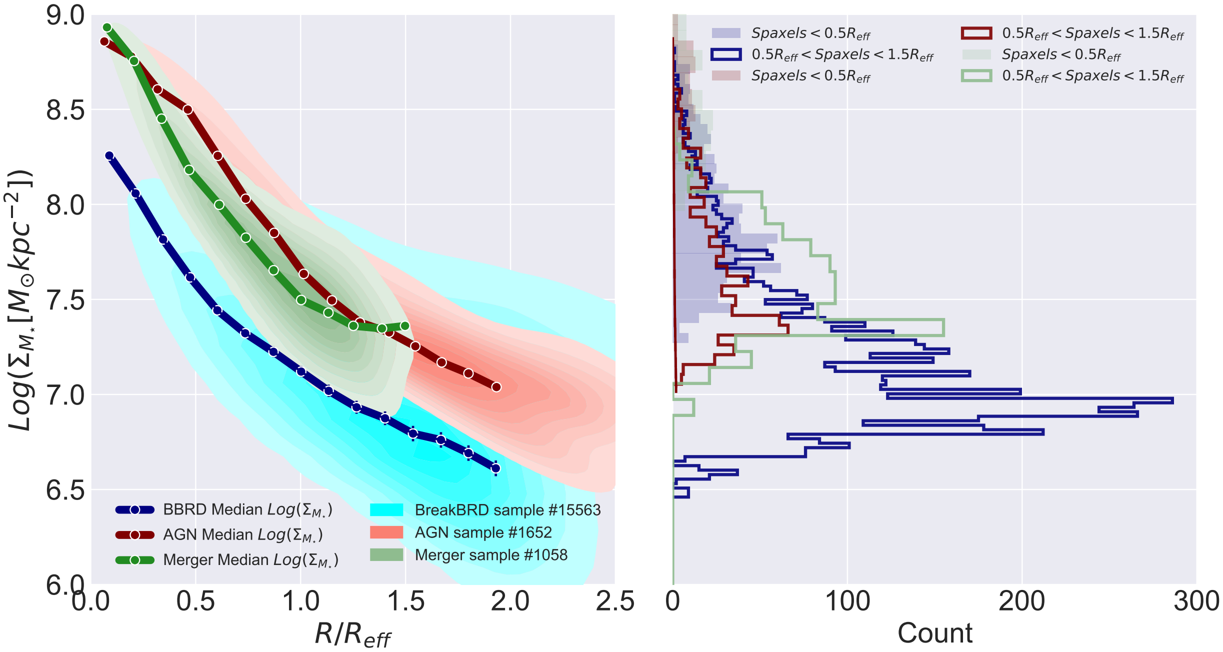

Figure 2.4: Stellar mass surface density ($\Sigma_{M_\star}$) radial profiles of the 11 BreakBRD galaxies(Blue) and the excluded BreakBRD, merger(green) and AGN(red) sample galaxies that we (left column) and the central($0.0-0.5R/R_{eff}$) and disk ($0.5-2.0R/R_{eff}$) distribution (right). In the histograms, the filled in histograms represent the central spaxels than and the transparent histograms are the disk. The samples show a clear difference in $\Sigma_{M_\star}$ radial profile where the merger and AGN are higher than the BreakBRD galaxies. The radial profiles show a monotonic decline to lower mass in agreement with the inside-out mass assembly of galaxies.

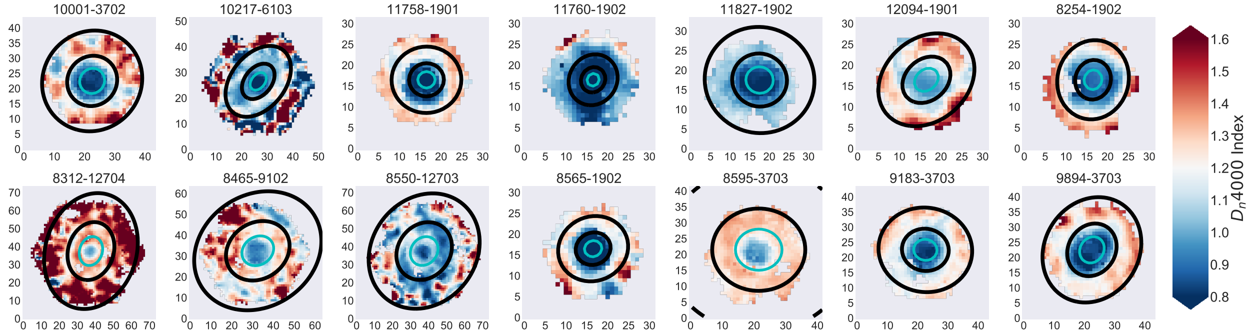

Figure 2.5: The D_n4000 index spatial maps for the BreakBRD galaxies. The color from blue to red represent low to high D_n4000 index (young to older stellar population from recent star formation within $\sim 1Gyr$ ago). The cyan represent the 3 arcsec similar to the FOV of the SDSS single fiber spectroscopy. The black lines represent the 0.5 and 1.0 R_{eff}. Noticeably, all the BreakBRD galaxies show a younger stellar population age in the center than region suggesting recent star formation localize in the center.

2.4 Analysis

2.4.1 Stellar Populations

In this section we describe our stellar age and mass radial profiles and distribution of the BreakBRD and our controlled sample. In Section 2.4.1 we use the D_n4000 provided by the MaNGA datacubes and the Luminosity-weighted stellar age (Age_{LW}) from Pipe3D catalog Sánchez et al. (2016a). In Section 2.4.1 we discuss the stellar mass assembly of nearby galaxies and how the Pipe3D provided the measurements we use for our analysis.

Stellar Age

Nearby galaxies ($z < 1$) show a clear bi-modality in to star forming and quiescent galaxies which can be seen multiple phase space diagram that compare star formation rate or age of the stellar population with the integrated stellar mass or absolute magnitude. These diagrams include the D_n4000-Mass (Blanton & Moustakas, 2009) where D4000 is an age indicator derived from the 4000$\mathring{A}$. The 4000$\mathring{A}$ break is the strongest discontinuity in the optical spectrum due to a large number of spectral lines in a narrow wavelength range, produced from metal absorption on the atmosphere of old and cool stars and a reduced flux from younger hot stars. Thus, we can associate a high $4000\mathring{A}$ break with an older stellar population and a low $4000\mathring{A}$ break with a younger stellar population (Kauffmann et al., 2003a). The D4000 index is defined as the ratio of the average flux density in bands $4050 - 4250\mathring{A}$ and $3750 - 3950\mathring{A}$ (Bruzual A., 1983). The D_n4000 index as defined in Balogh et al. (1999) takes narrower bands (4000-4100 and 3850-3950$\mathring{A}$) than the D4000 index, which has the advantage of being less sensitive to reddening effects. This index depends somewhat on metallicity but correlates more with the ratio of the present to past-averaged star formation rates in galaxies (Gallazzi et al., 2005). The D_n4000 is known to be a good indicator of stellar population ages with a mean $<\sim 1Gyr$ which corresponds to $D_n4000 < 1.4 - 1.5$ (Kauffmann et al., 2003b). From the global measurements as mentioned in Section 2.2.1, all galaxies in the BreakBRD sample have central fiber $D_n4000 < 1.4$, indicating that the central star formation occurred recently. Therefore, we use the D_n4000 absorption index as a stellar population age indicator in our analysis. Belfiore et al. (2019) provide the D_n4000 spatial map for MaNGA that we use in our analysis.

The luminosity-weighted stellar age (Age_{LW}) maps were derived from averaging the best models derived from linear combination of synthetic stellar populations templates as explained in Sánchez et al. (2016b). The luminosity-weighted stellar age highlight the contribution of young stellar population with a strong color effect that a (Sánchez et al., 2015) and is considered to be the first momentum of star formation and chemical enrichment histories in logarithm scale. We note the age is corrected by dust attenuation law (Cardelli et al., 1989) but this method may not be the best for star-forming galaxies compared to Calzetti (2001) however no significant difference were observed when adopting either method. Pipe3D catalog provides the spatial maps for our samples we use them throughout the analysis see Sánchez et al. (2015) for further explanation.

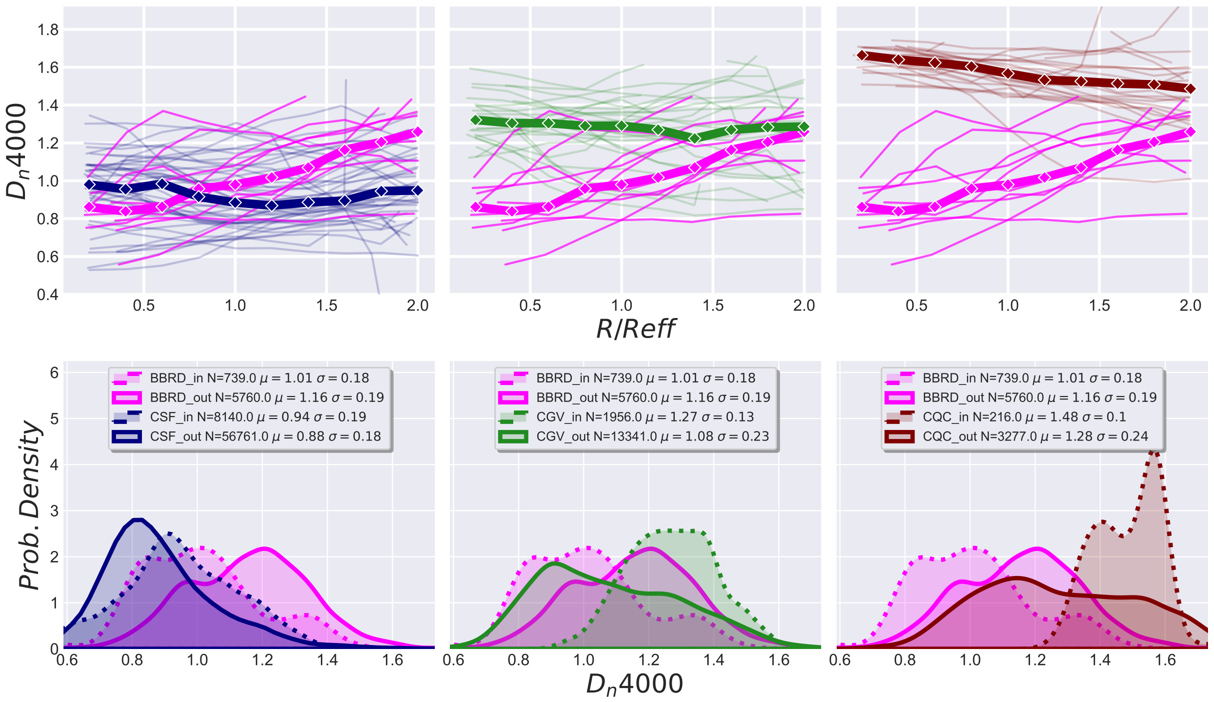

Figure 2.6: **Top**D_n4000 index as a function of effective radial bin (radial profile). The individual lines are the profiles for each galaxy in the sample and the solid line is the frequency weighted median of the entire sample. **Bottom** probability density distribution of the inner ($R < 0.5R_{eff}$) and outer ($0.5R_{eff} < R < 2.0R_{eff}$) spaxels represented as dashed and solid lines respectively. From left to right, we show how the CSF(blue), CGV(green) and CQC(red) radial profiles compare to the BBRD (magenta) profiles. The BreakBRD galaxies shows a more pronounce incline than the CSF, CGV and CQC indicating that the stellar age evolution from the inner to outer radii is shifting from a younger to an older stellar population in contrast to inside-out formation. However, the CSF, CGV and CQC samples show a flat profile which also contrast to the inside-out declining stellar age distribution.

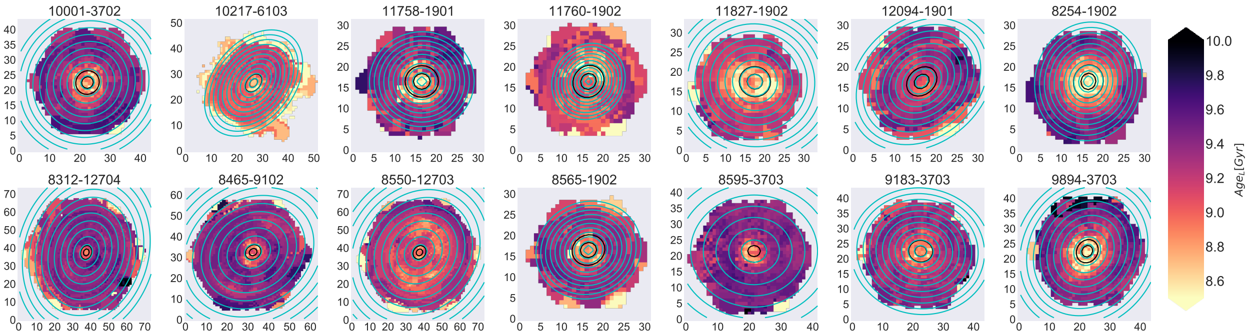

Figure 2.7: Example of the radial bins from 0-2.0 effective radial for the BreakBRD galaxies. The spatial maps are the stellar population age from Pipe3D catalog.

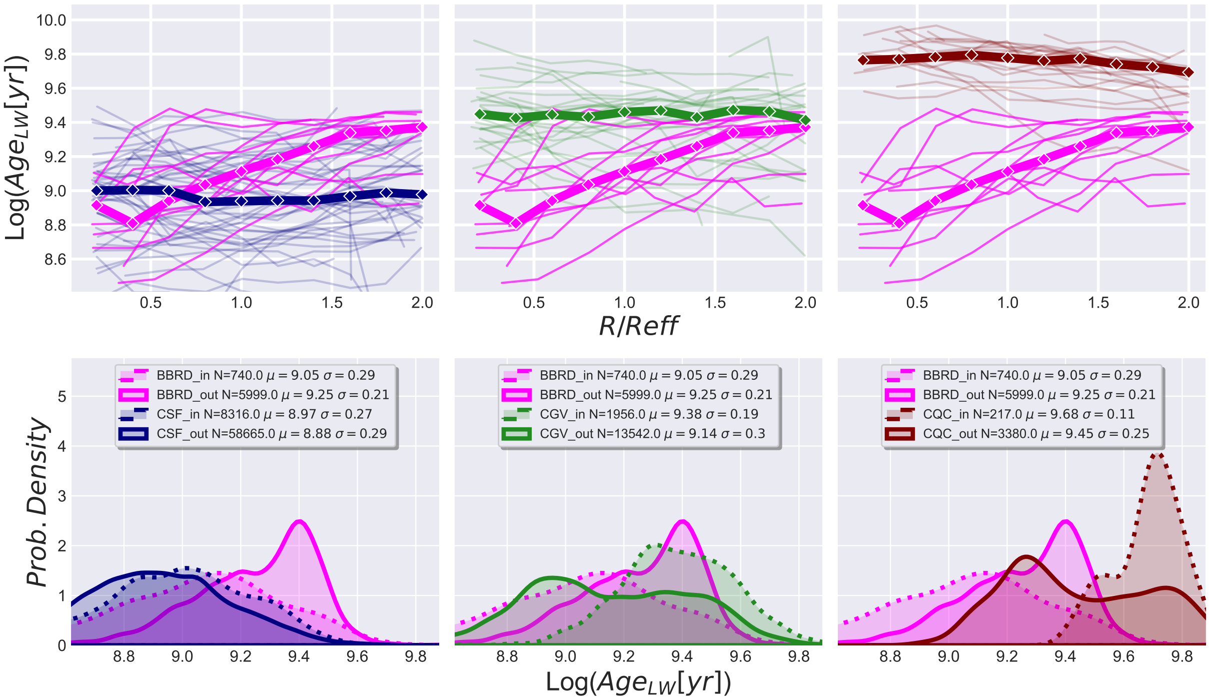

Figure 2.8: The Luminosity-weighted Stellar Age Log(Σ_{SFR}) as a function R_{eff} and R_{ellip} following the same nomenclature and color scheme of Figure 2.6. The CSF and CQC samples reside at a younger stellar age and older ranges and show a flat R/R_{eff} radial profile on average and do not reflect that expected decreasing stellar age from inside-out formation. The BBRD sample is younger than the CQC sample at a given R/R_{eff} radii, indicating that there is possible continuous star formation across the galaxies. Additionally, the BBRD sample shows a noticeable increase in stellar age than the CSF in agreement central concentration of star formation and older redder disk in contrast to inside-out formation. The radial profiles in kpc show that the CQC sample has a decreasing radial profile consistent with what we expect from inside-out formation. However, the CSF consistently has a flat radial profile, indicating how younger stars could obscure the older stellar population in the center. The BBRD galaxies show a steep increase from the nuclei to 3 kpc and a relatively flat profile at larger radii. The bottom row of histograms further shows that the CSF and BBRD sample occupies a similar stellar age distribution, and the BBRD disk spaxels are in an intermediate range to the CSF and CQC galaxies. We assert that the BBRD galaxies deviate in the age profiles from CSF and CQC samples regardless of radial scale and show an increase to a flat stellar age radial profile. Recent gas inflow could induce the younger stellar age in the central region. The timescale for the gas to reach the outer disk is significantly longer, thus showing the disk to appear older. The older disk could also indicate signs of the suppression of star formation from outside-in quenching.

Stellar Mass

The mass assembly is a complex relationship between many internal and external activities, including merging, gas accretion, and stellar feedback. A decreasing stellar mass surface density is consistent with a central bulge formed at an earlier epoch and, more recently, in the disk (i.e., inside-out formation). The radial distribution is well-known to have a monotonic decline in surface brightness radial profiles (SBP) for all galaxies almost independently of stellar mass, evolution history (i.e., galaxy merger), or present-day morphology (Sánchez, 2020). The SBP is thought to be directly related to the monotonic decline in stellar mass ($\Sigma_{M_\star}$). Therefore, this argues that a decrease in $\Sigma_{M_\star}$ radial profiles is a consequence of the inside-out scenario in agreement with the literature (González Delgado et al., 2015). The stellar mass surface density maps are provided by the Pipe3D catalog where they integrate the mass over cosmological time to that of the age of the galaxy. The mass is then corrected for mass-loss and mass lock into remnants for a given age and metallicity (see Sánchez et al. (2015) for further details). We use the stellar mass surface density to examine the mass distribution and compare the stellar mass to SFR, known as the star-forming main sequence.

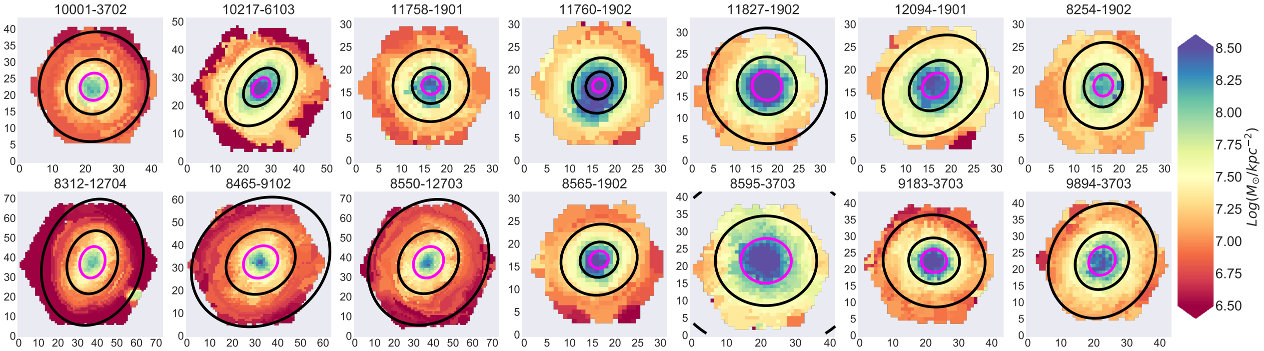

Figure 2.9: Stellar Mass Surface Density Map for the BreakBRD Galaxies. The magenta ellipse represents the 3 arcsec radius the black line represent the 0.5 and 1 R_{eff}. The BreakBRD galaxies show and inside-out mass distribution where the mass is centrally concentrated and significantly drop to lower mass surface density.

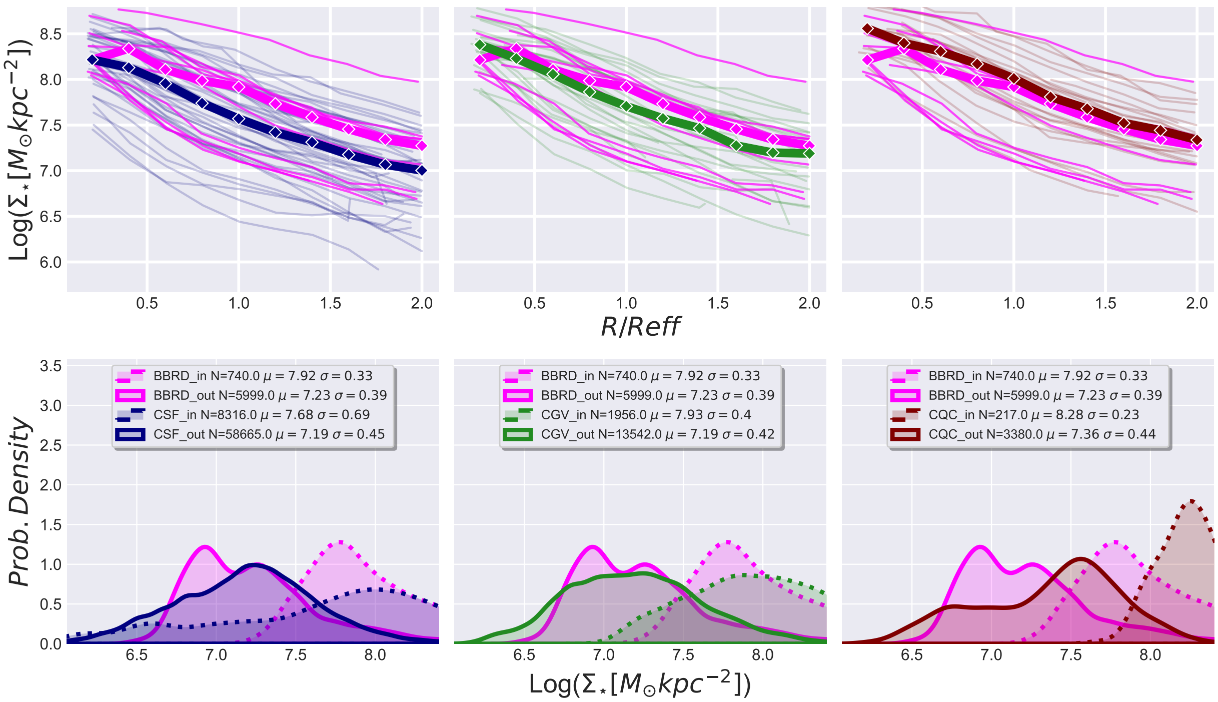

Figure 2.10: The stellar mass surface density Log($\Sigma_{M_\star}$) as a function R_{eff} and R_{ellip} following the same nomenclature and color scheme of Figure. 2.6. All 3 samples overlap in distribution but follow a similar monotonic decline from the center to the disk. The BreakBRD galaxies do not significantly deviate from the control samples suggesting that mass assembly may not play a major role in central star formation activity. The BBRD central spaxels are shown to be concentrated 7.7 Log($\Sigma_{M_\star}$) and have a narrow distribution in stellar mass density.

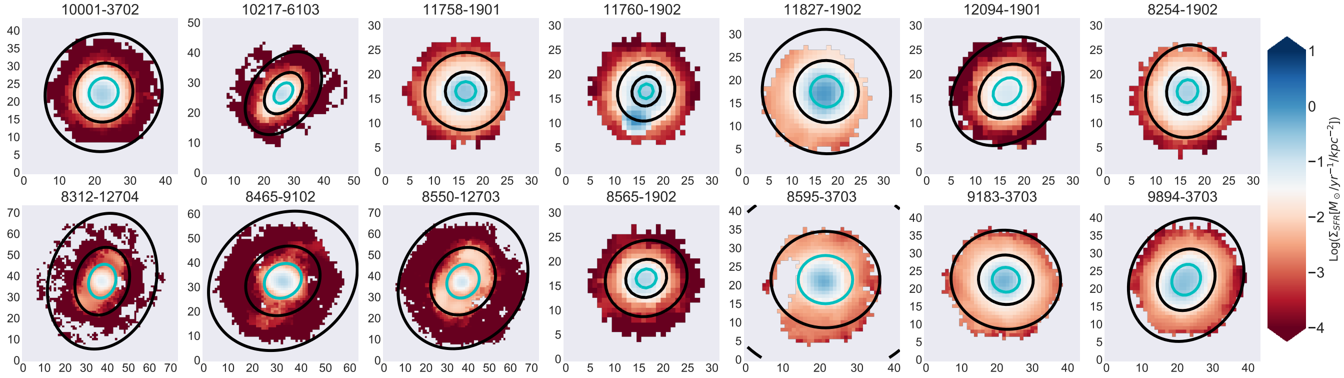

Figure 2.11: The star formation rate surface densityLog (Σ_{SFR}) spatial map for the BreakBRD galaxies where the black is the 1 and 3 arcsec and the cyan ellipse represent the $0.5Reff$. The maps show a clear peak in Log(Σ_{SFR}) in the center and decrease to the outer region. The galaxies with spiral arms and central bars structure appear spatially in the maps suggesting a change in star formation activity.

2.4.2 Star Formation Distribution

In this section, we discuss the analysis star formation indicators we use to show the the star formation rate, efficiency and enhancement using spatial resolved measurements for the BreakBRD galaxies and the comparison with the CSF, CGV and CQC samples similar to the previous section.

Star Formation Rate Surface Density

The star formation surface density profile allows us to examine recent star formation activity using the $H\alpha$ emission as a tracer. We compare the star formation rate radial profiles of the BreakBRD sample to the CSF, CGV, and CQC samples. The star formation rate in this analysis is probing 100 Myr or of recent star formation. We apply the $H\alpha$ to SFR conversion definition from Kennicutt et al. (1994) to the $H\alpha$ maps. Figure 2.11 we present the BreakBRD galaxies $\Sigma_{SFR}[M_\odot yr^{-1} kpc^{-2}]$ maps we used to make our radial profiles and compare to the parent sample.

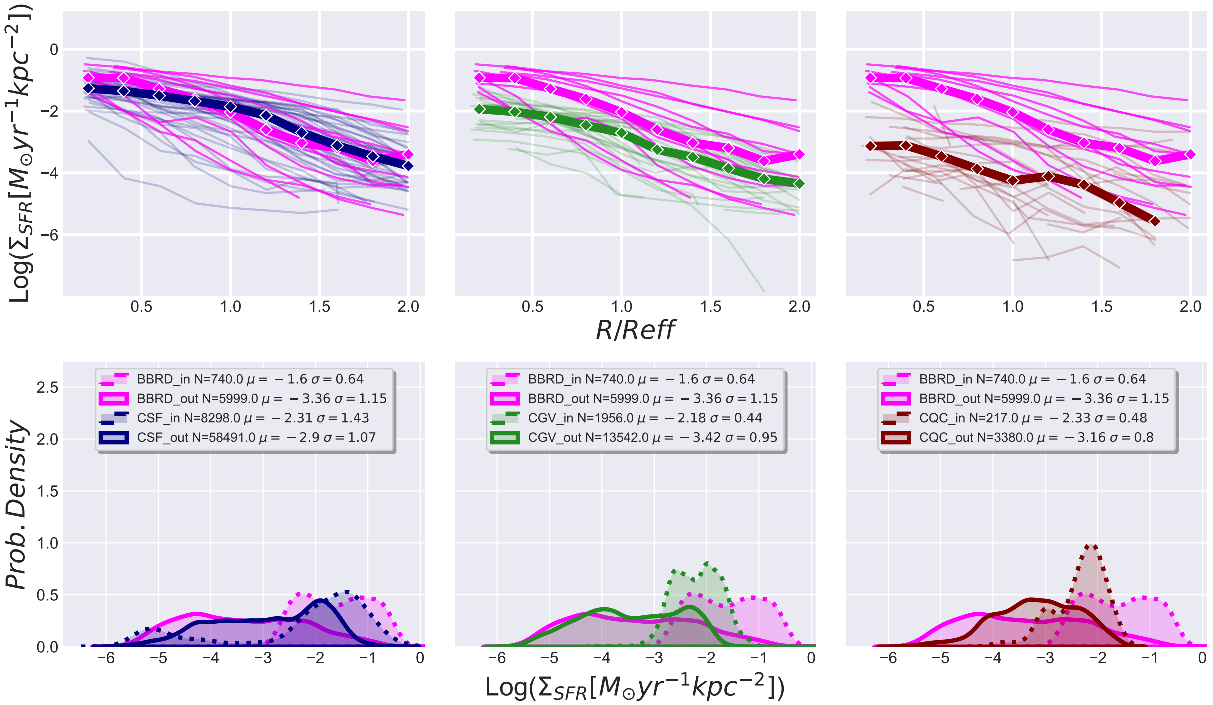

Figure 2.12: The star formation surface density $\mathrm{Log}(\Sigma_{SFR})$ as a function R_{eff}. The BreakBRD sample resides primarily with the star-forming galaxies with a decreasing star formation surface density profile. Each sample shows a decreasing radial profile, but the BreakBRD and CSF galaxies' central regions have a higher star formation than the CGV and CQC galaxies indicating a recent star formation activity in the BreakBRD galaxies. In the bottom panels, we compare the spaxel distribution. The BreakBRD galaxies central spaxels are distributed similar to the CSF galaxies as seen from radial profiles while the CGV and CQC distribution peak are ~ 1 dex lower hinting that the BreakBRD and CSF have more central recent star formation activity than the CGV and CQC. The star formation distribution of the disk for all samples are within a similar range. The BreakBRD disk spaxel mean is ~ 0.4 and ~ 1 less than the CSF and CGV but ~ 0.2 higher than the CQC sample. This demonstrates that the disk star formation less active than the CSF and CGV sample but more than the CQC sample. We note where the the CGV sample has the lowest mean indicating least star formation activity. However, this is due to a single galaxy that has the oldest disk which impacts the distribution and does not mean that the CGV sample have less star formation activity than the CQC galaxies. The results from this analysis support that the central region of the BreakBRD has experienced recent star formation similar to the star forming and green valley galaxies while the disk does shows a wider range of star formation rates.

Specific Star Formation Rate Surface Density

Specific star formation surface density can be interpreted as the amount of time required to form the current stellar mass at the current SFR (Sánchez, 2020; González Delgado et al., 2015). For common values of 10^{-11} $M_{\odot}$/yr this means that the current star formation rate surface density requires about a hundred Gyr to form the current stellar mass surface density. These values are especially common in early-type galaxies, as in agreement with the observations of Speagle et al. (2014). Thus we investigate the BreakBRD galaxies' sSFR radial profiles to the LG12 for insight into the star formation rate efficiency(SFE). This allows us to normalize the SFR surface density profiles from Figure 2.12 by the stellar mass profiles (Figure 2.10).

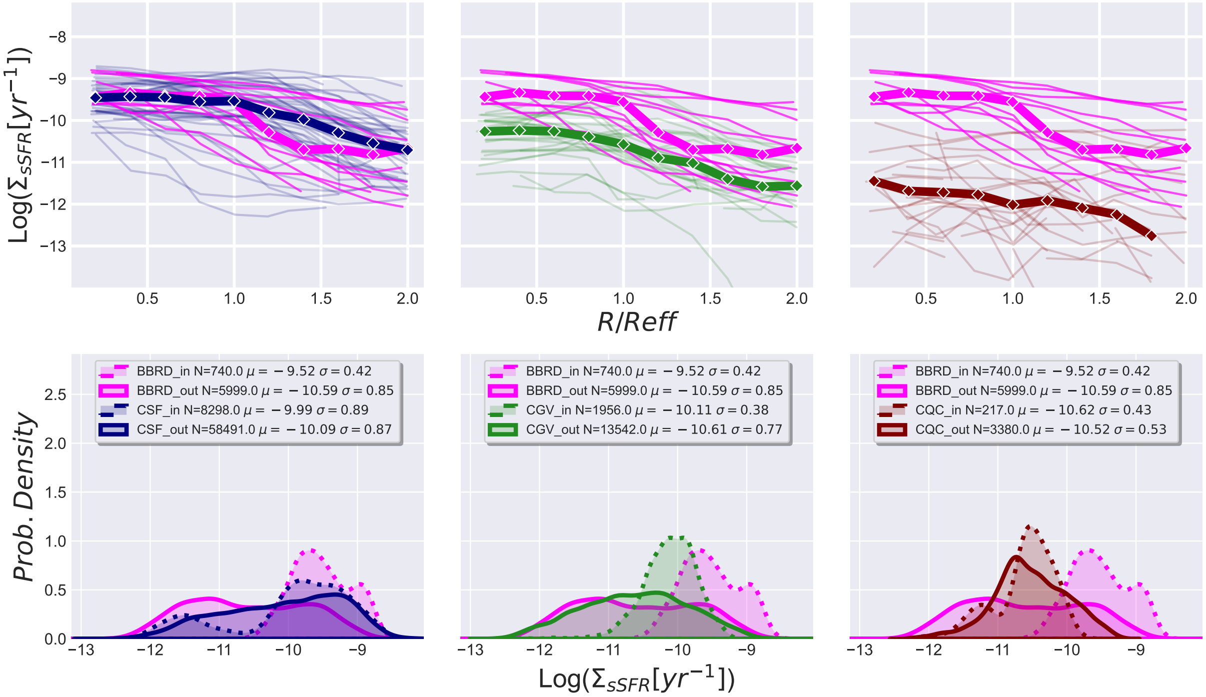

Figure 2.13: The specific star formation surface density Log(Σ_{sSFR}) as a function of effective radial bin (radial profile). The individual lines represent the profiles for each galaxy in the sample, and the solid line is the frequency-weighted median of the entire sample. **Bottom**: Probability density distribution of the inner ($R < 0.5R_{eff}$) and outer ($0.5R_{eff} < R < 2.0R_{eff}$) spaxels, represented as dashed and solid lines, respectively. From left to right, we show how the CSF (blue), CGV (green), and CQC (red) radial profiles compare to the BreakBRD (magenta) profiles. The BreakBRD galaxies reside primarily with the CSF galaxies; however, the BreakBRD median profile shows a steeper decline in star formation efficiency after 1 R_{eff}, indicating a decrease in star formation efficiency as a population in the disk. Further, the BreakBRD and CSF galaxies have higher Log(Σ_{sSFR}) than the CGV and CQC galaxies at all radii. This suggests that the BreakBRD galaxies have a star formation rate efficiency sufficient to maintain high star production as a population in both the central bulge and outer disk. Notably, the BreakBRD galaxies exhibit a steep decline in star formation efficiency that is not observed in the other galaxy samples. This is the main feature of the BreakBRD galaxies, where the central region has a younger stellar population while the disk has an older population, confirming this feature on a spatial scale in the sub-kpc range. From the PDF plots, the distribution of the BreakBRD galaxies' central region has the lowest average compared to the CSF, CGV, and CQC samples, while the disk spaxels are distributed similarly to the CGV sample. This further suggests that the central region, as a population, has a higher star formation efficiency than the disk. All the sample disks have a narrower distribution in the central region compared to their disks, indicating that the disks have a wide range of efficiencies. CSF and BreakBRD exhibit the largest distribution, which could relate to the variety of star-forming spiral galaxies with changing efficiency across the disk.

In Figure 2.13 we show the radial profiles of the parent sample split into age bins with the BreakBRD galaxies. The BreakBRD sample radial profiles reside with the star-forming galaxies profiles at higher specific star formation rate surface density Σ_{sSFR} than the CQC sample in the R_{eff} radius scale. BreakBRD galaxies sSFR plateau in the central to outer region before noticeably dropping $0.1dex$ indicating the central regions have stable and more efficient star formation production than the disk where the stellar population is older and have less star formation. BreakBRD and CSF both plateau to 1 R_{eff} but then the CSF drops more gradually than the BreakBRD galaxies suggesting that the efficiency of the disk star formation suddenly changes.

The distribution of central spaxels for the BBRD and CSF samples overlaps well, although the BBRD galaxies have a larger fraction of central spaxels with $\log(\Sigma_{sSFR}) < -10.5yr^{-1}$. The majority of CQC samples reside below $\log(\Sigma_{sSFR}) = -10.5yr^{-1}$ However, the disk spaxels are distributed across a broader range for the CSF, CQC, and BBRD samples indicating a breath of stellar populations in the disk but not a noticeable difference. We can infer that the central region takes a similar amount of time to form the current stellar mass as CSF galaxies. The disk has a large scatter because of the wide range of star formation processes supported by the vast stellar population ages, as shown in Figure. 2.8.

2.4.3 Metallicity

The gas-phase metallicity is used to measure the relative abundance of oxygen to hydrogen to infer the chemical evolution of the HII region where new stars are created. In addition, metallicity provides information about the regulation of outflow properties of metals from the interstellar medium (ISM). The inflow of neutral gas dilutes metal content while outflow removes metals (Teklu et al., 2020). The metallicity of a galaxy is expected to decrease if the outflow of gas is enriched beyond the current ISM.

(Kewley et al., 2019) explains that oxygen is the dominant element by mass in the Universe and is the principal nebular coolant. As a oxygen cools, collisions excitation become fewer, and the strength of the excitation becomes weaker, resulting in the lines becoming anti-correlated with gas-phase metallicity. Numerous studies investigate the gas-phase metallicity estimates and the strengths and weakness using different metallicity calibrated diagnostic (see, Kewley & Dopita (2002) and reference therein). Thus we can use gas-phase metallicity to examine for hints of metal loss from outflows. It is expected that an isolated star-forming galaxy with no interaction of the inter-galactic medium will increase metallicity with age from supernovae winds and stellar feedback as a result of star formation.

We examine multiple oxygen abundance diagnostic, O3N2, N2, N2O2 to analyze their metallicity radial distribution. Examining the discrepancies between methods is beyond the scope of this work. In this section, we provide an overview of the radial profiles of the BreakBRD and parent sample. We note that the differences between diagnostics can highlight potential issues with the ionization state, nitrogen enrichment, or other factors.

O3N2 diagnostic

We use the metallicity calibration based on the O3N2 based index as defined from Pettini & Pagel (2004). The main advantages and disadvantages for IFU spectroscopy can be found in the in literature (Kewley & Dopita, 2002; Sánchez et al., 2014; Belfiore et al., 2017; Poetrodjojo et al., 2018). We apply the diagnostic to the emission line maps to create the metallicity map for galaxies in the BreakBRD and parent sample. The metallicity gradient of O3N2 metallicity diagnostic has shown to be shallow negative decrease as a function of radius in previous sub-kpc scale analysis.

In Figure 2.14 we present the BreakBRD galaxies oxygen abundance metallicity($Log(O/H)+12$) map. We use these maps to produce the metallicity radial profile. The spatial maps looks to have a higher metallicity in the central region and gradually decrease to lower metallicity.

$N2H\alpha$ Diagnostic

The $[NII]/H\alpha$ metallicity diagnostic as defined in Kewley & Dopita (2002) as a crude metallicity estimator. e apply the diagnostic to the emission line maps to create the metallicity map for galaxies in the BreakBRD and parent sample. The metallicity gradient of $N2H\alpha$

metallicity diagnostic has shown to be shallow negative decrease as a function of radius in previous sub-kpc scale analysis. In Figure 2.16 we present the $N2H\alpha$ metallicity map for the BreakBRD galaxies. The maps look spatially seamless across all radii for most galaxies and some galaxies show minor structure in the inner radius.

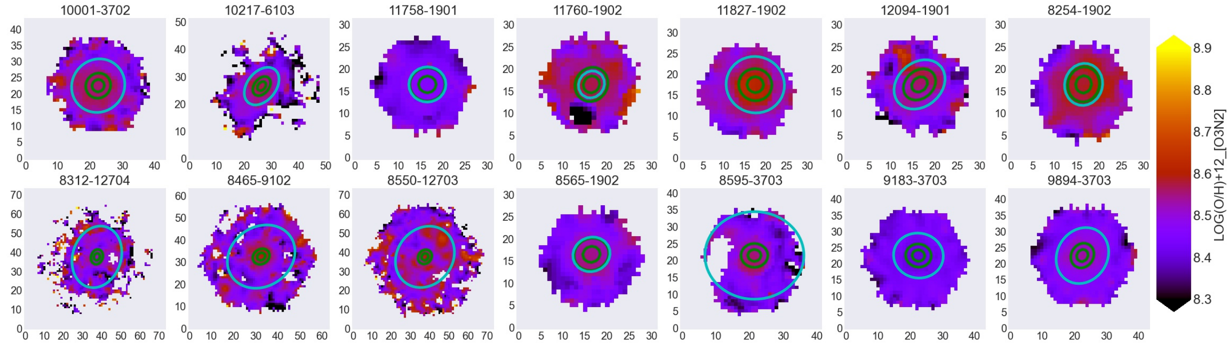

Figure 2.14: The O3N2 metallicity diagnostic $(Log(O/H) + 12[O3N2])$ spatial map for the BreakBRD galaxies where the green is the 1 and 3 arcsec and the cyan ellipse represent the 0.5 R_{eff}. The metallicity distribution appears to be consistent at all radii with noticeable high metallicity region in the outer disk of individual galaxies.

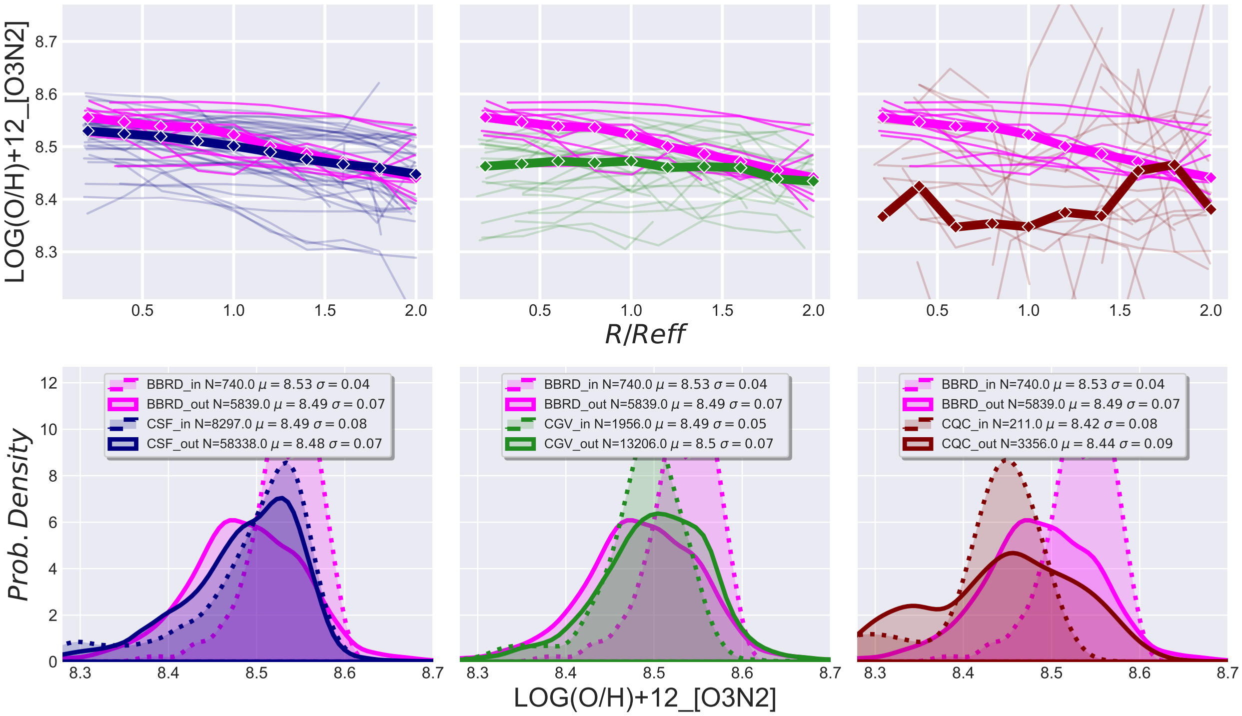

Figure 2.15: **Top**$Log(O/H)+12[O3N2]$ index as a function of effective radial bin (radial profile). The individual lines are the profiles for each galaxy in the sample and the solid line is the frequency weighted median of the entire sample. **Bottom** probability density distribution of the inner ($R < 0.5R_{eff}$) and outer ($0.5R_{eff} < R < 2.0R_{eff}$) spaxels represented as dashed and solid lines respectively. From left to right, we show how the CSF(blue), CGV(green) and CQC(red) radial profiles compare to the BBRD (magenta) profiles. BreakBRD galaxies as a population have a shallow deceasing radial profile similar to the CSF galaxies suggesting a similar distribution of metallicity as star forming galaxies. The radial profile of the BreakBRD galaxies show higher metallicity at all radii than the CGV and CQC galaxies though they converge to similar metallicity at larger radii. The CQC is shows high scatter making it less reliable to draw a conclusion for the sample as a whole. We expect the sample to have a higher metallicity but CQC appears to have less reliable measurement and could highly affected by dust attenuation and future analysis will explore this feature. The distribution of the central region for the BreakBRD galaxies show a more metal rich distribution than the disk which is aligns with inside-out formation where the metal enrichment is higher due to the star formation on a longer time scale than the disk. The BreakBRD galaxies do not noticeably variate from the CSF galaxies indicating that the recent central star formation and red outer disk feature could be independent of this metallicity distribution.

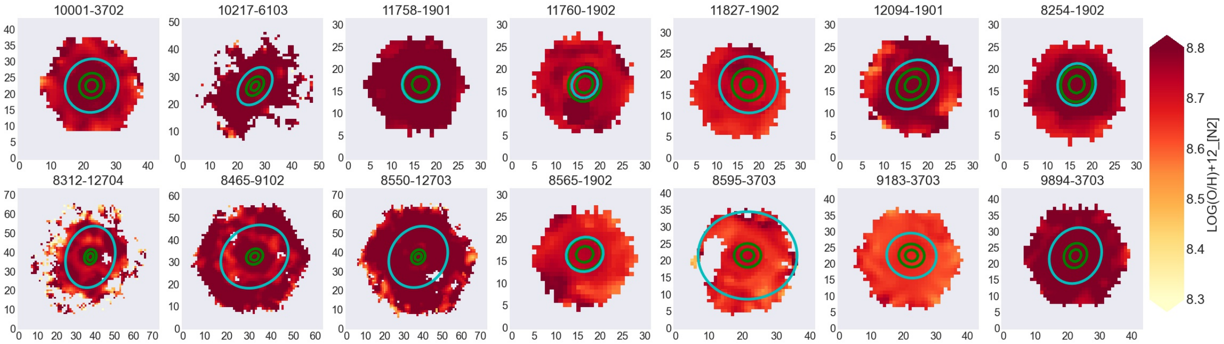

Figure 2.16: The N2 metallicity diagnostic ($Log(O/H) + 12[N2]$) spatial map for the Break-BRD galaxies where the green is the 1 and 3 arcsec and the cyan ellipse represent the 0.5 R_{eff}. The metallicity distribution appears to be consistent at all radii.

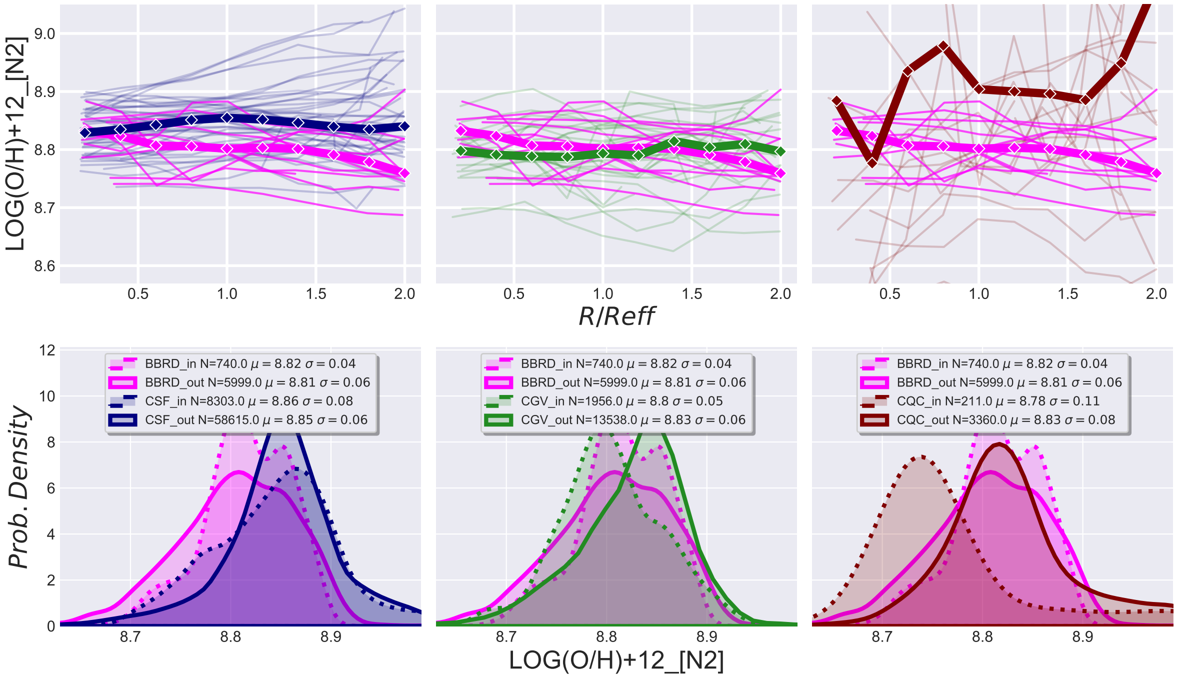

Figure 2.17: **Top**$Log(O/H)$+12$[N2]$ index as a function of effective radial bin (radial profile). The individual lines are the profiles for each galaxy in the sample and the solid line is the frequency weighted median of the entire sample. **Bottom** probability density distribution of the inner ($R < 0.5R_{eff}$) and outer ($0.5R_{eff} < R < 2.0R_{eff}$) spaxels represented as dashed and solid lines respectively. From left to right, we show how the CSF(blue), CGV(green) and CQC(red) radial profiles compare to the BBRD (magenta) profiles. BreakBRD galaxies radial profiles a shallow decrease indicating a central region is more metal rich than that of the disk. The BreakBRD galaxies profile aligns closely with CGV sample though the BreakBRD galaxies have slightly metal richer central region than that of the CGV galaxies before converging in the disk to $\sim 8.8Log_{10}(O/H) + 12$ and diverging in the outer disk of $\sim 0.2dex$. The BreakBRD and CGV share a similar metallicity radial profile in the N2 diagnostic. The BreakBRD galaxies have a $< 1dex$ difference at $\sim 0.6R_{eff}$ outward suggesting that the sample has a slightly metal poor distribution in the N2 diagnostic. Though the central and disk metallicity distribution overlap in value. The BreakBRD do not show a noticeable difference from the CSF and CGV but future research will take a closer look into the interplay of the N2 metallicity diagnostic and the underlying stellar population.

N2O2 Diagnostic

The N2O2 diagnostic involves the ratio of the [N II] to [O II] emission lines. This ratio is sensitive to the nitrogen-to-oxygen ratio (N/O) and, consequently, to the metallicity. It is useful because it directly compares two key elements whose relative abundances are known to vary with metallicity. However, it can be more challenging to use due to the wider wavelength separation of the involved lines, which makes it more susceptible to dust attenuation effects. We used the [NII]/[OII] optical diagnostic method as defined by Kewley & Dopita (2002) because it is known to be the most reliable measurement of oxygen abundance. The advantage is that both emission lines have similar ionization potential; thus, the ratio is independent of the ionization parameter.

In Figure 2.18 we show the oxygen abundance metallicity map using the N2O2 diagnostic. The maps vary in distribution where some have an almost seamless constant metallicity from inner to outer region, others show high metallicity concentration in the central region and decreasing at larger radii. Interestingly, some of the BreakBRD galaxies show the metallicity structure outlining the spiral arms and central bar.

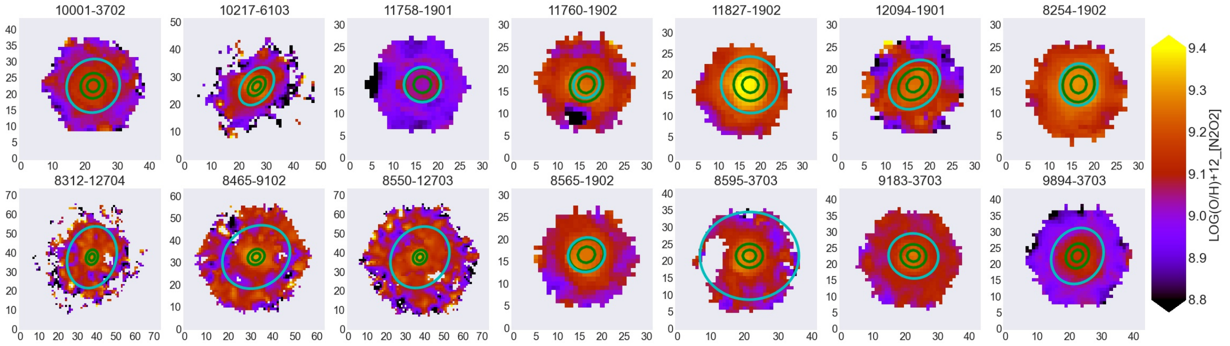

Figure 2.18: The N2O2 metallicity diagnostic ($Log(O/H) + 12[N2O2]$) spatial map for the BreakBRD galaxies where the green is the 1 and 3 arcsec and the cyan ellipse represent the 0.5 R_{eff}. The central region has a concentration high metallicity and consistent metallicity distribution. The disk metallicity has wider metallicity distribution.

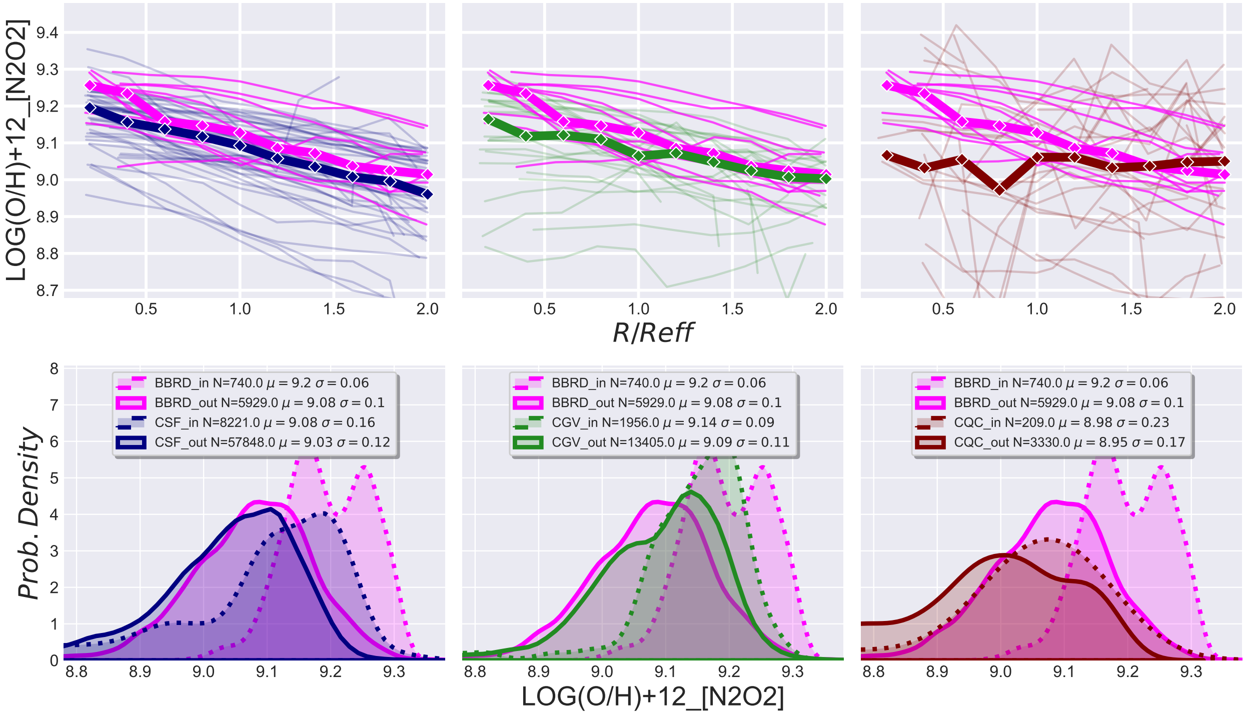

Figure 2.19: **Top**D_n4000 index as a function of effective radial bin (radial profile). The individual lines are the profiles for each galaxy in the sample and the solid line is the frequency weighted median of the entire sample. **Bottom** probability density distribution of the inner ($R < 0.5R_{eff}$) and outer ($0.5R_{eff} < R < 2.0R_{eff}$) spaxels represented as dashed and solid lines respectively. From left to right, we show how the CSF(blue), CGV(green) and CQC(red) radial profiles compare to the BBRD (magenta) profiles. BreakBRD galaxies radial profiles a shallow decrease indicating a central region is more metal rich than that of the disk. The BreakBRD radial profile have noticeably higher metallicity than CSF, CGV and CQC though the disk is most similar to that of the CSF sample. The higher metallicity is distinct and could have some implication in the difference of central age and disk. The distribution of the BreakBRD galaxies are bi-modal due to limit number of galaxies in the sample and could be due to 2-3 galaxies. Those galaxies with the higher metallicity in the central region deviate the most from the the other galaxies samples. We interpret this as the BreakBRD galaxies central metallicity could be experiencing some metal enrichment from more recent star formation isolated in that zone. The disk metallicity radial profile and distribution for the BreakBRD galaxies aligns with the CSF, CGV and CQC sample not showing any signs of metallicity enhancement nor suppression.

2.5 Results

In this section, we discuss the results for the analysis of the radial profiles of stellar age and mass maps of the BreakBRD sample against centrally old (CQC), intermediate (CGV), and young (CSF) stellar ages as determined by single fiber spectroscopy as discussed in Section 2.2.1. The color code for Figures 1-4 are the same. In these figures the top panels show the radial profiles of each sample plotted. The thin lines show the median values for individual galaxies, and the thick lines are the sample medians. The bottom row shows the probability density function (PDF) of all the spaxels in central and disk region: the central region ($R_{eff} < 0.5$) is the dotted PDF, and the outer or disk region ($0.5 < R_{eff} > 2.0$) is the solid PDF. The number of pixels in each distribution, as well as the arithmetic mean and standard deviation are listed in each panel.

2.5.1 Stellar Population Age Radial Distribution

D_n4000 *Index Radial Profile*

In the top row of Figure 2.6 we compare the LG12 centrally star-forming (CSF), centrally intermediate (CGV), and centrally quiescent (CQC) to the BreakBRD samples D_n4000 radial profiles to examine their local average stellar age distribution in the centre and disk.

The sample median of the CSF, CGV and CQC samples show a clear separation in average stellar age distribution where CSF have a younger age than the CQC sample by $D_n4000 \sim 0.6$ and the CGV is between the two samples similar to the global measurements. The age distribution for the samples look relatively flat across radii though the the individual profiles show varying degrees of increasing and decreasing radial profiles. Interestingly, the BreakBRD sample profile shows a clear increasing profile of $D_n4000 \sim 0.3$. The individual also shows nearly all having increasing radial profiles of varying degree and with one that is flat.

Further, we examine the central and disk distribution of the samples. The central stellar age population distribution of the CSF, CGV and CQC are clearly distinct and occupy the young, intermediate and older areas of the D_n4000 as show in the radial profiles. The disk stellar population is broader for all 3 samples

The increase to older stellar population age from the center to disk suggest that the BreakBRD galaxies have a young central age and older disk. The local and global stellar population are in agreement and shows that the evolution of the stellar population is distinct from different age regimes as shown by the CSF, CGV and CQC sample.

Instead of showing the average radial profiles of all the galaxies in our sample, we instead consider the D_n4000 of each pixel in the inner (dotted) and outer (solid) regions (bottom panels), we find that all three of the comparison samples have more high D_n4000 spaxels in the central 0.5 R_{eff} than in the outer regions, indicating that these samples tend towards inside-out galaxy formation. Interestingly, although the radial profiles indicate tighter D_n4000 sequence in the CQC galaxies, the distribution of spaxels values is the most broad in CQC. This may indicate that every galaxy has a minority of low D_n4000 pixels that are unable to bring down the median value in most radial bins.

The BreakBRD average radial profile shows a clear increasing radial profile from inner to outer radii. Broadly, this suggest that the BreakBRD galaxies are centrally younger than their outer disk. This is in agreement with the global measurements from the single fiber measurements. The central stellar age distribution of the BreakBRD galaxies are similar to the star forming galaxies and the disk region stellar age deviates at $R/R_{eff} > 1.0$. Compared to the CGV and CQC samples the BreakBRD galaxies have a younger stellar age at any given radii on average. This analysis suggest the BreakBRD stellar population age evolution in the center does not deviate significantly from star forming galaxies but the stellar population gets noticeably older but not as old the CGV and CQC sample. In the next section, we use another stellar population age indicator to confirm our findings.

Luminosity-weighted Age Radial Profile

In Figure 2.8, we show the Sánchez et al. (2016b,a) Pipe3D luminosity-weighted stellar population age radial profiles. The luminosity-weighted age allows us to take into count the contributions from stars at different ages and weight them by their luminosity unlike D_n4000 where it is most sensitive to young hot stars typically from recent star formation. Similar to Figure 2.6, the LG12 CQC, CGV and CSF samples clearly separated in stellar age at a given radius. The median profiles of the stellar population age of the sample are flat at a given radii but the individual profiles show varying slopes within a given age regime. The central star-forming CSF sample resides below $Log(Age_{LW}) = 9.5yr^{-1}$ consisting of a wide variety of radial profiles. The CGV galaxies tend to lie between the CSF and CQC. Like the CSF population, CGV galaxies have a broader distribution of radial profiles, indicating that the CQC galaxies have the tightest age sequence. The CQC sample shows consistently flat profiles at $Log(Age_{LW}) >\sim 9.5yr^{-1}$ at given radii. The probability distribution of the central regions show clear separation in stellar age and the outer disk has a much wider distribution and overlap across different age regimes. Notably that the central region are distributed at older age regime than the outer disk for all sample and the CSF sample inner and outer distribution shows the most similarity as described by the distribution mean. The older central stellar population and young population in the disk is agreement with inside-out formation though not conveyed clearly in the radial profiles.

The BreakBRD median radial profiles show a noticeable positive compared to the CSF, CGV and CQC samples as seen in magenta in Figure 2.8 from $Log(Age_{LW}) \sim 8.9 - 9.4yr^{-1}$ ($\sim 0.5dex$). The median profiles does not look similar to any of the sample median profiles at different ages and the individual BreakBRD galaxies, while having a variety of slopes, have increasing stellar ages with radius in all but one galaxy. It is therefore valuable to consider the slopes of each galaxy in addition to the median profiles. The BreakBRD profiles reside primarily with CSF sample age at a given radii and the disk converge with CGV sample disk age. The disk does not reach stellar ages as old as CQC sample median profile though a few individual profiles overlap with BreakBRD galaxies. We show that the BreakBRD sample does not follow any sample despite having a similar central distribution as CSF and D_n4000 range, possible signs that the BreakBRD galaxies have more recent star formation resulting in a younger stellar population compared to the CSF, CGV and CQC sample. In the bottom row of Figure. 2.8, The BreakBRD central stellar age distribution align with the ages of the CSF sample while the disk age are distributed at an older age and is an opposite relationship than what we observe form the CSF, CGV and CQC galaxies.

2.5.2 Stellar Mass Surface Density

The BreakBRD sample $\Sigma_{M_\star}$ radial profiles in Figure 2.10 show clear evidence of a monotonic decrease that agrees with inside-out formation. All 4 samples overlap in stellar mass at a given radius, though the CQC and CGV samples are distributed towards a higher mass surface density than the CSF and BreakBRD samples. We note that the flattening or increase in the median $\Sigma_{M_\star}$ at large radius for most of the samples is due to a lack of data for the lower mass galaxies, and the slope of individual galaxies consistently decrease with radius. Although the median BreakBRD distribution lies above the CSF galaxies and below the CGV and CQC galaxies, BreakBRD galaxies have overlapping distributions with all three comparison populations. The similarity between the 4 populations is also seen in the pixel value distributions shown in the bottom panels. The BreakBRD sample does not significantly deviate from the control samples, indicating no significant change in the mass assembly, and therefore their current state of centrally younger stars may not play a major role in these galaxies' earlier evolution.

2.5.3 Star Formation

Star Formation Rate Surface Density

In Figure 2.12 each sample shows a decreasing radial profile. The BreakBRD central spaxels tend to reside with star-forming samples primarily. BreakBRD galaxies vary widely in radial profiles and do not relate to one another in the half-light radius scale. There is a large scatter in the disk spaxels due to the lack of reliable $H\alpha$ measurements at larger radii.

The central spaxels span 1.5 dex with an arithmetic mean = -1.6 $Log(\Sigma_{SFR})$. The disk spaxels overlap the central spaxels and span an 8 dex range with a mean = -3.38 $Log(\Sigma_{SFR})$.

The BreakBRD overlap in star formation rate between the BreakBRD and CSF in the central region supports recent star formation. The disk spaxels overlap a wide range of star formation rates. We find that the 3 samples have a variation of linearly decreasing $Log(\Sigma_{SFR})$ which is broadly in agreement with inside-out formation (Sánchez, 2020) because of the expected different amount of gas supply in the central region versus the disk. Furthermore, the BreakBRD sample shows a noticeably steeper increasing slope than the flat CSF and CQC samples, suggesting the outer disk consists of an older stellar population.

- The BreakBRD galaxies have a gradual decrease of about $\sim 2dex$ Σ_{SFR} similar to the CSF galaxies suggesting continuous star formation rate similar to present-day star-forming galaxies. Recent star formation

- The BreakBRD galaxies sample as a population has a higher star formation rate than the CGV and CQC sample at all radii but the rates converge at larger R_{eff}. Specifically, $\sim 0.7dex$ and $\sim 1dex$ respectively in the central region. This is further suggest there is ongoing star formation with BreakBRD. Though, we note that there is overlap in the disk star formation rate when examining individual galaxies.

- The central distribution of the BreakBRD galaxies Σ_{sSFR} span $\sim 2dex$ and share overlap star formation rate with all samples though mainly suggesting on going ongoing star formation rate in all groups.

- BreakBRD galaxies disk Σ_{SFR} spans the widest range of $\sim 6dex$ spanning overlapping the CSF, CGV and CQC sample suggesting that the BreakBRD are being affected by a range of mechanisms that varies the star formation production in the disk

Star Formation Efficiency

In Figure 2.13 we show the BreakBRD sample have a central plateau in star formation efficiency in the central region out to 1 R_{eff} before decreasing in star formation efficiency of $\sim 0.5dex$ and then plateau. The BreakBRD and CSF galaxies have a similar radial profiles indicating that star central region is more efficient at forming stars than the disk for population. Further the CSF galaxies outer radius has a more gradual decline in Σ_{sSFR} and has a higher median value than that of the BreakBRD galaxies suggesting that the disk is noticeably less efficient than that of CSF galaxies. The outer radii of the BreakBRD galaxies have a median closer to the CGV sample though still slightly higher.

We interpret the following as results from the Σ_{sSFR} analysis:

- BreakBRD central region has a similar star formation rate efficiency as star-forming galaxies while the disk share efficiency similar to green-valley galaxies

- The sudden decrease in disk is further confirmation that the BreakBRD have a younger star formation population than the disk as seen from the difference in star production

- The BreakBRD galaxies have a higher efficiency in star formation at all radii than the CQC and CGV suggesting on-going star formation in both the central region and the disk.

- The BreakBRD shows to have efficient star formation and that the disk is not on average old but instead just older than the central region

- The central distribution of the BreakBRD galaxies Σ_{sSFR} span $\sim 3.5dex$ and share overlap in efficiency with all samples though mainly with CSF and CGV suggesting that the mechanisms that regulate the star formation in the CSF and CGV are more liking shaping the the efficiency of the BreakBRD galaxies than that of the CQC sample.

- BreakBRD galaxies disk Σ_{sSFR} spans the widest range of $\sim 6dex$ spanning overlapping the CSF, CGV and CQC sample. This is difficult to interpret since it does not gravitate to one population. The wide range of star formation efficiency outcomes cannot be tied to a handful of mechanisms.

2.5.4 Metallicity

O3N2 Diagnostic

We draw our main results of the raidal distrubution of the BreakBRD galaxies compared to the parent sample (CSF, CGV and CQC galaxies) from Figure 2.15. We highlight these results below:

- BreakBRD galaxies as a population have a shallow deceasing radial profile similar to the CSF galaxies suggesting a similar distribution of metallicity as star forming galaxies
- The radial profile of the BreakBRD galaxies show higher metallicity at all radii than the CGV and CQC galaxies though they converge to similar metallicity at larger radii.
- The CQC is shows high scatter making it less reliable to draw a conclusion for the sample as a whole. We expect the sample to have a higher metallicity but CQC appears to have less reliable measurement and could highly affected by dust attenuation and future analysis will explore this feature.
- The distribution of the central region for the BreakBRD galaxies show a more metal rich distribution than the disk which is aligns with inside-out formation where the metal enrichment is higher due to the star formation on a longer time scale than the disk.
- The BreakBRD galaxies do not noticeably variate from the CSF galaxies indicating that the recent central star formation and red outer disk feature could be independent of this metallicity diagnostic

N2 Diagnostic

We draw our main results of the radial distribution of the BreakBRD galaxies compared to the parent sample (CSF, CGV and CQC galaxies) from Figure 2.17. We highlight these results below:

- BreakBRD galaxies radial profiles a shallow decrease indicating a central region is more metal rich than that of the disk.

- The BreakBRD galaxies profile aligns closely with CGV sample though the BreakBRD galaxies have slightly metal richer central region than that of the CGV galaxies before converging in the disk to $\sim 8.8 Log_{10}(O/H) + 12$ and diverging in the outer disk of $\sim 0.2 dex$. The BreakBRD and CGV share a similar metallicity radial profile in the N2 diagnostic

- The BreakBRD galaxies have a $< 1 dex$ difference at $\sim 0.6 R_{eff}$ outward suggesting that the sample has a slightly metal poor distribution in the N2 diagnostic. Though the central and disk metallicity distribution overlap in value.

- The BreakBRD galaxies do not show a noticeable difference from the CSF and CGV but future research will take a closer look into the interplay of the N2 metallicity diagnostic and the underlying stellar population.

N2O2 Diagnostic

We draw our main results of the radial distribution of the BreakBRD galaxies compared to the parent sample (CSF, CGV and CQC galaxies) from Figure 2.19. We highlight these results below:

- BreakBRD galaxies radial profiles a shallow decrease indicating a central region is more metal rich than that of the disk.

- The BreakBRD radial profile have noticeably higher metallicity than CSF, CGV and CQC though the disk is most similar to that of the CSF sample. The higher metallicity is distinct and could have some implication in the difference of central age and disk.

- The distribution of the BreakBRD galaxies are bi-modal due to limit number of galaxies in the sample and could be due to 2-3 galaxies. Those galaxies with the higher metallicity in the central region deviate the most from the the other galaxies samples. We interpret this as the BreakBRD galaxies central metallicity could be experiencing some metal enrichment from more recent star formation isolated in that zone.

- The disk metallicity radial profile and distribution for the BreakBRD galaxies aligns with the CSF, CGV and CQC sample not showing any signs of metallicity enhancement nor suppression.

2.6 Discussion

Our results suggest that the BreakBRD samples' stellar age distribution deviates from the controlled parent sample convention, exhibiting an increasing stellar age profile from the center to larger radii. This divergence provides evidence that the central region possesses a younger stellar population as a consequence of recent star formation. harbors stellar ages within the range of young to intermediate, none are as old as those found in the quiescent population. The stellar age distribution of the BreakBRD galaxies' disks suggests ongoing star formation, albeit not as recent as in the central regions. Further, the BreakBRD stellar mass distribution align well with all sample showing a monotonic decline from the center to the disk suggesting that the mass assembly as describe by inside-out formation does not play a critical role in the stellar population age distribution of these galaxies. In summary, the BreakBRD galaxies are shown to be centrally star forming galaxies with an older but continuous star forming disk galaxies in the global measurements from Tuttle & Tonnesen (2020) and spatially resolved scales as demonstrated in this analysis.

Inside-out formation in galaxies dictates that the central bulge formed first and the disk formed at a later epoch (Mo et al., 1998; White & Frenk, 1991; Brook et al., 2007) thus expecting declining local stellar age as a function of radius. This is thought to apply to early and late-type galaxies.

Early and late-type galaxies with mass $M_\star > 10^{9.5} M_\odot$ have also had decreasing Age_{LW} radial profiles with varying slopes supporting inside-out formation Sánchez (2020). Previous work emphasizes that there is no consensus on the age gradients slope partly due to various techniques for deriving stellar age. Stellar mass surface density and metallicity radial profile also show decreasing radial profile independent of morphology type from a sample of 300 CALIFA surveys of early and late-type galaxies González Delgado et al. (2015). Additionally, they provide evidence that these galaxies support the inside-out scenario and show further evidence arguing that the central region is more compact in mass than in light.

The increasing profiles for centrally star-forming galaxies could result from young, luminous O and B-type stars overwhelm the spaxel flux surface density and washing out the older stars produced from recent star formation activity. The BreakBRD, on average, shows steeper increasing profiles than the CSF and CQC sample. The BreakBRD galaxies have a central stellar age distribution similar to the CSF sample but show an older population in the outer spaxels. However, this does not explain the steeply increasing profile of the BreakBRD galaxies compared to the CSF. Examining the profiles on individual polar radial scales, we find a noticeable sharp increase in spaxels at a radius less $<\sim 4kpc$ followed by a flat to steady increasing average stellar age. This analysis suggests that BreakBRD galaxies shift to older stellar populations from the center to larger radii. The cause of this feature is currently unclear, and we examine the local stellar mass and star formation properties for more insight into their evolution. The increasing stellar age radial profile of BreakBRD galaxies reinforces the hypothesis from Tuttle & Tonnesen (2020) that recent star formation activity is primarily concentrated in the central region, resulting in a younger central stellar population.

Though the stellar age profiles of our sample do not appear to support inside-out formation, the stellar mass surface density radial profiles for the all samples show a monotonic decreasing radial profile consistent with inside-out mass growth. Nearby galaxies are known to have a monotonic decline regardless of stellar mass and type. They are directly correlated to the surface brightness profile via the conversion of mass-to-light ratio (Bakos et al., 2008;

Bell & de Jong, 2001). Further, the radial profiles can be separated by mass and Hubble type to provide insight into various evolution histories as seen in Sánchez (2020); González Delgado et al. (2014, 2015).

The BBRD samples do not display significant deviations that could provide strong evidence of for a change in mass assembly. This relation holds for the individual profiles and the sample median profile. The BreakBRD samples' stellar mass surface density shows varying decreasing slopes. It could be linked to any one of the physical properties of the individual galaxies, but the small sample size does not allow us to make a more general assumption about the sample. The central and disk distribution also align with the CSF, CGV and CQC sample.

The BBRD galaxies' mass assembly agrees with inside-out formation. However, it may not play a major role in the central concentration of star formation activity for the BreakBRD galaxies and suppression in the disk. We investigate the star formation surface density radial profiles of the BBRD, CSF, CGV and CQC, which show a similar monotonic decrease to the stellar mass surface density radial profile and agree with inside-out formation. The profile shape is believed to be due to the differential amount of gas supply in the bulge and disk as a result of increased timescales of gas infall with galactocentric distance (assuming a constant depletion time across the disk) as described by the Schmidt-Kennicutt law (Kennicutt et al., 1989; Schmidt, 1959). The BBRD sample does not show an apparent deviation in the radial profile that would clearly explain the central concentration of star formation and the young stellar population. The BBRD sample resides with the CSF galaxies. In contrast, the CQC sample has a lower star formation surface density in agreement with other previous literature (Sánchez, 2020; González Delgado et al., 2015) because early-type galaxies are shown to have fewer star-forming regions and overall less star formation activity. The star formation surface density radial profiles of the BBRD, CSF, and CQC galaxies vary widely. They do not show similar patterns, which is possibly driven by the stellar mass and morphology differences (Sánchez, 2020).

We reiterate that the result of Tuttle & Tonnesen (2020) the BreakBRD galaxies are in a range environment density comparable to the parent sample. We do not take the environment measurements of the MaNGA data set, but it could be possible that our selection of 11 galaxies are in high-density environments. The disk population could then be explained as likely due to an environmental process (i.e., ram-pressure stripping) ceasing star formation in the disk and continuing in the bulge resulting in a younger central bulge. On the other hand, ram pressure can cease star formation and physically alter the disk structure depending on the environment density. As seen in Figure. 2.1 the SDSS colored images, some of the BreakBRD galaxies have prominent spiral structures within the MaNGA field of view, suggesting that ram-pressure stripping is likely not the only process suppressing the star formation consistent with Tuttle & Tonnesen (2020). We cannot disentangle the individual processes, but in future work, we will utilize kinematics to investigate their physical mechanism and influence on similar features.

2.7 Conclusion

We investigate the resolved radial profiles of 11 primarily centrally star-forming galaxies with photometrically red disks, called BreakBRD galaxies. Central star formation is an interesting feature as it deviates from the standard inside-out formation model. Therefore, we analyze stellar age, mass, star formation activity, and chemical abundance to gain insights into possible factors influencing this different evolutionary path. We compare the profiles with 45 central star-forming (CSF), 27 centrally green valley (CGV), and 43 centrally quiescent galaxies (CQC) from the parent sample, which have red bulges and both photometrically red and blue disks, as comparative samples.

These are the key findings we interpret from the data:

- The stellar age distribution of the BreakBRD galaxies increases from the center to larger radii and deviates from the star-forming, green valley, and quiescent galaxies from the parent sample. The central age of the BreakBRD sample is most comparable to the star-forming galaxies, while the disk spaxels are comparable to the green valley galaxies. This result further confirms that the BreakBRD sample is centrally star-forming, with the disk being slightly older. The disk is younger than that of the quiescent population, suggesting potential ongoing star formation activity.

- The BreakBRD sample does not deviate from the stellar mass surface density, aligning with inside-out growth formation. This implies that mass assembly does not play a major role in their central concentration of recent star formation activity.

- The star formation rate and specific star formation rate show decreasing radial profiles for all samples. The BreakBRD sample primarily resides with the star-forming galaxies, displaying a decreasing star formation surface density profile. Each sample shows a decreasing radial profile, but the BreakBRD and CSF galaxies' central regions have higher star formation rates than the CGV and CQC galaxies at all radii. This indicates recent star formation activity and suggests that BreakBRD galaxies produce more stars in the central region than in the disk, similar to mechanisms driving star production in CSF and CGV galaxies.

- The oxygen abundance of the BreakBRD galaxies shows a decreasing radial profile in all three diagnostics, suggesting high to low metallicity from the bulge to the disk. There is a noticeable deviation in the central region for the N2O2 diagnostic, where the inner region is approximately 0.5 dex more metal-rich than the CSF and CGV samples but has similar disk metallicity to CSF, CGV, and CQC samples. The distribution of metallicity is wide and overlaps with the other samples, not showing any strong deviation from the parent sample that could indicate metallicity enhancement or suppression.

In conclusion, we confirm spatially that the BreakBRD galaxies have a younger central region and a noticeably older stellar population in the disk, as indicated by the D_n4000 index and luminosity-weighted age (Age_{LW}), compared to centrally star-forming (CSF), centrally green valley (CGV), and centrally quiescent galaxies from the parent sample. The BreakBRD galaxies do not show a strong deviation in mass distribution, suggesting that mass assembly does not play a major role in the central concentration of young stars. The star formation rate and specific star formation rate show a consistent radial profile in the central region before decreasing at larger radii, providing evidence of continuous star formation comparable to CSF galaxies. This hints that the disk may not be suppressed in star formation but is noticeably less active than the center. This can be caused by neutral gas being forced to center bulge, promoting recent star formation. The oxygen abundance of the BreakBRD galaxies does not show significant deviation from the parent sample that would indicate different mechanisms suppressing or enhancing metal enrichment, and it correlates with the noticeable change in the age distribution of the stellar population.

If not isolated by stellar age, BreakBRD galaxies align with both CSF and CGV galaxies, suggesting they could be affected by similar evolutionary paths that produce a comparable stellar population age, star formation rate, efficiency, and chemical abundance. This analysis would benefit from a larger sample size where we select the youngest central stellar population and compare profiles in that regime. Further analysis using different age indicators would provide more details on the evolution of the stellar population. Finally, investigating the relationship between the ionization parameter and metallicity could help clarify the effects of star formation processes that contribute to chemical abundance.

We note that the small sample size of 11 galaxies limits our ability to make a more concrete conclusion about the differences in the radial profiles. Future studies the Break-BRD spatially resolved kinematics to obtain information about the central regions' internal dynamics compared to the disk. In addition, we will expand our sample size by acquiring spatially resolved IFU data from Low-Resolution Spectrograph 2 from the Hobby-Eberly Telescope (HET) for an in-depth analysis. Finally, we will perform a comparative analysis of the radial profiles of the merger and AGN galaxies excluded from this paper.

Chapter 3

PHAST RGB METALLICITY DISTRIBUTION FUNCTION

Chapter Summary

The Panchromatic Hubble Andromeda Southern Treasury(PHAST) is an extension of the 2012 Panchromatic Hubble Andromeda Treasury (PHAT) (Dalcanton et al., 2012) that built a rich photometry catalog of the stars in the northern half of M31. We use the optical photomtry of the PHAST to select the RGB stellar population and isochrone models to estimate their stellar metallicity. The stars are then binned to 0.01 square bins and we compute the median for metallicity. The median metallicity binned maps sampled in even elliptical bins and compute the median from the inner to outer radii to create the RGB metallicity gradient. Using the stellar photometry of RGB stars in M31, we measure the metallicity gradient in both the northern and southern halves and compare their gradients. The stars comes from the PHAT and PHAST HST surveys optical bands F475W and F814W. Metallicity is calculated from isochrone models using 2D linear interpolation methods, and an RGB selection box is applied to mitigate photometric bias and ensure completeness. Since dust in galaxies affects photometry and can lead to overestimation of metallicity, we use infrared observations to correct for dust effects. While the PHAT catalog includes IR observations, the PHAST catalog only has optical observations, so we use previous IR observations of M31 to measure high dust mass surface density. A previous study of the PHAT metallicity gradient reported a slope of −0.02dex/kpc for the northern half of M31, indicating that the RGB population is well-mixed throughout the disk, assuming a fiducial age of $4Gyr$. In this chapter, we present the metallicity analysis of the PHAST catalog and the comprehensive RGB gradient obtained by combining the PHAT and PHAST catalogs. We find that M31 has a shallow metallicity gradient, with similar slopes ($-0.01dex/kpc$)

for both the northern and southern halves, suggesting that the RGB stellar population is well-mixed throughout the disk.

3.1 Introduction

The stellar metallicity gradient provides information on galaxies' past chemical enrichment, gas accretion, and gas outflow. The metallicity of a galaxy gives insight into the number of generations of stars that have formed and died in a region. As stars die, they release their core metals into the interstellar medium, increasing the metallicity. This increase reflects the age and star formation history of the galaxy. The processes affecting metallicity include the galaxy mass evolution and star formation history, as well as stellar and active galactic nucleus feedback. As such, any attempts to reconstruct a galaxy's evolutionary and interaction history must be able to reproduce the present day metallicity characteristics (Ma et al., 2016; Gehrig et al., 2023). Thus, metallicity provides insight into the chemical evolution, gas inflow and outflow, and star formation mechanisms in nearby galaxies.

Nearby galaxies allow us to study the metallicity gradient of the past when we measure it as a function of stellar age. Spiral galaxies are thought to form their dense central bulge at an earlier epoch and then form the outer disk, called inside-out formation Larson (1976). The metallicity gradient is a consequence of inside-out formation and therefore probes the evolutionary. The stellar age and metallicity can be derived from resolved stars' photometry or using integrated spectra, and thus can be directly compared to models of galactic structure and evolution.

The Panchromatic Hubble Andromeda Treasury (PHAT) survey (Dalcanton et al., 2012) observed millions of stars in the northern half of M31 to obtain photometry measurements, and the metallicity was derived from linear interpolation of isochrone models (Gregersen et al., 2015). The PHAT RGB metallicity gradient was shown to be very shallow with a slope of -0.02dex/kpc, assuming a 4Gyr flat age gradient. There is no clear consensus that nearby galaxies have a flat age gradient. Previous studies demonstrated that nearby galaxies have a wide range of gradients from positive to negative or the absence of a gradient, but both late-type and early-type the studies agree on a negative age gradient Goddard et al. (2017); González Delgado et al. (2014, 2015); Sanchez-Blazquez et al. (2006). These studies also report that in the outer radii ($R > R_{eff}$), the stellar age gradient is negative, supporting inside-out formation. Sanchez (2020) shows that the earlier-type spiral $M_\star > 10^{9.5} M_\odot$ galaxies have a negative luminosity-weighted stellar metallicity gradient with a slope that becomes shallower for low-mass and late-type galaxies. The metallicity profiles can show distinct metallicity substructure due to merger events (Gilbert et al., 2014) and internal structures like stellar bulges, bars, and other dynamical structures.

The RGB stars probe older and more well-mixed disk population and the metallicity provides insight into the generation of the star formation based on the present of metals in the stars atmosphere. Examining RGB stars, Gregersen et al. (2015) measured the metallicity from 4-20 kpc of the northern half of M31 (PHAT) and found a clear decreasing gradient of $[M/H] = -0.020 \pm 0.004$dex/kpc, assuming a constant fiducial age of 4 Gyr from the PHAT survey. In their analysis, they utilized isochrone models (a curve on the Hertzsprung-Russell diagram of stars with the same age but different mass) to extract the optical color and magnitude to interpolate the metallicity. The metallicity is made into a spatially resolved map from the median of binned stars. From their analysis, they found that M31 has a declining radial profile for the gradient using a 4 Gyr fiducial age, and the tail end of the central bar contains a separate population of stars with noticeably different kinematics.

In this analysis we have a similar probe of M31 southern half RGB stars in the disk to both compare and enhance these previous RGB metallicity gradients. The Panchromatic Hubble Andromeda Southern Treasury (PHAST) is an exciting extension of the Panchromatic Hubble Andromeda Treasury (PHAT) program. With the PHAST program, the HST is imaging the southern half of M31 using the same instrumentation as PHAT, adding ~ 96 million stars to the PHAT 117 million stars. The southern half of M31 has features that are unconstrained by the northern history and are therefore of particular interest. The PHAST catalog will also allow to discern the formation history of major dynamical structures such as the interaction with M32 and the Giant Southern Stream (GSS). The southern half of

M31 has a more complex morphology including a star forming region in M31 (NGC 206). In this analysis, we focus on constraining the metallicity of the southern half of the Andromeda galaxy using the red giant branch (RGB) photometry.

In this chapter, I use Gregersen et al. (2015) as the basis of the analysis with the goal to expand on their findings when including the southern half of M31. We assume the following: $RA = 10.65°$ and $Dec = 41.20°$. The distance modulus is $24.45 \pm 0.05, mag$ or $776 \pm 0.18, kpc$, a foreground extinction of $A_v = 0.17$, and effective radius (R_{eff}). See Gregersen et al. (2015) for references therein.

The chapter is structured as follows: In Section 3.2 we describe the photometry catalog and the reduction steps used to isolate the RGB stars. Section 3.3 we discuss align and scale previous dust maps to match the M31 binned spatial maps, how we compute the metallicity from isochrone models and the exclusion of high dust mass surface density to mitigate affects of dust. Section 3.4 we present the metallicity distribution function (MDF) with and with out the high dust mass surface density regions. We show the the spatially binned median maps of the PHAT and PHAST catalogs together and the elliptical apertures we to took to construct the radial profile. Section 3.5 and 3.6 we present and discuss our metallicity gradient and compare the PHAST and PHAT catalog gradients for any noticeable changes. We briefly discuss the presence of the metal rich bar possible.

3.1.1 Previous Studies of M31 Metallicity Gradient

The metallicity gradient of M31 has been studied for more than 3 decades using a range of methods to infer metallicity and age (Dennefeld & Kunth, 1981; Blair et al., 1982; Galarza et al., 1999; Trundle et al., 2002; Sanders et al., 2012). In this section, I summarize previous results of metallicity gradients of M31 spheroid and disk. The stellar halo is the outer surrounding region of the central bulge and the disk where older and metal rich stellar population reside. Gilbert et al. (2014) found that the stellar halo median metallicity decreases by an order of magnitude over 100 kpc and the metallicity profile continuously decreases over the $10-100$kpc range with a peak at $[Fe/H] = -0.4$ for the innermost stars with a median of $[Fe/H] \sim -0.5$. The outermost stars have a median metallicity of $[Fe/H] = -1.4$. Furthermore, they found that there is an increase in the presence of metal-poor stars at larger radii relative to the population. They also state that the removal of suspected debris features does not noticeably decrease the metallicity gradient and possibly shows signs of enhancing the central gradient within $\sim 30kpc$. Sanders et al. (2012) analyzed 100 HII regions and planetary nebula oxygen abundance (metallicity) and found a decreasing gradient of $-0.0195 \pm 0.0055dex$ and a consistent gradient with no significant changes, respectively. The flattening of the oxygen abundance was studied by Magrini et al. (2016), who argued that radial migration can contribute to this feature for M31 from the kinematics. Sanders et al. (2012) also note that M31's interstellar medium (ISM) is highly inhomogeneous, causing the oxygen abundance to vary significantly over relatively small distances between HII regions. Theses oxygen abundance measurement of the gas phase metallicity probe the present day gradient. Peña & Flores-Durán (2019) argues that the PNe abundance for M31 is an extreme case in that the PNe abundance does not relate to the galactocentric distances, which is a consequence of the merging and interactions with other galaxies. Another consequence of the merger and interaction could be the distribution of the chemical enrichment measurement of the oxygen-to-argon ratio from PNe presented by Arnaboldi et al. (2022), where the spatial variation and mixing could be linked to the current rainfall of metal-poor gas from the extraplanar HI region originating from satellites.

3.2 Data

3.2.1 RGB Photometry

The Panchromatic Hubble Andromeda Treasury (PHAT) survey Dalcanton et al. (2012), which was designed to image 1/3 of the M31 star-forming disk using the Hubble Space Telescope (HST). PHAT resolved over 117 million stars with orbits to constrain stellar temperature, bolometric luminosity, and extinction for most spectral types. The program covered a wide range of wavelengths from ultraviolet (UV) to near-infrared (NIR) using the Wide

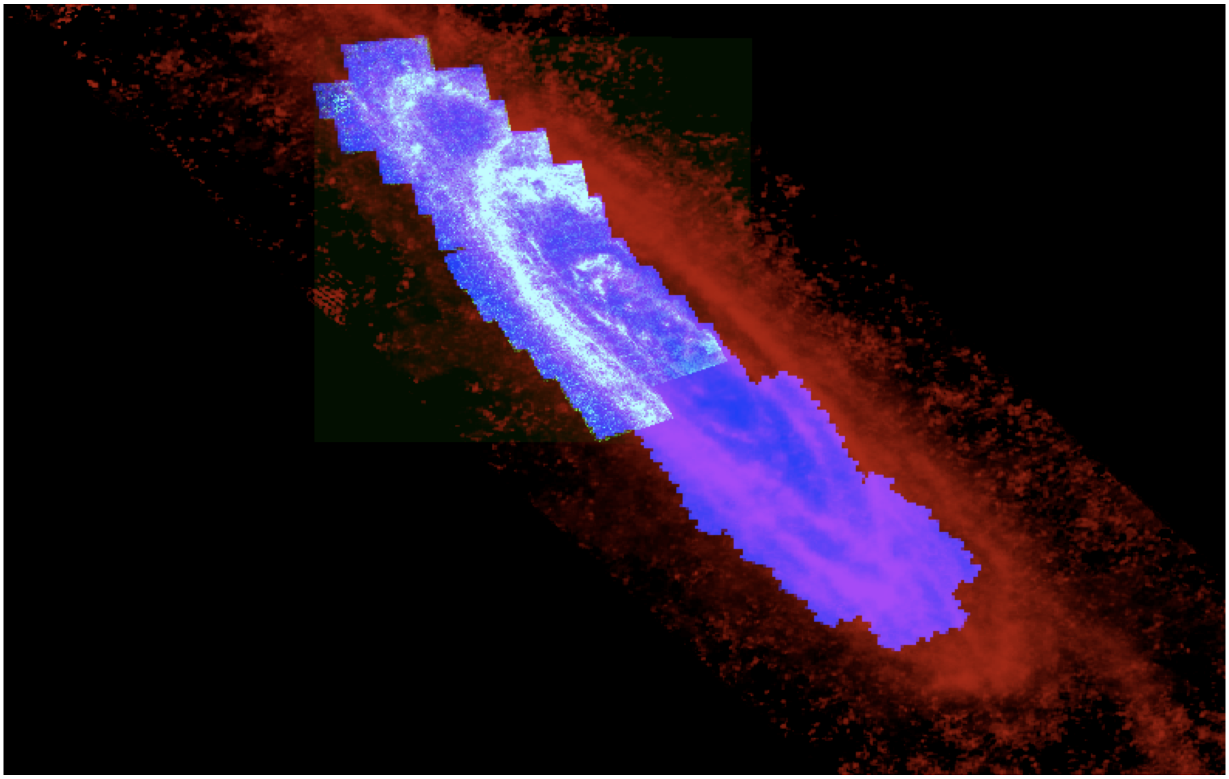

Figure 3.1: DS9 image showing the alignment of the Draine et al. (2013) dust surface mass density map(red), Dalcanton et al. (2015) PHAT dust Av(green) map and the PHAT and PHAST catalog $0.01 deg^2$ spatially binned map (blue)(This work).

Field Camera 3 (WFC3) and the Advanced Camera for Surveys (ACS). The addition of the Panchromatic Hubble Andromeda Southern Treasury Williams et al. (2021) and Chen et al. 2024 would add $> 93 million$ stars to the catalog focusing of the southern half of M31. This would allow for a more in-depth analysis of the metallicity gradient including the full field of view M31. The PHAT and PHAST catalog provide tables of parameters for each star including the positions, magnitudes, magnitudes error, signal-to-noise ratio, crowding and sharpness for each filter (Dalcanton et al., 2012; Williams et al., 2014).

We have adopted a similar method to Gregersen et al. (2015) to measure the metallicity of the red giant branch (RGB) stars and use the same processing of the photometry catalog and isochrone modelling. Gregersen et al. (2015) measured the metallicity gradient of red-giant branch stars with a fiducial age 4Gyr for the Northern part of M31. The RGB stars were corrected the photometric bias and completeness using a selection box in the color-magnitude space. The dust was corrected using the IR stellar photometry provided by the PHAT catalog and the Dalcanton et al. (2015) models. They found a shallow gradient in the median metallicity of $[M/H] = -0.020 \pm 0.004 dex/kpc$. The gradient is less than 1σ sensitivity to systematic effects of dust extinction, photometric bias and completeness, and fiducial age changes. For PHAST catalog we apply a similar data reduction procedure.

The major difference between the PHAT and PHAST catalog is that the PHAST catalog does not have IR observation this requiring a different approach to dust extinction see next Section 3.3.2. Additionally, computing the photometric bias and completeness is out of the scope of this paper and we not the Gregersen et al. (2015) overall finds that both the dust extinction correction and systematic photometric bias does not play significant role in altering the metallicity gradient (comparable to 1σ error). We also note that we use the PHAT six filter photometry catalog over the camera-by-camera photomtry because we do not preform an artificial star test. For the PHAST catalog we use the four filter photometry catalog. In this analysis, we only focus on the optical bands $F475W$ and $F814W$.

We create an optical catalog including only the $F475W$ and $F814W$. These catalogs have uniform coverage from the individual ACS/WFC field (see. Williams et al. (2014, 2023) for further description). We apply the following quality cut call defined as the good star (gst) cut to both the PHAT and PHAST catalog:

- $F475WSNR$ and $F814WSNR \geq 4$
- $F475Wcrowd$ and $F814Wcrowd \leq 2.25$
- $F475Wsharp^2$ and $F814Wsharp \leq 0.2$

The optical photometry is corrected for foreground extinction using $A_V = 0.17mag$. We apply A_λ/A_V of 1.212 and 0.596 for $F475W$ and $F814W$ extinction respectively (from http://stev.oapd.inaf.it/cgi-bin/cmd). The corrected photometry is represented as $F814W_0$. We then exclude all stars with $F814W_0 < 23mag$ to remove stars with higher photometric bias and lower completeness. These criteria are the same as those found in Gregersen et al. (2015),the original analysis of the PHAT catalog RGB metallicity distribution function (MDF) and radial gradient. After the reduction, The PHAST catalog has $\sim 3.7 \times 10^6$ stars and PHAT catalog has $\sim 6 \times 10^6$. In an effort to mitigate completeness and bias, we approximate the Gregersen et al. (2015) selection box on the color magnitude diagram of the photometry catalog. After applying the selection box, the PHAST catalog $\sim 6 \times 10^6$ stars and the PHAT catalog contains $\sim 7 \times 10^6$ stars. In total we have 11×10^6 we have photometric measurements and position for M31.

3.2.2 Dust Mass Surface Density Maps

Unlike the PHAT, the PHAST catalog does not have IR imaging from the Hubble Space Telescope and thus we have to find an alternative route to correct for extinction. Dust extinction causes an over-estimate in stellar metallicity without accounting for the surrounding dust blocking the light from the RGB stars. We mitigate the effect of dust by using dust maps from previous surveys that used IR imaging to measure the dust mass and luminosity as well there corresponding uncertainty. Draine et al. (2013) produced a

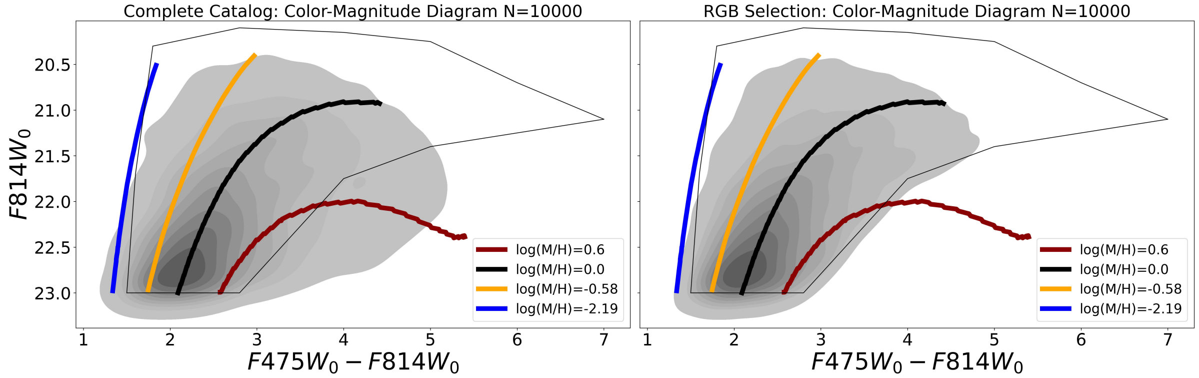

Figure 3.2: A sub-sample of PHAST catalog color magnitude diagram (CMD) (grey). (Left) The original catalog, (Right) The original catalog after the applying approximate Gregersen et al. (2015) RGB selection box. The red, orange, black and blue represent the $[M/H] = [-2.19, -0.58, 0.0, 0.6]$ isochrone models with a fiducial age at $4Gyr$ respectively where $Z_{\odot} =$ 0.0152([M/H]=0.0).

high resolution maps of dust structure for M31 using Spitzer and Hershel catalog based on analysis from Draine & Li (2007) dust calibration models. The maps are the best fits values from the 2 angular resolution scales from the SPIRE350(S350) and MIPS160(M160) camera. The M160 and S350 have a FWHM=24. 9 = 90 pc at 744 kpc and FWHM = 39 = 141 pc at 744 kpc respectively. The best fits maps are available for public use, see http://www.astro.princeton.edu/draine/m31dust. Dalcanton et al. (2015) compare the dust maps with the PHAT IR data and found that the alignment was in agreement with the dust structure from the IR photometry map. Their analysis provide resolved maps that align with the dust structure of M31 from the PHAT catalog.

3.3 Method

3.3.1 Resolved Spatial Maps

In Figure 3.1 we present the 3 aligned maps of M31 observation. We show the S350 dust mass surface density (red) Draine et al. (2013), PHAT catalog A_V map(green) derived from IR photomtry and this work 0.01° square bins spatially resolved map produced from the

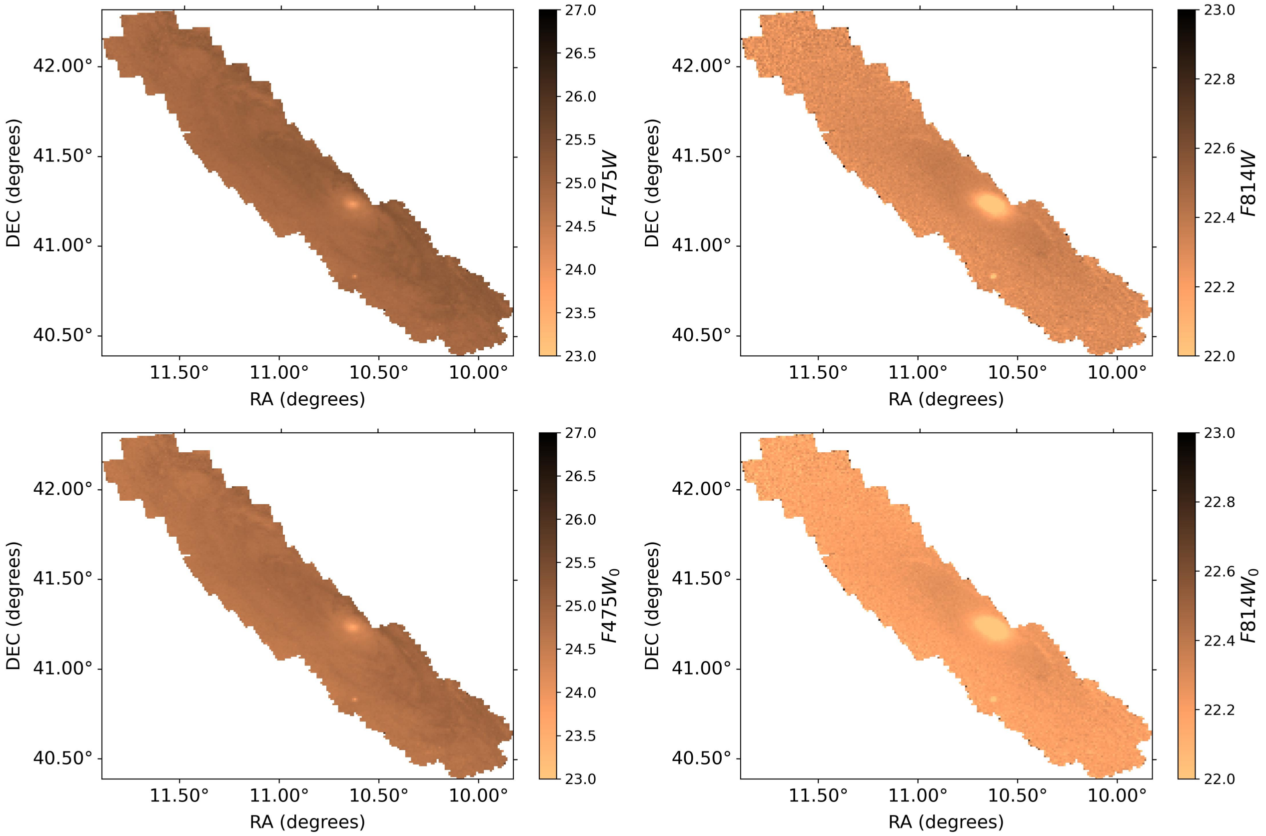

Figure 3.3: The spatial map of the PHAT and PHAST catalog where the color for F814W(left column) F475W(right column) shows the comparison between the original magnitude spatially binned map(Top) to that of the foreground corrected binned map(Bottom) showing no significant changes.

PHAT and PHAST catalog using Astropy Python package. We demonstrate that we are able to align our catalog with previous studies and the dust map. The binned maps are used to construct the radial profiles for both catalogs as well as the combined profiles to represent the M31 metallicity profile. The S350 dust map is used to locate high dust mass regions across M31 disk.

We make 2D spatial maps of the various parameters of the photometry catalog. We bin the coordinates to 0.01° square bins and take the median of the stars within the given bins. In Figure 3.3 we show the spatial maps for the PHAT and PHAST catalog of the F814W and F475W mag original maps and the foreground corrected maps. The PHAT and PHAST catalog fit seamlessly. The

3.3.2 Source of Dust Extinction

3.3.3 Estimating RGB Metallicity from Isochrone Models

We use the stellar evolutionary tracks (i.e. isochrones) models to infer the metallicity of the each star given the F814W magnitude and F475W-F814W color to interpolate metallicity values for each star in the catalog. Bressan et al. (2012); Chen et al. (2014); Tang et al. (2014) provide stellar evolution tracks (See. http://stev.oapd.inaf.it/cgi-bin/cmd) when providing inputs. The model provides a table of parameters such as the magnitude in all filters, initial mass, and luminiosity. These parameters are the sampled at $\Delta Z = 0.0001$ for range of $0.6 >= Z >= 0.001$ where solar metallicity is $Z_{\odot} = 0.0152$ at a fiducial stellar age of 4Gyr. As done in Gregersen et al. (2015), we use the Python packages scipy and LinearNDInterpolator function to linearly interpolate the metallicity from the optical color magnitude diagram. The final isochrone table is then reduced to remove non-RGB stars. We first exclude magnitudes greater than 23 mags in F814W filter to match the photomtry catalog. In Figure 3.2 we show the color-magnitude diagram of the PHAST before and after applying the RGB selection box to mitigate photometric bias and completeness. Additionally, we over plot the 4 RGB isochrone models for $[M/H] = [-2.19, -0.58, 0.0, 0.6]$.

3.3.4 Remove High Dust Mass Regions

The photomtry catalogs are spatially binned in $0.01deg^2$ and then we take the median of all the stars in those binned areas for every measurement (i.e. F475W, F814W, M/H, dust surface mass etc.). All the world coordinate systems are aligned. We remove the high dust mass surface density $M_{\odot}kpc^{-2} > 3e5$ and remove them before constructing the radial profiles The high dist mass regions are predominately in the dust ring substructure. In Figure 3.4 we present our spatial maps, the metallicity, dust mass surface density, stellar number density and the photometric color ($F475W_0 - F814W_0$). The ring structure for all maps coincide with the high mass dust structure. We show in Figure 3.10 the maps when excluding dust mass surface density($\Sigma_{M_{\star},dust} \geq 3e5M_{\odot}kpc^{-2}$). This criteria removes the dust ring structure leaving a physical gap in the binned maps. We construct radial profiles from the center to disk and apply a linear fit measure the metallicity gradient as we discuss in the next section.

3.4 Analysis

The aim of this section is to demonstrate the techniques used to evaluate the metallicity maps derived from the catalog to provide the metallicity gradient with and without the high dust mass surface density. As discussed in the last section, the RGB we are using are produced after the GST stars are selected, the Gregersen et al. (2015) RGB selection box is applied to the color magnitude diagram, selecting RGB stars with apparent magnitude ≤ 23.0. The stellar metallicity is then estimated and we create binned spatial maps and align Draine et al. (2013) dust maps. We present the MDF for the PHAT and PHAST catalog and visualizations of removing high dust mass surface density using the dust maps. The maps are then used to examine the radial profile of the PHAT and PHAST catalog as well as the entire M31 profile by combining the catalogs.

In Figure 3.6, we show the metallicity distribution function (MDF) for the complete catalog, the PHAT, and the PHAST catalogs. We show that the metallicity distributions for PHAT and PHAST are qualitatively similar. Additionally, our PHAT MDF median

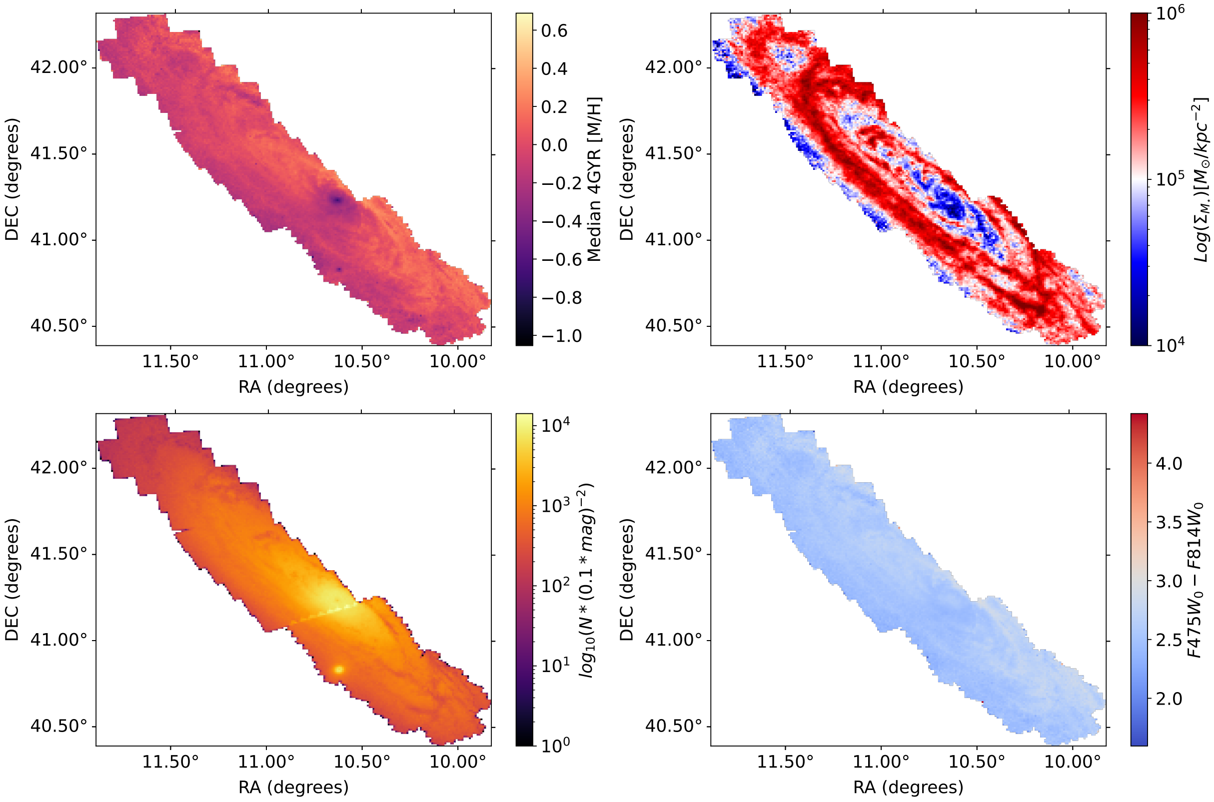

Figure 3.4: (From Left to Right and top to bottom) The 0.01° spatially binned maps, The median $4Gyr$ metallicity [M/H], The dust mass surface density, stellar density, the median foreground corrected color.

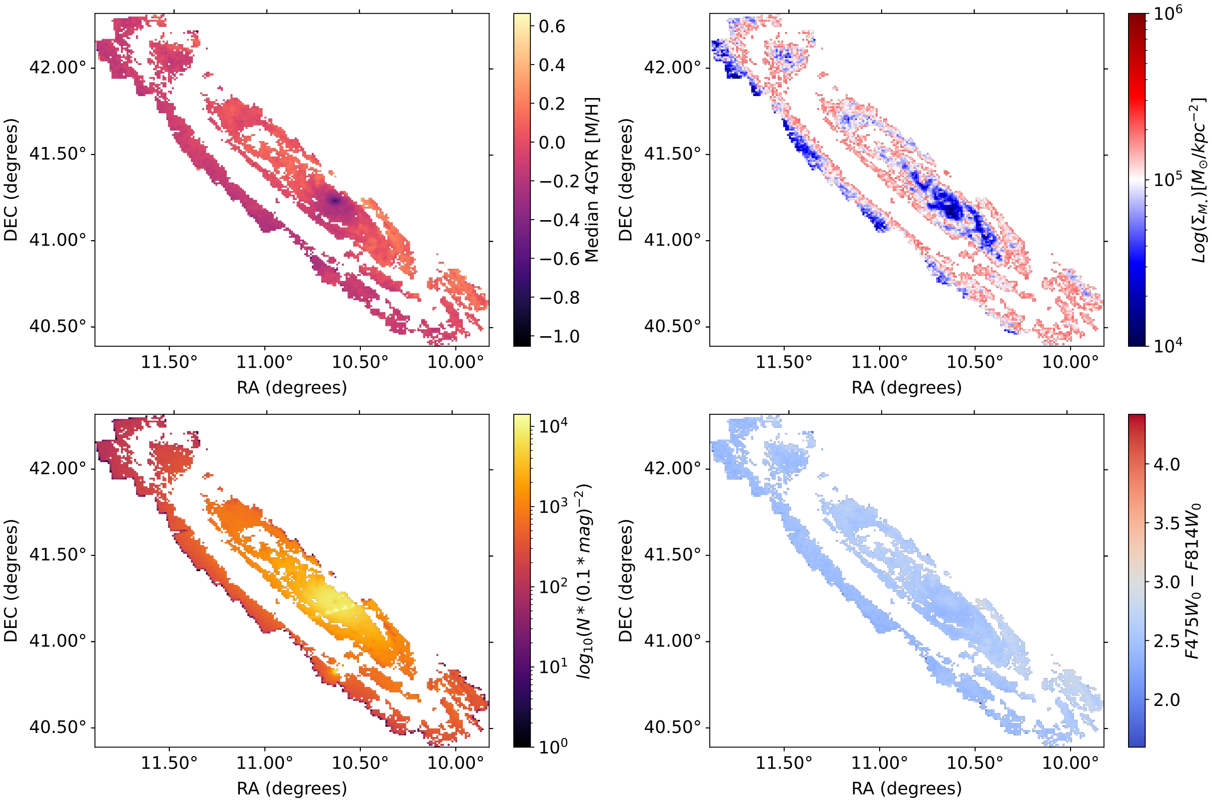

Figure 3.5: (From Left to Right and top to bottom) The 0.01° spatially binned maps excluding the dust mass surface density $Log(\Sigma_{M_*}) > 3e5M_\odot kpc^{-2}$, The median $4Gyr$ metallicity [M/H], The dust mass surface density, stellar density, the median foreground corrected color.

metallicity is slightly more metal-rich than that of Gregersen et al. (2015), with less than a 0.1 dex difference.

We remove the binned areas with a dust mass $\geq 3 \times 10^5 M_{\odot}/kpc^2$ to show the metallicity spatial map with and without dust regions in Figure 3.7. The maps in the top row display the regions with and without high dust mass, corresponding to the spiral structure of M31. The bottom row shows the metallicity distribution function (MDF) of the spatial bins (not individual stars). The left panel presents the complete dataset, while the right panel separates the MDF by high dust mass and the remaining dust mass surface density from the Draine et al. (2013) M31 dust map. The MDF of the high dust mass regions matches the remaining sample MDF, indicating that dust does not significantly impact the metallicity gradient.

We construct the metallicity profile by taking elliptical annulus bins across the PHAT and PHAST catalogs from the center of the galaxy with a $b/a = 0.275$ (Gregersen et al., 2015). In each bin, we take the median of the spatial binned values in the radius range. Additionally, we use the Python SciPy statistics package to compute the confidence interval values in the ellipse to determine the true parameters of the population from a sample. Figure 3.7 shows the elliptical annuli used to measure the median metallicity gradient for the RGB stars at a fiducial age of 4 Gyr. We apply the elliptical annuli to the maps excluding high dust mass regions, which appear visually similar.

3.5 Results

In this section, we analyze the radial gradient of the PHAT, PHAST and the complete catalog and compare the difference to the previous analysis from Gregersen et al. (2015). Our results come from the spatial maps with high dust surface mass included (Figure 3.4) and excluded (Figure 3.5) in the sample to compare the impact of dust.

We present the M31 RGB metallicity gradient from the center to the outer disk (Figure 3.9). We binned the median metallicity into evenly separated elliptical apertures along the semi-major axis as shown in Figure 3.8 of the visualization of the elliptical apertures. We exclude the dust mass surface density ($Log(\Sigma_{M_\star,dust})[M_{\odot}kpc^{-2}] > 3e5$) to compare changes

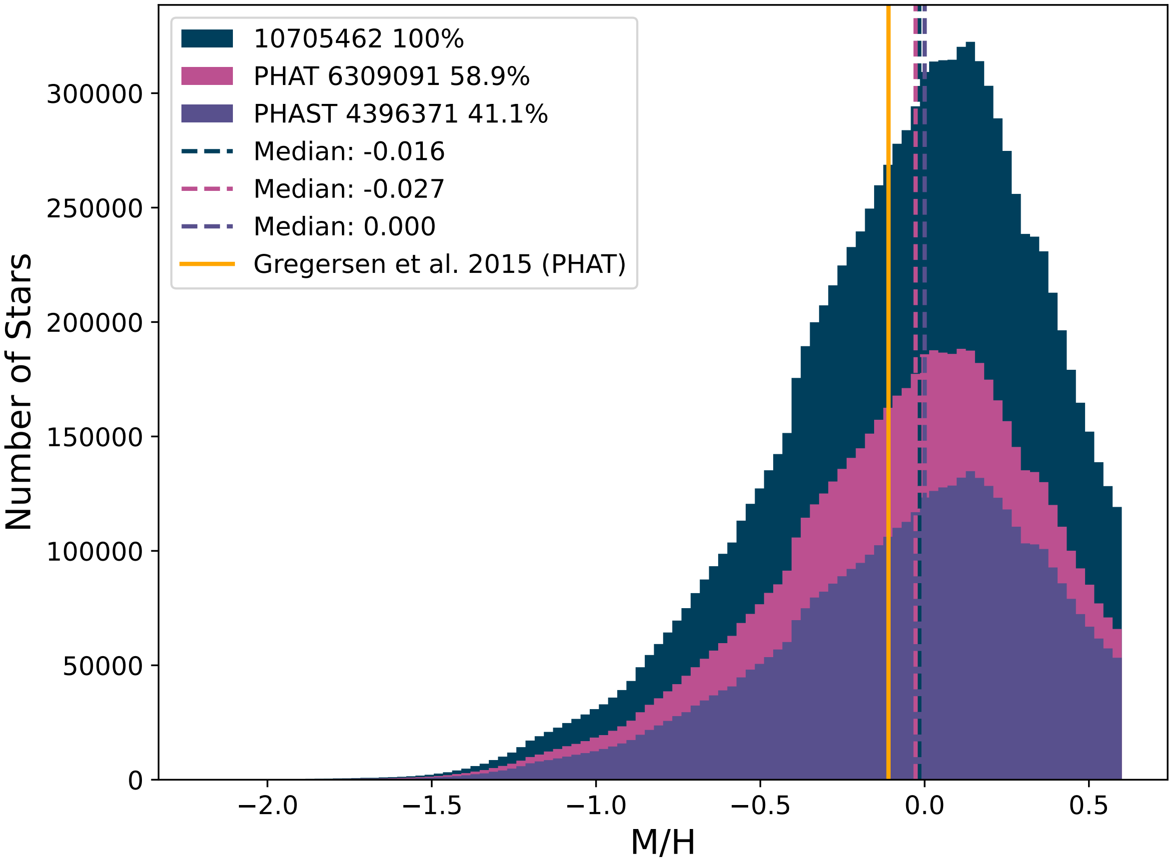

Figure 3.6: M31 RGB metallicity distribution function using a flat fiducial age of 4Gyr. The blue, pink and purple histogram represent the complete M31 catalog(PHAT and PHAST), PHAT and PHAST respectively, The dash lines are the median metallicity and the values are displayed in the legend. We also include the the median metallicity of the PHAT catalog from Gregersen et al. (2015) ($\sim -0.11 dex$) in orange. These MDFs are not corrected for systemic bias in metallicity but as discussed in Gregersen et al. (2015), the MDF is qualitatively the same

.

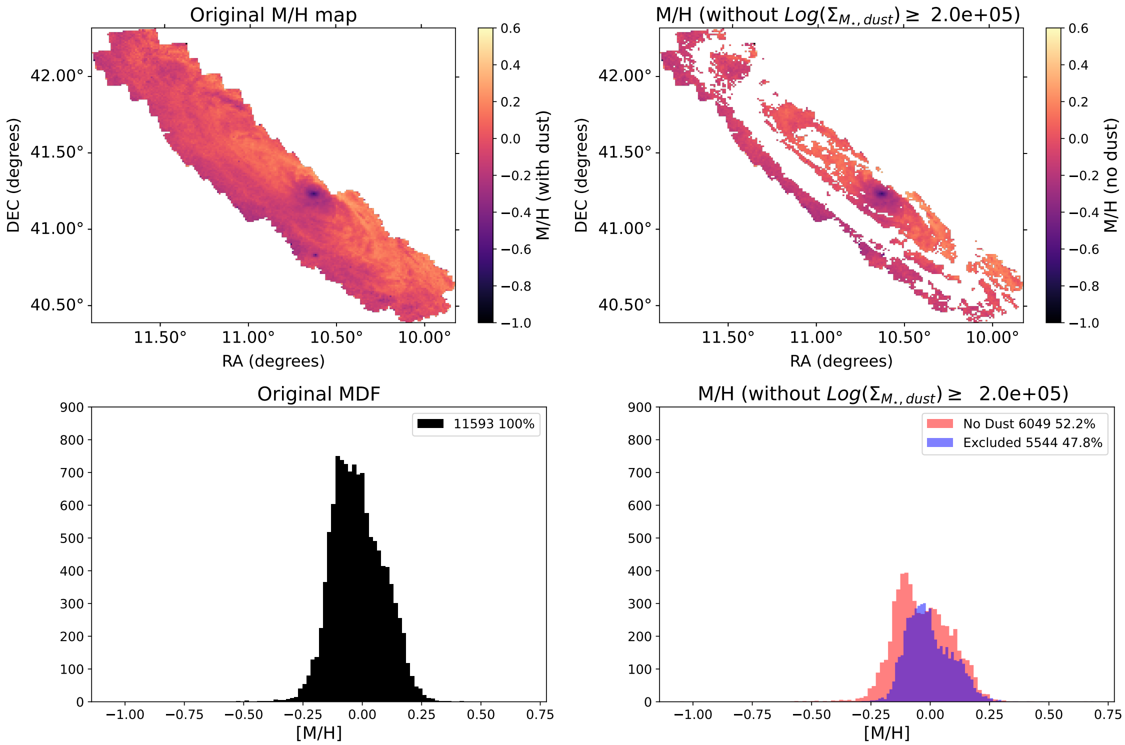

Figure 3.7: M31 spatially binned maps with and without dust mass surface density $\geq 3 \times 10^5 M_\odot/kpc^2$ in the top panels and the metallicity distribution function of the spatial bins comparing the original and the separated values.

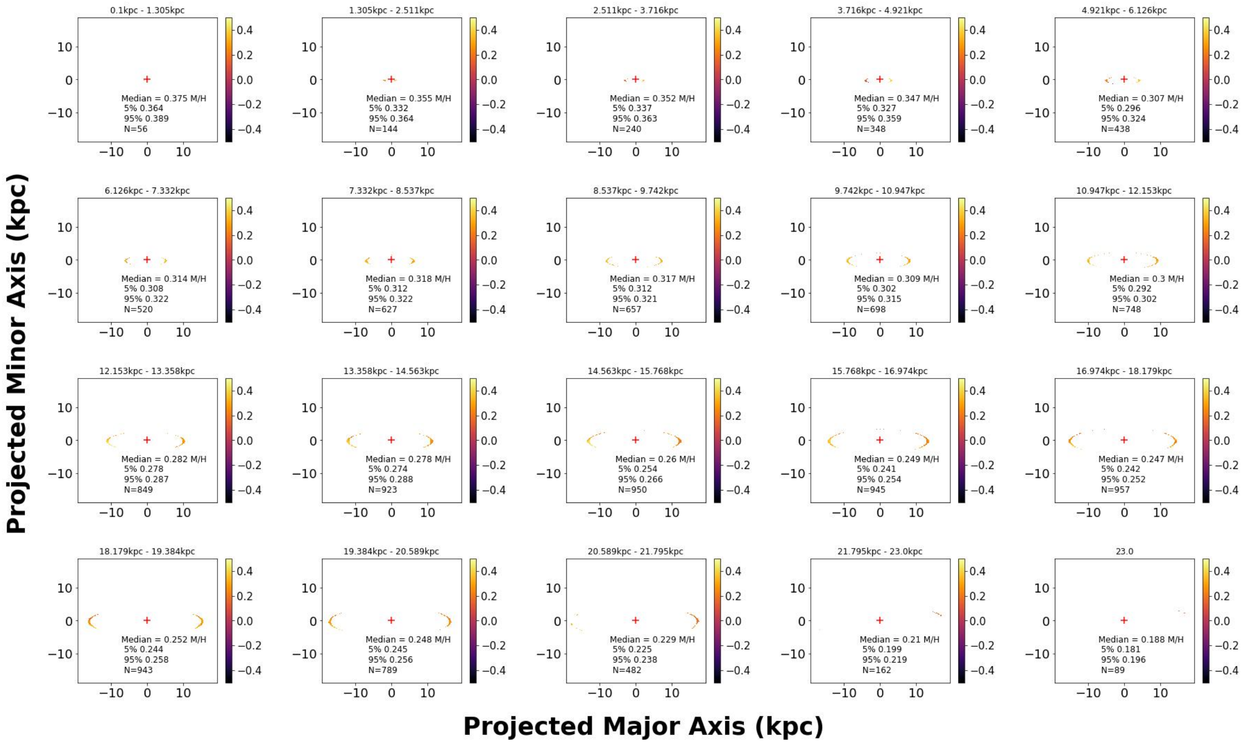

Figure 3.8: Projected RGB metallicity map elliptical annulus bins with the dust region. The color represent the metallicity. The cross represent the center x and y coordinates for the M31 map. The bottom right legend shows the median, 95 and 5 percentile and the number of spatial bins in the annulus.

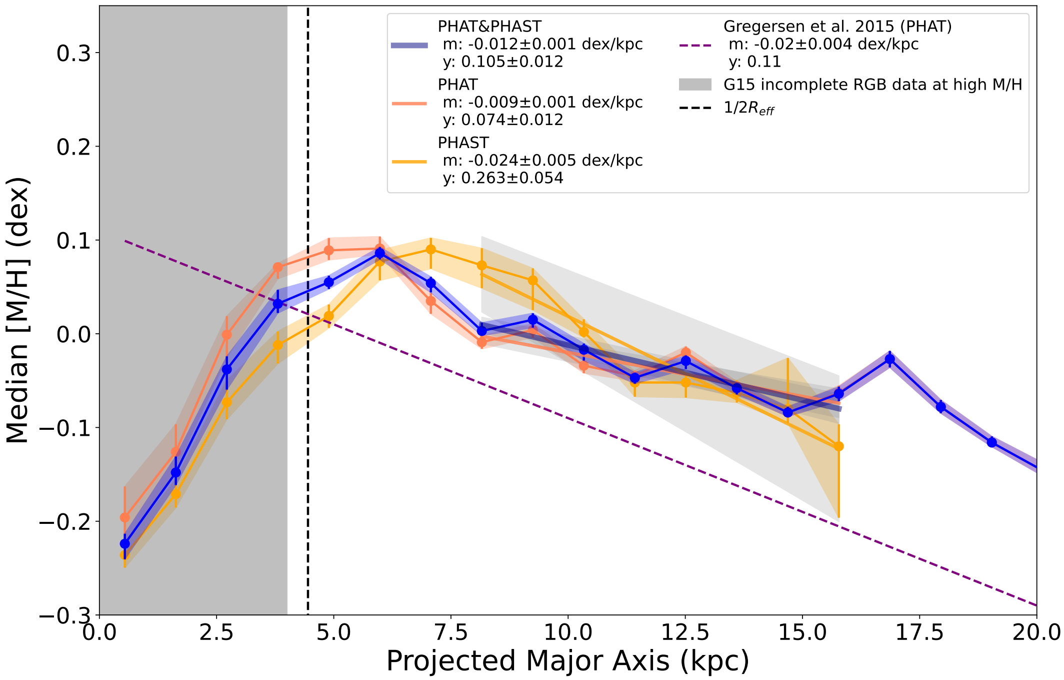

Figure 3.9: The median RGB metallicity gradient for the PHAT and PHAST catalogs. The orange and yellow colors represent the PHAT and PHAST metallicity radial profile. The blue line represent the median metallicity of the combined catalogs and the solid black line. The solid black lines represent the line of best fit for the different maps. The median metallicity shows to have a very shallow gradient with a slope $0.01 dex/kpc$ in comparison to $0.02 dex/kpc$ Gregersen et al. (2015) gradient represented by the dashed purple line. Overall our result is in agreement with the RGB metallicity distribution is constant through out the disk. The grey represent the incomplete bulge region from Gregersen et al. (2015) to show where less reliable measurements are in the the gradient. The vertical dash line represents the half light radius R_{eff} (Courteau et al., 2011)

in the gradient to that off the complete map that includes those dust regions. We then create the metallicity radial profile shown in Figure 3.9 with dust regions included and without the dust region 3.10.

We fit a gradient to the measured metallicity profile at radius greater than the R ¿ 4.45 kpc ($1/2R_{eff}$ (Courteau et al., 2011)). As discussed in Gregersen et al. (2015) this radial cut excludes low completeness in the central bulge. We then create a linear fit based on these medians.

We measure M31 metallicity gradient to be -0.01 ± 0.001dex/kpc for both the dust excluded and included with a less than $0.005dex$ change in the y-intercept(See. Figure 3.9 and Figure 3.10). We use bootstrapping to compute the confidence interval for each bin as shown in the error bars. The exclusion of high dust mass does not impact the metallicity gradient of M31 and is in agreement with the Gregersen et al. (2015) in terms of affect. However our metallicity gradient is 0.01 dex/kpc shallower that theirs even when isolating the PHAT data and measuring the gradient.

The PHAT and PHAST gradients in our analysis are very similar in that they have similar slopes of $0.01dex/kpc$ in with and with high dust surface mass density regions. Gregersen et al. (2015) noted that the region $\sim 3 - 7kpc$ is the metal rich bulge where the highest metallicity regions can be found for the PHAT catalog. We also find this in our analysis of our metallicity profiles for PHAT. For PHAST, however we find that the highest metallicity regions at $\sim 8{-}12kpc$. The peak in metallicity appears to be the same at $0.1M/H$. In further agreement, we demonstrate that the PHAT catalog peak does not change when excluding the dust which aligns with Gregersen et al. (2015) where the high metallicity is not caused by dust by a real change in stellar population. In comparison, the PHAST catalog shows that the peak is virtually unchanged when excluding the high mass dust regions. Interestingly at $\sim 11 - 14kpc$ the metallicity slightly increase when dust excluded resulting in an additional peak in the metallicity profile. The cause of this change will further investigated in future work but it is insignificant change in the scheme of the overall metallicity profile.

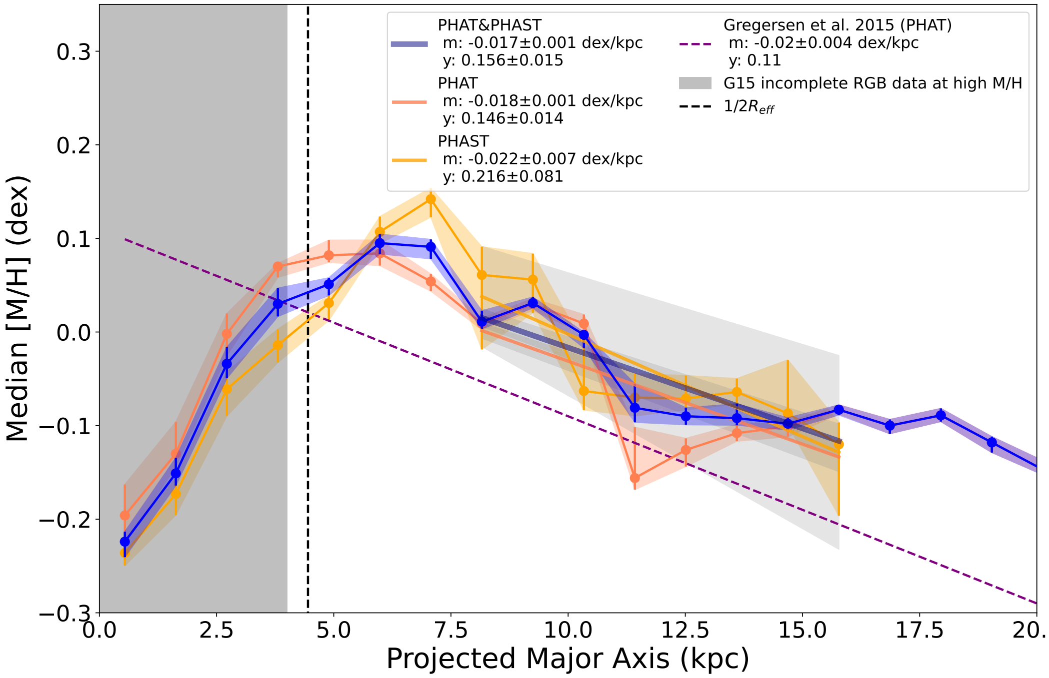

Figure 3.10: The median RGB metallicity gradient excluding high dust mass surface density regions $Log(\Sigma_{M_\star,dust})[M_\odot kpc^{-2}] > 3e5$ for the PHAT and PHAST catalogs. The orange and yellow colors represent the PHAT and PHAST metallicity radial profile. The blue line represent the median metallicity of the combined catalogs and the solid black line. The solid black lines represent the line of best fit for the different maps. The median metallicity shows to have a very shallow gradient with a slope $0.01 dex/kpc$ in comparison to $0.02 dex/kpc$ Gregersen et al. (2015) gradient represented by the dashed purple line. Overall our result is in agreement with the RGB metallicity distribution is constant through out the disk. The grey represent the incomplete bulge region from Gregersen et al. (2015) to show where less reliable measurements are in the the gradient. The vertical dash line represents the half light radius R_{eff} (Courteau et al., 2011)

3.6 Conclusion

We investigate the M31 RGB stars of metallicity gradient using highly resolved spatial maps and constructing radial profiles. Our work is heavily influenced by previous research by Gregersen et al. (2015) where they studied the PHAT catalog metallicity gradient. This analysis uses the stellar photometry individual stars from the HST PHAT and PHAST survey and covers $\sim 25kpc$ of M31 disk. Metallicities are estimated from $\sim 11.0e6$ RGB stars using the optical photometry and isochrone models. We create a spatially resolved map of the median metallicity and apply the RGB selection box from Gregersen et al. (2015) to correct for photometric bias and completeness. We then construct radial profiles using this map to compute the metallicity gradient. From the maps and radial profiles we conclude the following:

- **RGB Gradient:** M31 4 Gyr RGB stars have a metallicity gradient with a slope of -0.012 ± 0.001dex/kpc. Our RGB metallicity gradient excluding the high dust mass surface density shares a similar slope to the Gregersen et al. (2015) for the PHAT catalog and are 0.1 dex higher in metallicity. The PHAST catalog show a steeper metallicity gradient but within the error of the PHAT catalog. The metallicity gradient is impacted by the exclusion of high dust mass surface density.

- **Compare PHAT and PHAST RGB Gradient:** The PHAST catalog shows a noticeable increase in metallicity from $5 - 7.5$kpc before gradually decreasing throughout the southern half of the disk. We present the 4Gyr metallicity gradient from $\sim 8.0 - 16$kpc, the slope is -0.025 ± 0.005dex/kpc.

  We apply the exact same processing and data reduction of the PHAST catalog to the PHAT catalog and estimate the metallicity gradient. PHAT has a metallicity gradient slope of -0.009 ± 0.001 dex/kpc from $\sim 8.0 - 16$kpc. Our metallicity gradient is shallower than the previous study and could relate to the recent improvements to

PHAT catalog highlighted in Williams et al. (2023) but it is currently unclear and future analysis will aim to explore the impact of the change in the catalog.

PHAT and PHAST catalog are both have shallow metallicity gradient but the PHAST gradient is more than twice as steep as the northern half. The southern half has a slightly higher RGB metallicity than that of the northern half from $7.5 - 11.5$kpc and then the metallicity are about the same to the outermost radii. The radial profiles and gradient do not significantly deviate. We interpret this result as the RGB stars are well mixed and distributed across the disk of M31.

- **Impact of High Dust Mass** The metallicity gradient is slightly impacted by the exclusion of high dust mass surface density. We align and the IR dust maps of M31 to our maps of M31 and remove high dust mass surface density $\Sigma_{M_\odot kpc^{-2}} \geq 3.0 \times 10^5$ and then plot the radial profiles for both the PHAT and PHAST catalog. We find that the PHAT and PHAST have slopes of -0.015 ± 0.001dex/kpc and -0.023 ± 0.005 dex/kpc respectively from $\sim 8.0 - 16$ kpc. Overall, the exclusion of high dust mass surface density does not significantly affect the metallicity gradient. Interestingly, at $\sim 6 - 9kpc$ the metallicity slightly increase when dust excluded resulting in an more pronounced peak in the metallicity profile. Further analysis is needed to determine the significance of this change if any.

- **Metal Rich Bar Feature** M31 bar is approximately between $3 - 7$ kpc (Gregersen et al., 2015). In the M31 radial profile there is a clear the peak in RGB metallicity at ~ 6 kpc before decreasing in the outer disk. The PHAST catalog shows to continue at the peak metallicity to about 8 kpc and the PHAT catalog show to have a similar metallicity at 5 kpc. Our change in metallicity for both the PHAT and PHAST catalog show noticeable changes where the metal rich bar approximately resides. Further, the region is unaffected by the removal of high dust mass surface density in agreement with Gregersen et al. (2015) that this is signs of a real change in stellar population. Future studies will measure do a more detailed study of the stellar population of the central bar.

Chapter 4

PIPELINE DEVELOPMENT AND MACHINE LEARNING APPLICATION FOR RESOLVED NEARBY GALAXIES

Chapter Summary

Survey and observation of nearby galaxies data in various forms needs software tools to gain research insight. Machine learning applications can provide some of these tools, necessary for analyzing the large data sets associated with nearby galaxies. In Chapters 2 and 3 I demonstrate how we can use both integral field unit spectroscopy and stellar photometry to examine the distribution of properties to investigate recent evolution. In this chapter, we show the software tools in development to process stellar photometry for flagship observatories and a state-of-the-art segmentation classification model to predict the ionization sources for integral field unit spectroscopy survey called MaNGA. The hyperspectral classification model Spectral–Spatial Feature Tokenization Transformer (SSFTT) uses a combine convolutional neural network and transformer architecture to predict the label map of land cover and land use hyperspectral datasets. We attempt to use the high quality MaNGA dataset and the SSFTT to predict the ionization source distribution for multiple datacubes. In the subsections below, I first discuss the the pipeline development, and then Deep Learning algorithm that I have contributed to for future analysis of large spectroscopic and photometric datasets.

This chapter addresses two specific problems:

- Providing a new Python-based pipeline for managing photometry measurements in future surveys of nearby galaxies

- Testing a complex machine learning model to classify the dominant ionization sources

in star-forming galaxies and evaluating its accuracy in recovering true values

This problem is significant within the scope of the thesis because, as demonstrated in Chapters 2 and 4, understanding the stellar population and star formation activity in nearby galaxies relies on accurate IFU and stellar photometry data. Testing the predictive capability of advanced models offers a valuable test case for future surveys that will utilize similar models with even larger datasets.

4.1 Photometry Pipeline

4.1.1 Background

In the field of astronomy, flagship mission provide massive amounts of data of our Universe and requires software to mange and calibrate data to produce science ready data products. The Panchromatic Hubble Andromeda Southern Treasury (PHAST) is an exciting extension of the Panchromatic Hubble Andromeda Treasury (PHAT) program (Dalcanton et al., 2012). The PHAST program, the HST is imaging the southern half of M31 using the same instrumentation as PHAT, adding 100 million stars to the coverage area. The southern half of M31 has features that are unconstrained by the northern history and are therefore of particular interest. The PHAT and PHAST datasets are large and require a dedicated data pipeline to extract photometry measurements.

We present a refactoring of the original Panchromatic Hubble Andromeda Treasury photomtry pipeline from Perl/IDL based code to Python. The PHAT pipeline, which was created in 2007, uses an Amazon Web Services (AWS) pipeline that is still in use today Williams et al. (2018). The pipeline is given HST provided calibrated images and produces clean mosaic images in all bands, color images, catalog of resolved stellar photometry, and artificial star tests. Additionally, the authors also provide many diagnostic and scientific plots from each step in the pipeline process. However, this pipeline needed to be refactored to be all python-based and use the most updated pre-processing routines and make it more user-friendly for future analysis and development. To address this need, Python scripts are being developed for the new PHAST data pipeline to produce the photometry catalog. The pipeline will produce the photometry data-products as the previous pipeline but with updated data preparation and can be easily modified for future users because it is all written in one of the most widely used programming language. An example of the new feature called DeepCR, which uses a trained convolutional neural network to remove cosmic rays from images, is included in the pipeline Zhang & Bloom (2020); Chen et al. (2024). The new software will enable users to produce their own photometry catalog from their WFC3 UVIS calibrated data without the cost of AWS to pay for resources and development. The pipeline will also be able to produce photometry catalogs for the flagship JWST NIRCAM calibrated data.

The main objectives of this chapter are to develop a photometry pipeline using the wpipe package, demonstrating how users can customize it for their needs. Achieving these objectives will provide valuable software for processing photometry data in future surveys, such as the Roman Space Telescope mission. With the PHAST program, the HST is imaging the southern half of M31 using the same instrumentation as PHAT, adding 100 million stars to the coverage area.

The PHAT and PHAST datasets are large and require a dedicated data pipeline to extract photometry measurements. The PHAT pipeline, which was created in 2007, uses an Amazon Web Services (AWS) pipeline that is still in use today (Williams et al., 2018). The pipeline is given HST provided calibrated images and produces clean mosaic images in all bands, color images, catalog of resolved stellar photometry, and artificial star tests. Additionally, the authors also provide many diagnostic and scientific plots from each step in the pipeline process. Future flagship surveys from JWST (Gardner et al., 2006) and Nancy Roman Space Telescope Akeson et al. (2019) will have a significantly larger FOV and thus increase the number of stars observed in a given observation and will require a robust and automated pipeline to manage the large dataset and this work aims to provide such software.

To address this need, Python scripts are being developed for the new PHAST data pipeline to produce the photometry catalog. The pipeline will produce the photometry data products as the previous pipeline but with updated data preparation and can be easily modified for future users because it is all written in one programming language. An example of the new feature called DeepCR, which uses a trained convolutional neural network to remove cosmic rays from images, is included in the pipeline (Zhang & Bloom, 2020). The new software will enable users to produce their own photometry catalog from their WFC3 UVIS calibrated data without the cost of AWS to pay for resources and development. The pipeline will also be able to produce photometry catalogs for the flagship JWST NIRCAM calibrated data.

4.1.2 Data

Input Data

The Panchromatic Hubble Andromeda Southern Treasury (PHAST) is an exciting extension of the Panchromatic Hubble Andromeda Treasury (PHAT) program (Dalcanton et al., 2012), which was designed to image 1/3 of the M31 star-forming disk using the Hubble Space Telescope (HST). PHAT resolved millions of stars with orbits to constrain stellar temperature, bolometric luminosity, and extinction for most spectral types. The program covered a wide range of wavelengths from ultraviolet (UV) to near-infrared (NIR) using the Wide Field Camera 3 (WFC3) and the Advanced Camera for Surveys (ACS). The PHAST program, the HST is imaging the southern half of M31 using the same instrumentation as PHAT, adding 100 million stars to the coverage area. The southern half of M31 has features that are unconstrained by the northern history and are therefore of particular interest.

The photometry pipeline uses Flexible Image Transport System($FITS$) as the input file format. These fits file are the primary output format structure from the HST ACS and WFC pipeline provided by the Space Telescope Science Institute. The calibration pipeline preforms various correction to mitigate the instrumentation affect on the imaging. The calibration and instrument details can be found in the header including the filter used, position and world coordinate systems. Additionally the FITS file has 6 extensions with their own header description and the calibrated image in each chip with correspond data quality arrays and inverse variance map. The calibration pipeline produces an $FLT.fits$ and $FLC.fits$ representing if a CTE correction was applied (FLC) or not(FLT) for HST dataproducts. For JWST, the image files are $CRF.fits$. We use $FLC.fits$ for our examples.

4.1.3 Methods - schedule jobs and build task(how wpipe works)

Wpipe Pipeline Package

The photmetry pipelines uses the *wpipe* package('https://github.com/benw1/WINGS') developed Dr. Adrien Thob (Thob et al. in prep). A full description of wpipe can be found in the cookbook but give a brief description here. The Wpipe module is developed for pipelines that need to automate scheduling of successive task. The pipeline organize task to preform on each image at the same time keeps track task and image being processed allowing for pausing and resuming the pipeline using terminal sub-command.

Wpipe uses a shared SQL database for jobbing handling the data and uses a suite of classes(Pipeline, User, Mask, Job etc.) to represent necessary entities of the pipeline in the database. The primary function of jobbing is to fire jobs when called to start a new job. The chaining of various jobs is running the pipeline. The firing task is executed by command-line argument recognized by wpipe. In Figure 4.1 we show the simplified Unified Modeling Language class diagram representing wpipe class architecture. The SQL Database is powered by third-party module SQLAlchemy and is implemented via wpipe's subpackage *sqlintf* that the user should never have to interface with.

The initializing of the pipeline makes the data directory structure at a given home directory and the directories will be used to store data products, configuration files and build task from the pipeline.

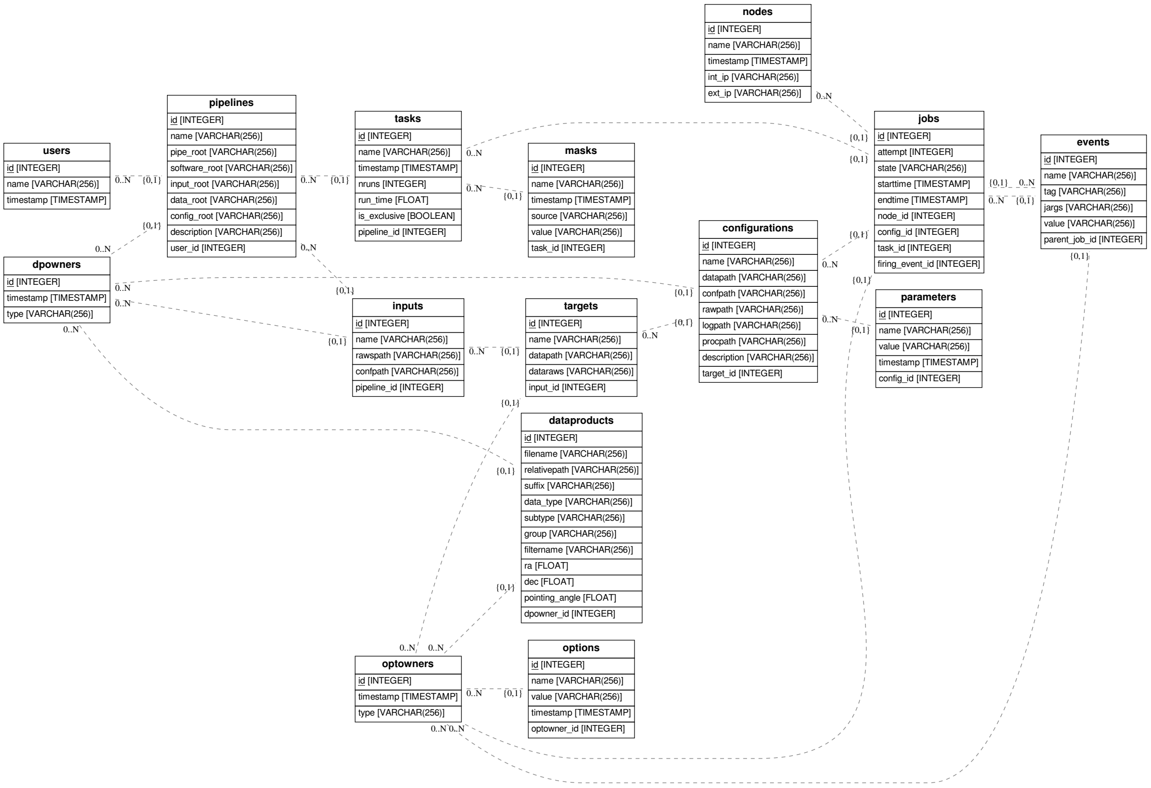

Figure 4.1: UML Class Diagram for the wpipe object-oriented and SQL database architecture from the Wpipe cookbook by Dr. Adrien Thob

Required Packages

4.1.4 Analysis: Pipeline Architecture

Sorting and Tagging

To begin the pipeline, we build our first task to take a directory containing the calibrated $FITS$ from the HST calibration pipeline. The *sort.py* task sorts PHAST FLC files based on field information, creates a structured DataFrame of raw data products, and compiles a list of unique target names for further analysis. Iterates through the unique target names, filtering data and creating individual target objects, streamlining the data processing workflow. Prepares configurations for each target and manages the processing of raw data products. This includes copying images to processing directory, starting tagging jobs, and tracking progress. When each image is done being sorted, each image is uniquely tagged with a ID where the pipeline can locate a call in the shared database. At the end of the *sort.py* task are left with a directories labeled with the target name and instrument as the name and containing sub-directories for the configuration files, processed files, log files and the original raw data for the images with the same targetname and instrument in the header. The dataproducts in the proc directory will be used for further processing in the pipeline and are the files that are tagged using the $tag_image.py$ in the SQL database.

Astrodrizzle

HST takes multiple observation of the same objects and these images need to be aligned to a common coordinate system to integrate the flux of object over multiple observations. STScI provides a package to preform this alignment called Astrodrizzle (https://www.stsci.edu/scientific-community/software/drizzlepac). The firing task can provide information to the next task giving us the flexibility to preform an array of operations. In the *astrodrizzle.py* task, it navigates to the */proc* directory of the target from the firing parent event and loads the appropriate configuration file. This configuration file contains parameters that control the behavior of the pipeline. It then retrieves the filter from the firing event. This filter is used to select specific raw data products from the list, creating a filtered list of data products for further processing. Optionally, If the RUN_DEEPCR parameter is set to 'T' and the files are Ultraviolet Imaging Spectrograph (UVIS) files, it runs the DeepCR algorithm, which is designed to identify and replace cosmic rays in the images. If the detector is Infrared (IR) or if RUN_DEEPCR is set to 'F', this step is skipped. Sets the default parameters for AstroDrizzle using the first image in the list. AstroDrizzle is a software package used for the automated combination of dithered images into a single composite image. These parameters are then appended to the configuration file. Executes AstroDrizzle on the list of images using the default parameters. This step combines the dithered images into a single, cleaned image. The Astrodrizzle output are stored in the labeled log file. After the task is complete, we are left with the drizzled FITS file $drc.fits$ for each filter in the sorted directory. The images are then tagged again with the Drizzled sub-type in the shared database then fires $find\_reference.py$.

Find Reference Image for Photmetry

The drizzled needs to set a reference image for each filter. Ideally the image with the longest exposure or a specified drizzled image. Using the target ID, it retrieves the targets associated dataproducts from the database with the subtype='DRIZZLED'. Looks for a reference image filter in the job configuration. If a reference image filter is found, it selects the drizzled image with the filter specified in the job configuration. If no reference image filter is found, it selects the drizzled image with the longest exposure time. Update the selected reference image sub-type to 'reference' and group to 'proc'. Logs the number of drizzled images found for the target. This information is useful for tracking the progress of the pipeline. The output images are now ready to be prepared for photometry processing using $prep\_image.py$ task.

Preparing Drizzled Images For DOLPHOT

Dolphin (2000) (DOLPHOT) package is the main workhorse for retrieving the photometry measurements. Before starting we have to prepare the image preforming DOLPHOT operation. The *prep_image.py* Sets the processing path and logs the start of the 'splitgroups' operation on the data product. Executes the 'splitgroups' operation using a subprocess. This operation splits the data product into individual groups. Creates data products from the output of the 'splitgroups' operation. These data products are images that have been prepped for further processing. Logs the creation of each data product and its associated options. Calculates the sky background for each image. If the detector option is 'UVIS', it runs the 'calcsky' operation. If the detector option is 'WFC', it logs the start of the 'calcsky' operation. Creates data products from the output of the 'calcsky' operation. These data products are images that have been prepped for further processing. When all images are finished being prepped we now make the DOLPHOT parameter that allows for specific tweaking to the DOLPHOT operation. The user can set certain parameters a head of time then fires the *make_param.py*.

The *make_param.py* task, Checks for user-specified parameters in the configuration. If a parameter is not specified by the user, it sets a default value for that parameter. Writes the parameters and their values to the targets configuration file. This file is used as input for other scripts in the pipeline. Defines global parameters for the pipeline. These parameters control the behavior of the pipeline and are used across multiple scripts for running DOLPHOT. Fires DOLPHOT events for the target called *run_dolphot*. The task retrieves the target and configuration associated with the job. The target is retrieved from the options of the firing event, and the configuration is used to set up the processing and logging paths. Iterates through all configuration dataproducts associated with the job. For each configuration dataproduct, it checks if the filename contains the string '.param' (the DOLPHOT parameter file). If so, it retrieves the dataproduct and uses it to set up the DOLPHOT operation. If not, it ignores the dataproduct. Retrieves the parameter file from the event options. This file contains parameters that control the behavior of the DOLPHOT operation. Checks that all necessary files (images, sky files, etc.) are present for the DOLPHOT operation. Constructs and executes the DOLPHOT command using the parameters from the parameter file. The output of the DOLPHOT operation is logged to a file. The DOLPHOT output will be the photometry catalog for the images given by the users. The DOLPHOT package provides log files with information about the DOLPHOT alignment, PSF and warning and are saved to the pipeline directory for review by the user.

Finally, the user is given a science ready photometry catalog. The pipeline provides a dynamic system allowing for user running the pipeline multiple times can add their own functions for their science use case using Python. Additionally, this also allows for users to manipulate pipeline task to implement their own calibration. We demonstrate this by implementing a deep-learning cosmic-ray rejection deepCR package Zhang & Bloom (2020); Chen et al. (2024) in the *sort.py* and *tag_image.py*. The task demonstrates how to use the wpipe objects and function to calibrate the input data.

4.1.5 User Pipeline Interaction

For the photometry pipeline, the user can provided specific parameters for the Astrodrizzle, DOLPHOT and local and remote directory manipulation. This can be done in the configuration file (*.conf*). The configuration file parameters will store default parameters as the pipeline process and tracks your images.

4.1.6 Results

We use the *wpipe* pipeline software package to develop a photometry pipeline based on the PHAT photometry catalog Williams et al. (2018). We demonstrate the pipeline capability of making a science ready photometry catalog for the PHAT observations (Dalcanton et al., 2012) by showing the pipeline architecture used to process, copy and track imaging data in a chained sequence. Secondly, we provide an example on how the pipeline can be changed to allow users to to implement their won calibration. Additionally, we show how users can use the configuration file to make changes to the included packages used to align and make photometry catalog(Astrodrizzle, DOLPHOT etc.). Currently the photometry pipeline is optimized to process calibrated images from HST and JWST datasets. The provided configuration file will all the user to add specific dataset parameters(sharp, crowd etc.).

- We provide an improved Python based photometry pipeline for current HST and JWST observation and will be used for the upcoming flagship data from the Roman Space Telescope.

- The pipeline will allow users to implement their own augmented steps using the WPIPE package tools

- The pipeline software is free a publicly available on Github

4.1.7 Conclusion: How will this be used for Roman Space Telescope

In conclusion, we demonstrate the benefits of creating a pipeline using the wpipe package. We show how we use the pipeline to build a photomtry pipeline and the ways that users can implement the changes. In future work, the pipeline will be optimized to produce a photometry catalog for the Roman Space Telescope, the next flagship UV and optical space observatory.

4.2 Deep-learning Applications for Hyperspectral Data

The expanding amount of data from galaxies observation provide a high quality datasets that can be used for various applications. Integral field spectroscopy surveys provide a spatially resolved spectroscopic datacubes to measure the unique chemical signature across the object. Hyperspectral imaging in the remote sensing domain uses similar technique to acquire the chemical composition and concentration of surface properties such as land cover and land use. Deep-learning techniques have mostly treated problems as an extension of RGB or multi-spectral imaging using convolutional neural network (CNN). CNNs are good for local features, but spectral data has ordered and long-ranging dependencies, maybe better suited for Recurrent Neural Networks(i.e. Long Short Term Models(LSTM)) and transformer approaches. Over the past few years various deep learning classification architecture have used a standard set of hyperspectral imaging datasets limited to a single data cube and label spatial map. In this work, we test a state-of-the-art classification model that shown to have high performance compared to other techniques with the the MaNGA survey multiple high quality spatial and spectral dataset to predict the ionization source map. We aim to demonstrate the accuracy of this model to identify ionization sources using the multiple datacube input. Utilizing larger datasets can significantly enhance the robustness of machine learning applications, particularly for stress testing classifiers.

4.2.1 Background

Hyperspectral imaging (HSI) is a remote sensing technique where the spatial and spectral bands are integrated to produce a spectral fingerprint for an observed object. The application of the technique is used in a wide range of fields including astronomy, mining, geology and medical field (Wu & Sun, 2013). In astronomy, integral field unit spectroscopy is the equivalent method to observe spatial information and spectral bands of star clusters, galaxies and other extensive objects in the nearby to high-redshift universe. Convolutional Neural Network (CNN) methods are widely applied to image recognition and image segmentation which considers the spatial correlation among pixels (Yang et al., 2018). CNN-based HSI classification (3D-CNN) have demonstrated high performance exploiting both spatial and spectral context.

In the past decade there have been model developed to predict the features from spatial and spectral dataset using the combination of CNNs and transformers. SpecTr Yun et al. (2021) is a model that has the the capability to model long-range dependency among spectral bands and explores the spectral and spatial bands. It does this by training a CNN to learning the context dependent sparsity(*definition*) features using a depth wise convolutions applying a filter to each spectral 2D image. Therefore they introduce spectral normalization, transformers and depth-wise convolution to produce spatial-spectral contextual feature maps with the same sequence length (i.e. wavebands). Another model was developed called CoTr Xie et al. (2021) which used a similar encoder and decoder structure to consist of a CNN and Transformers where the CNN is used to extract the feature map and the transformer captures the long-range dependencies i.e. the spectral dimension. They were able to achieve high model segmentation classification accuracy for 3D multi-organ datasets. Lastly, the Spectral–Spatial Feature Tokenization Transformer (SSFTT) (Sun et al., 2022) developed an a CNN and transformer structure that proved to improve HSI classification performance than the former architecture.

It is challenging to produce large HSI label datasets of land utilized by humans and the physical land in remote sensing domain resulting is small datasets. Indian Pine Baumgardner et al. (2015), Housten 2013 Duan et al. (2020) and the Pavia University dataset used in recent literature in HSI deep-learning application. These datasets wavebands range from $\sim 60-230$ spectral bands and use a single image to train and evaluate models. The SSFTT model demonstrate high classification performance for these datasets. In practice, classification models would train on multiple unique images to train and evaluate. We utilize the MaNGA survey (Bundy et al., 2014) that provide resolved dataset of nearby galaxies offers $\sim 10,000$ unique and high-quality datacubes to demonstrate the SSFTT model accuracy.

In galaxy evolution studies, there are a wide range spectroscopic diagnostic to classify nearby galaxies and the intrinsic properties that fuel star production and chemical inflow and outflow dynamics. The BPT diagnostic (Baldwin et al., 1981) as a label maps to train Spectral–Spatial Feature Tokenization Transformer (SSFTT) model to test the model performance in a real-world scenario. This analysis will provide a test for recovering accurate predication using 3D and 2D CNN and transformers model combination. Ionization state is a simple test case for more complicated assessments from spectra, like quantifying abundance patterns see Byler et al. (2024b). If the model has a high accuracy in recovering the ionization state, it can be used to for on the fly analysis and future survey data analysis.

In section 4.2.2, we introduce the MaNGA survey and how preprocessing the steps we applied to the datacubes. Additionally, we discuss how we create the label maps from the datacubes. In section 4.2.3 we show describe the SSFTT model architecture ,the sampling methods we used to split the datacube train test and validation split and the training model hyper-parameters we used in this analysis. Section 4.2.4 we briefly discuss future work to obtain the classification accuracy of SSFTT model using the MaNGA sample.

4.2.2 Data

SDSS-IV Mapping Nearby Galaxies at Apache Point Observatory (MaNGA) survey (Bundy et al., 2015) to collect integral field unit (IFU) spectroscopic measurements when available (see Section 2.2.2 for more detail.) We include Pipe3D catalog which is a value catalog that derived from the MaNGA catalog. Pipe3D is able to recover emission line and absorption features similar to DAP. We apply cuts from the Pipe3D catalog a subset of the full sample for rapid iteration of train/eval pipeline. We then select galaxies that have a total mass between $9.5 \leq Log(M_\star) \leq 11.0$ stellar mass. The visible gas attenuation within an effective radius (half-light radius) $A_{V,R_{eff}} < 2$ to mitigate high dust galaxies. We then select IFU sizes to be 127, 91 and 61. Finally, we aim to make sure we have face-on galaxies in the sample thus we include galaxies with a $inclination < 30°$ as a first past attempt, we encourage that this constraint can be lifted in future model training. The remaining galaxies are then ready to be separated into the training, test and validation dataset evenly where the sample is stratified sampled Singh & Masuku (2014) to ensure IFU size are distributed evenly.

After we reduce the MaNGA dataset to number of galaxies that meet the previous criteria we then apply a further constraints on the data as a whole to input into the classification model. As discussed in Byler et al. (2024a), we use the the `LOGCUBE-SPX-MILESHC-MASTARSSP` formatted output provided by the MaNGA Data Reduction Pipeline where the wavelength array is logarithmically binned and flux for the emission and absorption lines in the 1D spectrum on in units of $10^{-17} ergs/sec/cm^2/\mathring{A}/spaxel$. The cubes are corrected for redshift, wavelength cut where we set the wavelength range between $5000 - 8000\mathring{A}$ with 2040 wavelength elements. The cubes are then resampled so that the cube uses the same wavelength grid. Finally, the entire datacube are normalized between 0 and 1.

The BPT diagnostic diagram Baldwin et al. (1981) uses the emission line flux ratios to distinction primary ionization sources that produce the more recent stellar population. The BPT consist of diagnostic diagrams uses three emission line ratios using $[OIII]/H\beta$ as a function of $[NII]/H\alpha$, $[SII]/H\alpha$ and $[OI]/H\alpha$ and classifies galaxies being dominated with star-formation, active galactic nuclei, low ionization narrow emission line region(LINER) Seyfert or Seyfert-HII composite (AGN and star formation are both contributing to the energy source). Kewley et al. (2006) further refined the definition by adding a max starburst line (Kewley et al., 2001) where galaxies within the diagnostic diagram boundary would be considered star forming and Kauffmann et al. (2003a) provided an empirical line to divide pure star forming galaxies and Seyfert-HII composite with those galaxies. The BPT label maps are then generated from these fully reduced cubes. We refer to the BPT maps as the ionization maps throughout the analysis.

We use $[OIII]/H\beta$ as a function of $[NII]/H\alpha$ diagnostic to classify galaxies in to 3 classes, star forming, Seyfert-HII composite(composite hereafter) and AGN. We only use these line ratios because the $[SII]/H\alpha$ and $[OI]/H\alpha$ only distinction different types of AGN type ionization from star forming and the emission lines measurements are weaker making more challenging to detect Dopita et al. (2000); Fensch et al. (2016). [NII] emission is generally stronger emission and is easier to detect making it more robust as a diagnostic. The DAP provides emission lines maps for the ratios to be competed. We generate the label maps by using the BPT diagnostic diagrams. In Figure 4.2 We show the label maps of 6 random galaxies training sample color coded by the BPT classification of the spaxels. Further, we do not use single pixel spectra when training, instead we apply spatial patches (9x9x2040) centered around the central label spaxel.

We assume that the resolved BPT classification holds on the sub-kpc scale. Investigating the global BPT diagnostics hold on the kpc scale is out of the scope for this project but we note that previous analysis of the MaNGA galaxies have found that the young stellar population only slightly extend beyond adopted demarcation suggesting SF misclassification Belfiore et al. (2016), even in higher resolution observation shows only a slight misclassification Fensch et al. (2016).

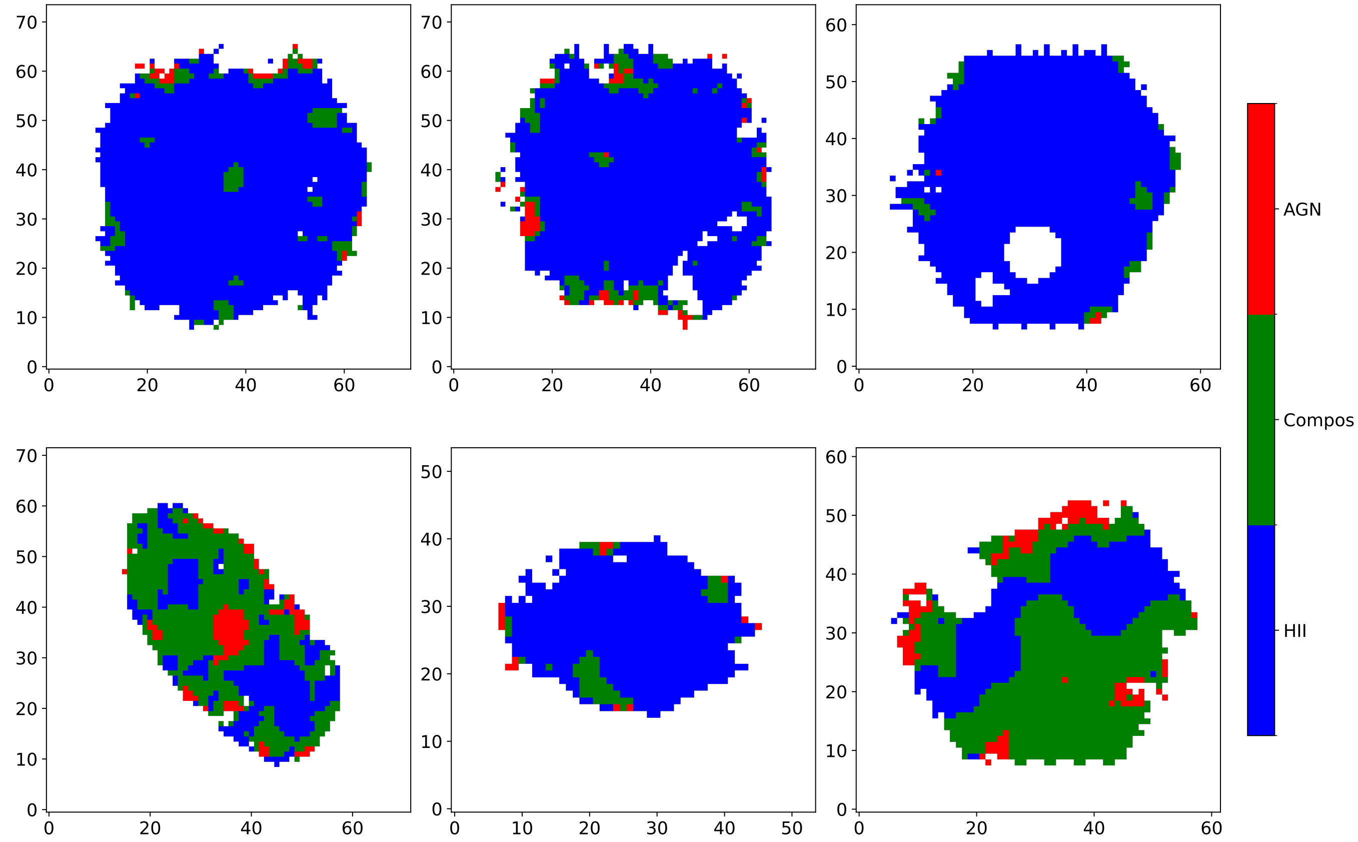

Figure 4.2: BPT label map randomly sampled from the train dataset showing the spatial distribution of the 3 ionization classes from the O3Hβ vs N2Hα BPT diagnostic diagram where HII, Composite, AGN are represented as blue, green and red.

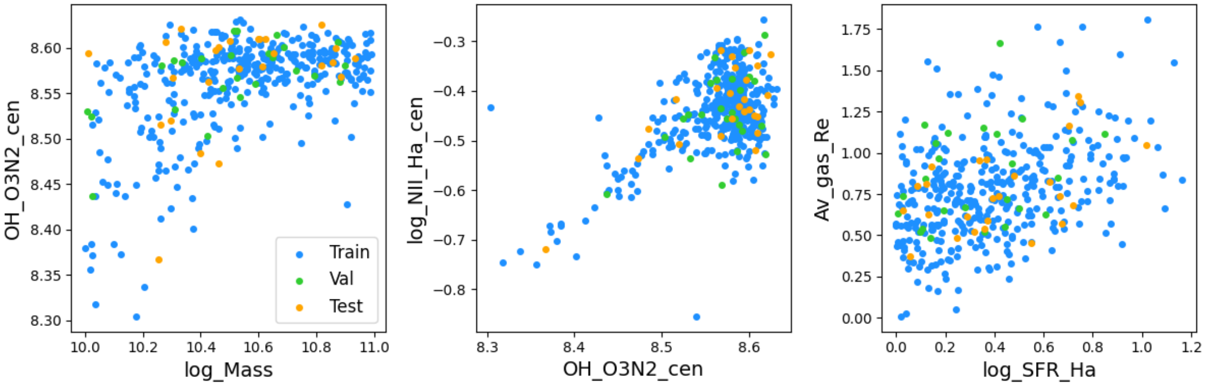

Figure 4.3: The Mass-Metallicity Relation, the N2Hα vs. Metallicity and the gas visible attenuation vs star formation rate plots of the training[blue], testing[orange] and validation[green] datacubes. These values were provided by the Pipe3D catalog table and represent the reduced datacubes for training the deep-learning model.

4.2.3 Method

SSFTT Model Structure

In this analysis, we use the Spectral - Spatial Feature Tokenization Transformer (SSFTT) Sun et al. (2022). The deep-learning classification model integrates CNN and transformer structure. The model consist of a 3D CNN layer and then a 2D layer to localize feature extraction in spatial and spectral dimension. The localized features are then transformed using a Transformer to produce tokenized low-middle-deep semantic features of the hyperspectral imaging. The aim is to express the deep semantic feature as a token with distribution characteristics in line with the sample. Therefore making the sample more separable. See Sun et al. (2022) for a full description of the model architecture.

The SSFTT has been compared to recent state-of-the art CNN and transformer structure HSI classification models and shown to be the most accurate in it's prediction to classify spectral-spatial features by expressing the low - deep semantic features of the hyperspectral concisely and efficientlySun et al. (2022). However, their is a possibility of over-fitting given the training dataset. We use this model to test the robustness of the model in a more representative real world scenario where the user has a large quantity of independent datacubes. The MaNGA survey provides datacubes of individual galaxies with unique spatial and spectral features.

Train, Test and Validation Split

We utilize 200 MaNGA datacubes with their corresponding label maps. The data is split into training, validation, and test sets with an 80/10/10 ratio. To address the potential issue of class imbalance in the training data, we use an imbalanced sampler instead of random sampling. This approach helps to counteract the bias toward the dominant class that might occur with a random split, thus mitigating the risk of poor model performance and misclassification.

For performance evaluation, we employed two methods to split the data: the imbalanced sampler and the stratified method. The imbalanced sampler ensures that each class is represented proportionally within each split, balancing the training process despite the inherent class distribution. In contrast, the stratified sampling method was applied to create roughly matching bin distribution for the data split. These bins are then grouped by PLATE-IFU, redshift, and IFU size to maintain a more balanced representation across the splits. We used the StratifiedShuffleSplit function from the Scikit-Learn Python package for this purpose. The datacubes were binned by BPT labels, with star-forming (SF) = 1, composite (COMP) = 2, and active galactic nuclei (AGN) = 3. This method ensures an even distribution of these labels across the train, validation, and test sets.

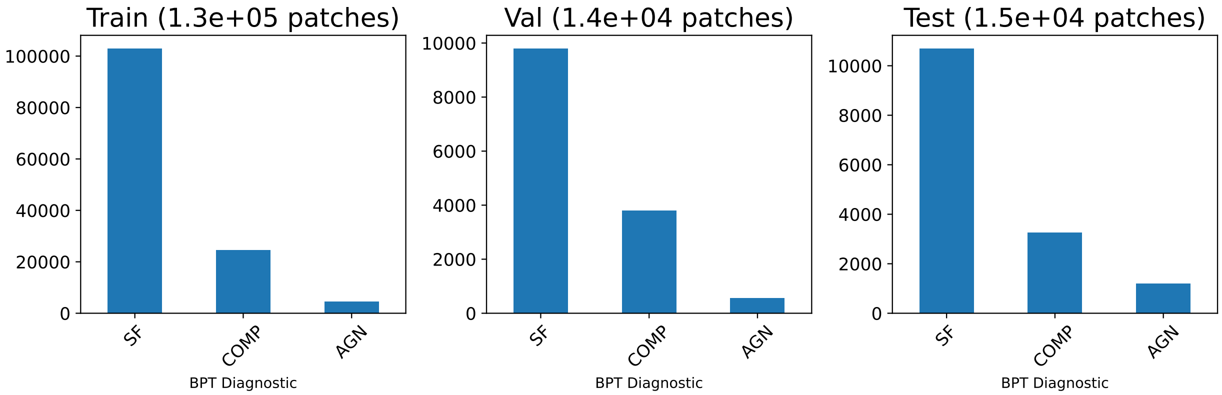

Figure 4.4: The patches distribution for the training, test and validation sets. The star-forming class is dominate in all datasets. We use an imbalanced sampler to for training the model to mitigate the affects of the dominate class.

Training Hyper-parameters

The SSFTT model training setup is adapted from Byler et al. (2024b) with minor modifications to incorporate the BPT maps. The model's hyper-parameters are detailed here. We input MaNGA datacubes and use the Adam optimizer to minimize cross-entropy loss during training. The learning rate, weight decay, and momentum parameters are consistent with those used in Byler et al. (2024b). The training process spans 130 epochs with a batch size $b = 1024$.

4.2.4 Future Work

At the time of this submission, we do not have results of this analysis but future work will highlight the results of using the SSFTT model to predict the ionization source. Byler et al. (2024b) did an extensive study on the SSFTT architecture and other architecture to predict the metallicity concentration as the label map.

Chapter 5

CONCLUDING REMARKS AND FUTURE WORK

The research presented in this dissertation made use of integral field unit spectroscopy and stellar photometry to measure the chemical abundance, star formation, mass, and age of nearby galaxies. Nearby galaxies provided insight into the complex recent history of galaxies over cosmic time. In my analysis, I measured various properties of the stellar population, chemical abundance, and star formation production as a function of radius, called radial profiles. We compared these profiles to investigate notable differences and similarities to learn more about the recent evolution across the disk.

In Chapter 2, we investigated the radial distribution of centrally star-forming galaxies with photometrically red disks, called BreakBRD galaxies, compared to centrally young (CSF), intermediate (CGV), and old (CQC) galaxies. We used the MaNGA survey to investigate the distribution on a sub-kpc scale and compared the distributions to each other. We presented that the BreakBRD galaxies' stellar age radial profiles deviated from the other samples, showing a steep increasing slope, whereas the stellar age distribution for the other samples was almost flat, in agreement with the claim that these galaxies had a younger central stellar age and a noticeably older disk. Additionally, we showed that the stellar mass distribution of all samples exhibited a monotonic decline, indicating that mass assembly did not play a major role in the central age difference of the BreakBRD galaxies. Further, the BreakBRD galaxies produced more stars in the central region, similar to the CSF and CQC samples. Though the disk had a lower star formation rate and efficiency, the BreakBRD galaxies' disks were not quenched and might have had enough neutral gas to continue forming stars in recent epochs. Finally, the metallicity showed a decreasing radial profile for all samples, in agreement with inside-out formation but did not significantly deviate to draw conclusions about the impact of metallicity on central star formation. We concluded that the BreakBRD galaxies were indeed centrally young, had noticeably positive stellar age radial profile slopes, and that the disk appeared to have an older stellar population but also showed signs of recent star production, though at a lower rate and efficiency than the central bulge.

In Chapter 3, we used stellar photometry of RGB stars to measure the metallicity gradients of the Andromeda galaxy (M31). The stellar photometry came from two HST surveys, PHAT and PHAST, which observed the northern and southern halves, respectively. From previous analysis, the PHAT RGB metallicity gradient had a negative slope of -0.02 dex/kpc, assuming a flat fiducial age of 4 Gyr, with the metallicity distribution function (MDF) having a median of approximately -0.11 [M/H] dex. In our analysis, we presented the RGB metallicity gradient and MDF for the PHAST catalog and combined the PHAT and PHAST catalogs to show the M31 catalog. We found that the PHAT, PHAST, and M31 radial profiles had a shallow metallicity gradient slope of -0.01 dex/kpc, only a 0.01 dex difference from previous work. The difference was likely due to the different methods used to remove high dust mass regions and from our analysis not applying a completeness or photometric bias to the stars catalog. The PHAT and PHAST catalogs shared similar radial profiles and slopes, even including the highest dust mass regions. Still, the M31 RGB metallicity had a shallow gradient, in agreement with previous work. The M31 radial profile showed a flat high metallicity plateau from approximately 5 to 13 kpc and overlapped with previous analysis where the metal-rich bar was observed. Future work will investigate the details of the high-mass bar stellar population.

In Chapter 4, we built on the large datasets from stellar photometry and integral field unit spectroscopy and presented a photometry pipeline and deep-learning classification model. We shared a photometry pipeline that used HST and JWST observations to clean, align, and manage high resolution and produced the photometry catalog used to create the PHAST catalog presented earlier. The pipeline was managed by the wpipe Python package and SQL to track and manage the data as it moved through the pipeline. The current pipeline we presented was an improvement from the previous one in that it was built entirely in Python, the most widely used computer language. Additionally, the pipeline had the capability to be user-friendly, including the ability to label data products and resume the pipeline if interrupted. Finally, it allowed users to input their own parameters to adjust for their scientific needs. The pipeline would be used in future flagship observatories to produce photometry catalogs.

We attempted to use a deep-learning classification model to predict the ionization status for MaNGA galaxies from 3D datacubes, building off the large datacubes of approximately 10,000 galaxies. We used the emission line maps derived from the datacubes and applied the BPT diagnostic to classify the spaxels by ionization source. The model was given the 3D datacube and labels to output the predicted values. The aim of this analysis was to use a state-of-the-art hyperspectral imaging classifier in real-world data scenarios where the data came from multiple and varying sources. The model analysis demonstrated that the model had strong performance when using individual datasets with a single label image. We found that the SSFTT might show state-of-the-art performance on Indian Pines, but that was due to overfitting to the local scene conditions. When using a more appropriate split approach, it did not perform well. We demonstrated that the massive dataset of the MaNGA survey could be utilized for testing current model performance.

By investigating the radial distribution of nearby star-forming galaxies and their stellar chemical abundance, this dissertation research contributed to a deeper understanding of galaxies on sub-kpc scales. Future and advanced studies on sub-kpc scales will be able to resolve separate stellar populations, dissect complex gas and stellar populations from merger populations. Larger surveys aimed to quadruple the IFU size and increase sensitivity to observe the intergalactic gas surrounding nearby galaxies to investigate signs of accretion remnants. Additionally, multi-wavelength observations from space-based telescopes provided access to different stellar populations. JWST allowed for the study of the gas and stellar composition of high-redshift galaxies, providing constraints on the composition of galaxies a few Gyr ago using IFU spectroscopy. Roman would probe the UV and provide deep insight into the younger and more energetic stellar populations. These future surveys will offer a more complete interpretation of the measurements of galaxy composition and complex star formation history.

BIBLIOGRAPHY

Akeson, R., Armus, L., Bachelet, E., et al. 2019, arXiv e-prints, arXiv:1902.05569

Arnaboldi, M., Bhattacharya, S., Gerhard, O., et al. 2022, Astronomy & Astrophysics, 666, A109. https://www.aanda.org/10.1051/0004-6361/202244258https://www.aanda.org/10.1051/0004-6361/202244258

Bakos, J., Trujillo, I., & Pohlen, M. 2008, The Astrophysical Journal, 683, L103. https://doi.org/10.1086/591671https://doi.org/10.1086/591671

Baldwin, J. A., Phillips, M. M., & Terlevich, R. 1981, PASP, 93, 5

Baldwin, J. A., Phillips, M. M., & Terlevich, R. 1981, Publications of the Astronomical Society of the Pacific, 93, 5. http://iopscience.iop.org/article/10.1086/130766http://iopscience.iop.org/article/10.1086/130766

Balogh, M. L., Morris, S. L., Yee, H. K. C., Carlberg, R. G., & Ellingson, E. 1999, ApJ, 527, 54

Baumgardner, M. F., Biehl, L. L., & Landgrebe, D. A. 2015, doi:doi:/10.4231/R7RX991C. https://purr.purdue.edu/publications/1947/1https://purr.purdue.edu/publications/1947/1

Belfiore, F., Maiolino, R., Maraston, C., et al. 2016, Monthly Notices of the Royal Astronomical Society, 461, 3111. https://academic.oup.com/mnras/article-lookup/doi/10.1093/mnras/stw1234https://academic.oup.com/mnras/article-lookup/doi/10.1093/mnras/stw1234

Belfiore, F., Maiolino, R., Tremonti, C., et al. 2017, Monthly Notices of the Royal Astronomical Society, 469, 151, arXiv:1703.03813 [astro-ph]. http://arxiv.org/abs/1703.03813http://arxiv.org/abs/1703.03813

Belfiore, F., Westfall, K. B., Schaefer, A., et al. 2019, AJ, 158, 160

Bell, E. F., & de Jong, R. S. 2001, The Astrophysical Journal, 550, 212. https://doi.org/10.1086/319728https://doi.org/10.1086/319728

Blair, W. P., Kirshner, R. P., & Chevalier, R. A. 1982, The Astrophysical Journal, 254, 50. http://adsabs.harvard.edu/doi/10.1086/159703http://adsabs.harvard.edu/doi/10.1086/159703

Blanton, M. R., & Moustakas, J. 2009, Annual Review of Astronomy and Astrophysics, 47, 159–210. http://dx.doi.org/10.1146/annurev-astro-082708-101734http://dx.doi.org/10.1146/annurev-astro-082708-101734

Bluck, A. F. L., Maiolino, R., Piotrowska, J. M., et al. 2020, Monthly Notices of the Royal Astronomical Society, 499, 230–268. http://dx.doi.org/10.1093/mnras/staa2806http://dx.doi.org/10.1093/mnras/staa2806

Breda, I., Papaderos, P., Gomes, J. M., et al. 2020, 7

Breda, I., Papaderos, P., Gomes, J. M., et al. 2020, A&A, 635, A177

Bressan, A., Marigo, P., Girardi, L., et al. 2012, Monthly Notices of the Royal Astronomical Society, 427, 127, arXiv:1208.4498 [astro-ph]. http://arxiv.org/abs/1208.4498http://arxiv.org/abs/1208.4498

Brinchmann, J., Charlot, S., White, S. D. M., et al. 2004, MNRAS, 351, 1151

Brook, C., Richard, S., Kawata, D., Martel, H., & Gibson, B. K. 2007, The Astrophysical Journal, 658, 60. https://doi.org/10.1086/511056https://doi.org/10.1086/511056

Bruzual A., G. 1983, ApJ, 273, 105

Bundy, K., Bershady, M. A., Law, D. R., et al. 2014, The Astrophysical Journal, 798, 7. http://stacks.iop.org/0004-637X/798/i=1/a=7?key=crossref.ce8f697114eeb3752ff6da50e3e66986http://stacks.iop.org/0004-637X/798/i=1/a=7?key=crossref.ce8f697114eeb3752ff6da50e3e66986

—. 2015, The Astrophysical Journal, 798, 7. https://doi.org/10.1088/0004-637x/798/1/7https://doi.org/10.1088/0004-637x/798/1/7

Byler, E., Forland, B., & McKay, M. 2024a, in Algorithms, Technologies, and Applications for Multispectral and Hyperspectral Imaging XXX, ed. M. Velez-Reyes & D. W. Messinger, Vol. 13031, International Society for Optics and Photonics (SPIE), 130310I. https://doi.org/10.1117/12.3012800https://doi.org/10.1117/12.3012800

Byler, E. B., Forland, B. M., & McKay, M. 2024b, in Algorithms, Technologies, and Applications for Multispectral and Hyperspectral Imaging XXX, ed. D. W. Messinger & M. Velez-Reyes (National Harbor, United States: SPIE), 25. https://www.spiedigitallibrary.org/conference-proceedings-of-spie/13031/3012800/Chemical-signature-characterization-with-hyperspectral-imagery–novel-deep-learning/10.1117/12.3012800.fullhttps://www.spiedigitallibrary.org/conference-proceedings-of-spie/13031/3012800/Chemical-signature-characterization-with-hyperspectral-imagery–novel-deep-learning/10.1117/12.3012800.full

Calzetti, D. 2001, PASP, 113, 1449

Cardelli, J. A., Clayton, G. C., & Mathis, J. S. 1989, ApJ, 345, 245

Chen, G., Zhang, H.-X., Kong, X., et al. 2020, The Astrophysical Journal, 895, 146, arXiv: 2004.13044. http://arxiv.org/abs/2004.13044http://arxiv.org/abs/2004.13044

Chen, Y., Girardi, L., Bressan, A., et al. 2014, Monthly Notices of the Royal Astronomical Society, 444, 2525.

http://academic.oup.com/mnras/article/444/3/2525/1061098/Improving-PARSEC-models-for-very-low-mass-starshttp://academic.oup.com/mnras/article/444/3/2525/1061098/Improving
PARSEC-models-for-very-low-mass-stars

Chen, Z. Zhang, K. Williams, B. F., & Durbin, M. 2024, The Astrophysical Journal, 962, 7. https://iopscience.iop.org/article/10.3847/1538-4357/ad1602https://iopscience.iop.org/article/10.3847/1538-4357/ad1602

Courteau, S., Widrow, L. M., McDonald, M., et al. 2011, The Astrophysical Journal, 739, 20. https://iopscience.iop.org/article/10.1088/0004-637X/739/1/20https://iopscience.iop.org/article/10.1088/0004-637X/739/1/20

Croom, S. M., Lawrence, J. S., Bland-Hawthorn, J., et al. 2012, Monthly Notices of the Royal Astronomical Society, no. https://academic.oup.com/mnras/article-lookup/doi/10.1111/j.1365-2966.2011.20365.xhttps://academic.oup.com/mnras/article-lookup/doi/10.1111/j.1365-2966.2011.20365.x

Dalcanton, J. J., Williams, B. F., Lang, D., et al. 2012, The Astrophysical Journal Supplement Series, 200, 18, arXiv: 1204.0010. http://arxiv.org/abs/1204.0010http://arxiv.org/abs/1204.0010

Dalcanton, J. J., Williams, B. F., Lang, D., et al. 2012, ApJS, 200, 18

Dalcanton, J. J., Fouesneau, M., Hogg, D. W., et al. 2015, The Astrophysical Journal, 814, 3. https://iopscience.iop.org/article/10.1088/0004-637X/814/1/3https://iopscience.iop.org/article/10.1088/0004-637X/814/1/3

Dekel, A., Birnboim, Y., Engel, G., et al. 2009, Nature, 457, 451, arXiv:0808.0553 [astro-ph]. http://arxiv.org/abs/0808.0553http://arxiv.org/abs/0808.0553

Delgado, R. M. G., Pérez, E., Fernandes, R. C., et al. 2013, arXiv:1310.5517 [astro-ph], doi:10.1051/0004-6361/201322011, arXiv: 1310.5517. http://arxiv.org/abs/1310.5517http://arxiv.org/abs/1310.5517

Dennefeld, M., & Kunth, D. 1981, AJ, 86, 989

Dolphin, A. E. 2000, Publications of the Astronomical Society of the Pacific, 112, 1383, arXiv:astro-ph/0006217. http://arxiv.org/abs/astro-ph/0006217http://arxiv.org/abs/astro-ph/0006217

Dopita, M. A., Kewley, L. J., Heisler, C. A., & Sutherland, R. S. 2000, ApJ, 542, 224

Draine, B. T., & Li, A. 2007, The Astrophysical Journal, 657, 810. https://iopscience.iop.org/article/10.1086/511055https://iopscience.iop.org/article/10.1086/511055

Draine, B. T., Aniano, G., Krause, O., et al. 2013, The Astrophysical Journal, 780, 172. https://iopscience.iop.org/article/10.1088/0004-637X/780/2/172https://iopscience.iop.org/article/10.1088/0004-637X/780/2/172

Drory, N., MacDonald, N., Bershady, M. A., et al. 2015, AJ, 149, 77

Duan, P., Kang, X., Ghamisi, P., & Liu, Y. 2020, Remote Sensing, 12, 4034

Fensch, J., Duc, P.-A., Weilbacher, P. M., Boquien, M., & Zackrisson, E. 2016, Astronomy & Astrophysics, 585, A79. http://www.aanda.org/10.1051/0004-6361/201527141http://www.aanda.org/10.1051/0004-6361/201527141

Fernández, R. L., Delgado, R. M. G., Pérez, E., et al. 2018, Astronomy & Astrophysics, 615, A27, arXiv: 1802.10118. http://arxiv.org/abs/1802.10118http://arxiv.org/abs/1802.10118

Freedman, W. L. 1986, Symposium - International Astronomical Union, 116, 61. https://www.cambridge.org/core/product/identifier/S0074180900148636/type/journal$_{a}rticlehttps : //u$

Galarza, V. C., Walterbos, R. A. M., & Braun, R. 1999, The Astronomical Journal, 118, 2775. https://dx.doi.org/10.1086/301113https://dx.doi.org/10.1086/301113

Gallazzi, A., Charlot, S., Brinchmann, J., White, S. D. M., & Tremonti, C. A. 2005, MNRAS, 362, 41

Gardner, J. P., Mather, J. C., Clampin, M., et al. 2006, Space Science Reviews, 123, 485, arXiv:astro-ph/0606175. http://arxiv.org/abs/astro-ph/0606175http://arxiv.org/abs/astro-ph/0606175

Gehrig, L., Steindl, T., Vorobyov, E. I., Guadarrama, R., & Zwintz, K. 2023, Astronomy & Astrophysics, 669, A84. https://www.aanda.org/10.1051/0004-6361/202244408https://www.aanda.org/10.1051/0004-6361/202244408

Gilbert, K. M., Kalirai, J. S., Guhathakurta, P., et al. 2014, The Astrophysical Journal, 796, 76, arXiv:1409.3843 [astro-ph]. http://arxiv.org/abs/1409.3843http://arxiv.org/abs/1409.3843

Goddard, D., Thomas, D., Maraston, C., et al. 2017, 28

González Delgado, R. M., Pérez, E., Cid Fernandes, R., et al. 2014, A&A, 562, A47

González Delgado, R. M., García-Benito, R., Pérez, E., et al. 2015, A&A, 581, A103

Gregersen, D., Seth, A. C., Williams, B. F., et al. 2015, The Astronomical Journal, 150, 189, arXiv:1511.00006 [astro-ph]. http://arxiv.org/abs/1511.00006http://arxiv.org/abs/1511.00006

Gunn, J. E., & Gott, J. Richard, I. 1972, ApJ, 176, 1

Hilz, M., Naab, T., & Ostriker, J. P. 2013, MNRAS, 429, 2924

Ibarra-Medel, H. J., Sánchez, S. F., Avila-Reese, V., et al. 2016, Monthly Notices of the Royal Astronomical Society, 463, 2799. https://doi.org/10.1093/mnras/stw2126https://doi.org/10.1093/mnras/stw2126

Johnson, L. C., Seth, A. C., Dalcanton, J. J., et al. 2016, The Astrophysical Journal, 827, 33. https://iopscience.iop.org/article/10.3847/0004-637X/827/1/33https://iopscience.iop.org/article/10.3847/0004-637X/827/1/33

Kauffmann, G., Heckman, T. M., White, S. D. M., et al. 2003a, MNRAS, 341, 33

Kauffmann, G., Heckman, T. M., Tremonti, C., et al. 2003b, MNRAS, 346, 1055

Kennicutt, Robert C., J. 1998, ARA&A, 36, 189

Kennicutt, Robert C., J., Keel, W. C., & Blaha, C. A. 1989, AJ, 97, 1022

Kennicutt, Robert C., J., Tamblyn, P., & Congdon, C. E. 1994, ApJ, 435, 22

Kepner, J. 1999, The Astrophysical Journal, 520, 59, arXiv: astro-ph/9710329. http://arxiv.org/abs/astro-ph/9710329http://arxiv.org/abs/astro-ph/9710329

Kewley, L. J., & Dopita, M. A. 2002, ApJS, 142, 35

Kewley, L. J., Dopita, M. A., Sutherland, R. S., Heisler, C. A., & Trevena, J. 2001, The Astrophysical Journal, 556, 121, arXiv: astro-ph/0106324. http://arxiv.org/abs/astro-ph/0106324http://arxiv.org/abs/astro-ph/0106324

Kewley, L. J., Groves, B., Kauffmann, G., & Heckman, T. 2006, Monthly Notices of the Royal Astronomical Society, 372, 961. https://doi.org/10.1111/j.1365-2966.2006.10859.xhttps://doi.org/10.1111/j.1365-2966.2006.10859.x

Kewley, L. J., Nicholls, D. C., & Sutherland, R. S. 2019, ARA&A, 57, 511

Kroupa, P. 2001, MNRAS, 322, 231

Lackner, C. N., & Gunn, J. E. 2012, Monthly Notices of the Royal Astronomical Society, 428, 2141. https://doi.org/10.1093/mnras/sts179https://doi.org/10.1093/mnras/sts179

Larson, R. B. 1976, Monthly Notices of the Royal Astronomical Society, 176, 31. https://academic.oup.com/mnras/article-lookup/doi/10.1093/mnras/176.1.31https://academic.oup.com/mnras/article-lookup/doi/10.1093/mnras/176.1.31

Law, D. R., Cherinka, B., Yan, R., et al. 2016, The Astronomical Journal, 152, 83, arXiv:1607.08619 [astro-ph]. http://arxiv.org/abs/1607.08619http://arxiv.org/abs/1607.08619

Law, D. R., Cherinka, B., Yan, R., et al. 2016, AJ, 152, 83

Ma, X., Hopkins, P. F., Faucher-Giguère, C.-A., et al. 2016, Monthly Notices of the Royal Astronomical Society, 456, 2140. https://academic.oup.com/mnras/article-lookup/doi/10.1093/mnras/stv2659https://academic.oup.com/mnras/article-lookup/doi/10.1093/mnras/stv2659

Magrini, L., Coccato, L., Stanghellini, L., Casasola, V., & Galli, D. 2016, Astronomy & Astrophysics, 588, A91. http://www.aanda.org/10.1051/0004-6361/201527799http://www.aanda.org/10.1051/0004-6361/201527799

Mo, H. J., Mao, S., & White, S. D. M. 1998, 18

Mo, H. J., Mao, S., & White, S. D. M. 1998, MNRAS, 295, 319

Nelson, E. J., van Dokkum, P. G., Förster Schreiber, N. M., et al. 2016, The Astrophysical Journal, 828, 27. https://iopscience.iop.org/article/10.3847/0004-637X/828/1/27https://iopscience.iop.org/article/10.3847/0004-637X/828/1/27

Pagel, B. E. J., & Edmunds, M. G. 1981, ARA&A, 19, 77

Pan, Z., Li, J., Lin, W., et al. 2015, ApJ, 804, L42

Parikh, T., Thomas, D., Maraston, C., et al. 2021, MNRAS, 502, 5508

Peletier, R. F., & Valentijn, E. A. 1989, Ap&SS, 156, 127

Pérez, E., Cid Fernandes, R., González Delgado, R. M., et al. 2013, ApJ, 764, L1

Pettini, M., & Pagel, B. E. J. 2004, Monthly Notices of the Royal Astronomical Society, 348, L59, arXiv: astro-ph/0401128. http://arxiv.org/abs/astro-ph/0401128http://arxiv.org/abs/astro-ph/0401128

Peña, M., & Flores-Durán, S. N. 2019, Revista Mexicana de Astronomía y Astrofísica, 55, 255, arXiv:1907.05797 [astro-ph]. http://arxiv.org/abs/1907.05797http://arxiv.org/abs/1907.05797

Poetrodjojo, H., Groves, B., Kewley, L. J., et al. 2018, Monthly Notices of the Royal Astronomical Society, 479, 5235, arXiv: 1807.01522. http://arxiv.org/abs/1807.01522http://arxiv.org/abs/1807.01522

Pérez, E., Fernandes, R. C., Delgado, R. M. G., et al. 2013, arXiv:1301.1679 [astro-ph], doi:10.1088/2041-8205/763/1/L1, arXiv: 1301.1679. http://arxiv.org/abs/1301.1679http://arxiv.org/abs/1301.1679

Renzini, A., & Peng, Y.-j. 2015, ApJ, 801, L29

Salim, S., Rich, R. M., Charlot, S., et al. 2007, ApJS, 173, 267

Sanchez, N. N., Werk, J. K., Tremmel, M., et al. 2019, The Astrophysical Journal, 882, 8. https://iopscience.iop.org/article/10.3847/1538-4357/ab3045https://iopscience.iop.org/article/10.3847/1538-4357/ab3045

Sanchez, S. F. 2020, Annual Review of Astronomy and Astrophysics, 58, 99, arXiv:1911.06925 [astro-ph]. http://arxiv.org/abs/1911.06925http://arxiv.org/abs/1911.06925

Sánchez, S. F., Pérez, E., Sánchez-Blázquez, P., et al. 2016a, Rev. Mexicana Astron. Astrofis., 52, 21

—. 2016b, Rev. Mexicana Astron. Astrofis., 52, 171

Sanchez-Blazquez, P., Peletier, R. F., Jimenez-Vicente, J., et al. 2006, Monthly Notices of the Royal Astronomical Society, 371, 703. https://academic.oup.com/mnras/article-lookup/doi/10.1111/j.1365-2966.2006.10699.xhttps://academic.oup.com/mnras/article-lookup/doi/10.1111/j.1365-2966.2006.10699.x

Sanders, N., Caldwell, N., McDowell, J., & Harding, P. 2012, The Astrophysical Journal, 758, 133, arXiv:1209.2251 [astro-ph]. http://arxiv.org/abs/1209.2251http://arxiv.org/abs/1209.2251

Schmidt, M. 1959, The astrophysical journal, 129, 243

Singh, A., & Masuku, M. 2014, International Journal of Commerce and Management, 2, 1

Speagle, J. S., Steinhardt, C. L., Capak, P. L., & Silverman, J. D. 2014, ApJS, 214, 15

Sun, L., Zhao, G., Zheng, Y., & Wu, Z. 2022, IEEE Trans. Geosci. Remote Sensing, 60, 1. https://ieeexplore.ieee.org/document/9684381/https://ieeexplore.ieee.org/document/9684381/

Sánchez, S. F. 2020, Annual Review of Astronomy and Astrophysics, 58, 99–155. http://dx.doi.org/10.1146/annurev-astro-012120-013326http://dx.doi.org/10.1146/annurev-astro-012120-013326

Sánchez, S. F., Rosales-Ortega, F. F., Iglesias-Páramo, J., et al. 2014, Astronomy & Astrophysics, 563, A49. http://www.aanda.org/10.1051/0004-6361/201322343http://www.aanda.org/10.1051/0004-6361/201322343

Sánchez, S. F., Pérez, E., Sánchez-Blázquez, P., et al. 2015, Pipe3D, a pipeline to analyze Integral Field Spectroscopy data: I. New fitting phylosophy of FIT3D, , , arXiv:1509.08552

Sánchez, S. F., García-Benito, R., Zibetti, S., et al. 2016a, Astronomy & Astrophysics, 594, A36, arXiv: 1604.02289. http://arxiv.org/abs/1604.02289http://arxiv.org/abs/1604.02289

Sánchez, S. F., Pérez, E., Sánchez-Blázquez, P., et al. 2016b, Pipe3D, a pipeline to analyse integral field spectroscopy data: II. Analysis sequence and CALIFA dataproducts, arXiv, arXiv:1602.01830 [astro-ph]. http://arxiv.org/abs/1602.01830http://arxiv.org/abs/1602.01830

Tang, J., Bressan, A., Rosenfield, P., et al. 2014, Monthly Notices of the Royal Astronomical Society, 445, 4287. http://academic.oup.com/mnras/article/445/4/4287/1752836/New-PARSEC-evolutionary-tracks-of-massive-stars-athttp://academic.oup.com/mnras/article/445/4/4287/1752836/Ne PARSEC-evolutionary-tracks-of-massive-stars-at

Teklu, B. B., Gao, Y., Kong, X., Lin, Z., & Liang, Z. 2020, ApJ, 897, 61

Trundle, C., Dufton, P. L., Lennon, D. J., Smartt, S. J., & Urbaneja, M. A. 2002, Astronomy & Astrophysics, 395, 519, arXiv:astro-ph/0207198. http://arxiv.org/abs/astro-ph/0207198http://arxiv.org/abs/astro-ph/0207198

Tuttle, S. E., & Tonnesen, S. 2020, The Astrophysical Journal, 889, 188. http://dx.doi.org/10.3847/1538-4357/ab5dbbhttp://dx.doi.org/10.3847/1538-4357/ab5dbb

Urrutia, T., Wisotzki, L., Kerutt, J., et al. 2019, A&A, 624, A141

Wake, D. A., Bundy, K., Diamond-Stanic, A. M., et al. 2017, AJ, 154, 86

Westfall, K. B., Cappellari, M., Bershady, M. A., et al. 2019, The Astronomical Journal, 158, 231. https://iopscience.iop.org/article/10.3847/1538-3881/ab44a2https://iopscience.iop.org/article/10.3847/1538-3881/ab44a2

Westfall, K. B., Cappellari, M., Bershady, M. A., et al. 2019, AJ, 158, 231

White, S. D., & Frenk, C. S. 1991, The Astrophysical Journal, 379, 52

Williams, B. F., Olsen, K., Khan, R., Pirone, D., & Rosema, K. 2018, ApJS, 236, 4

Williams, B. F., Olsen, K., Khan, R., Pirone, D., & Rosema, K. 2018, The Astrophysical Journal Supplement Series, 236, 4, arXiv:1802.06088 [astro-ph]. http://arxiv.org/abs/1802.06088http://arxiv.org/abs/1802.06088

Williams, B. F., Lang, D., Dalcanton, J. J., et al. 2014, The Astrophysical Journal Supplement Series, 215, 9. https://iopscience.iop.org/article/10.1088/0067-0049/215/1/9https://iopscience.iop.org/article/10.1088/0067-0049/215/1/9

Williams, B. F., Durbin, M. J., Dalcanton, J. J., et al. 2021, The Astrophysical Journal Supplement Series, 253, 53, arXiv:2101.01293 [astro-ph]. http://arxiv.org/abs/2101.01293http://arxiv.org/abs/2101.01293

Williams, B. F., Durbin, M., Lang, D., et al. 2023, The Panchromatic Hubble Andromeda Treasury XXI. The Legacy Resolved Stellar Photometry Catalog, arXiv, arXiv:2307.09681 [astro-ph]. http://arxiv.org/abs/2307.09681http://arxiv.org/abs/2307.09681

Wu, D., & Sun, D.-W. 2013, Innovative Food Science & Emerging Technologies, 19, 1. https://linkinghub.elsevier.com/retrieve/pii/S1466856413000775https://linkinghub.elsevier.com/retriev

Xie, Y., Zhang, J., Shen, C., & Xia, Y. 2021, CoTr: Efficiently Bridging CNN and Transformer for 3D Medical Image Segmentation, Tech. Rep. arXiv:2103.03024, arXiv, arXiv:2103.03024 [cs] type: article. http://arxiv.org/abs/2103.03024http://arxiv.org/abs/2103.03024

Yang, X., Ye, Y., Li, X., et al. 2018, IEEE Transactions on Geoscience and Remote Sensing, 56, 5408. https://ieeexplore.ieee.org/document/8340197/https://ieeexplore.ieee.org/document/8340197/

Yun, B., Wang, Y., Chen, J., et al. 2021, SpecTr: Spectral Transformer for Hyperspectral Pathology Image Segmentation, Tech. Rep. arXiv:2103.03604, arXiv, arXiv:2103.03604 [cs, eess] type: article. http://arxiv.org/abs/2103.03604http://arxiv.org/abs/2103.03604

Zhang, K., & Bloom, J. S. 2020, The Astrophysical Journal, 889, 24. https://dx.doi.org/10.3847/1538-4357/ab3fa6https://dx.doi.org/10.3847/1538-4357/ab3fa6

Zhang , K. & Bloom, J. S. 2020, The Astrophysical Journal, 889, 24. https://iopscience.iop.org/article/10.3847/1538-4357/ab3fa6https://iopscience.iop.org/article/10.3847/1538-4357/ab3fa6